The 15th Symposium on Polar Science

3－5 December 2024

National Institute of Polar Research

Research Organization of Information and Systems

Session OM

Polar Meteorology and Glaciology

Abstracts

Conveners: Shun Tsutaki, and Ikumi Oyabu (NIPR)

OMo1

Derivation of sea ice thickness based on sea ice history using satellite data

Noriaki Kimura, Hiroyasu Hasumi
Atmosphere and Ocean Research Institute, The University of Tokyo

Sea ice is an important component of the climate system at high latitudes. Satellite observations play an important role in monitoring the sea ice. Sea ice concentration has been observeed for a long time since 1970s, and in recent years, highly accurate daily sea ice motion data has become available. The most important information on sea ice is its thickness. Challenges to derive sea ice thickness from satellite remote sensing data have been made by using surface information from microwave radiometers, Synthetic Aperture Radars, or visible and infrared sensors, and by estimating surface height from laser or radar altimeters. However, the ice thickness data currently available are insufficient in terms of accuracy and spatio-temporal coverage. We first analyze the ice history along the ice track traced back to the ice formation, and then develop a method to estimate sea ice thickness based on the obtained sea ice history, especially the heat budget history.

This study uses data from the AMSR-E and AMSR2 microwave radiometers onboard satellites and sea ice thickness observations from the Upward Looking Sonar (ULS) moored in the Beaufort Sea by the Woods Hole Oceanographic Institution. Sea ice movement was calculated using a pattern matching method, the maximum cross correlation technique. We constructed a daily ice-velocity dataset without missing data over the sea-ice area on a 60 × 60 km grid for 2003–2024. Backward trajectory is calculated using this daily ice motion.

First, particles are arranged at an interval of 10 km over the ice area on a certain day. Daily displacement of particles is calculated from the ice velocity on one-day time steps. When the particle reaches open ocean (no-ice) area, we assume it to be ice production. In reality, sea ice concentration around the particle changes from day to day after its creation, which means that the sea ice age composition changes daily by sea ice melting and new sea ice is formation. The daily net sea ice formation can be estimated from the daily increase in the ice area calculated from the change in concentration and the daily increase due to sea ice convergence. Next, daily heat budget was calculated along the sea ice track. The daily growth and melting rates were added to obtain the integrated sea ice thickness. As with the sea ice age, the sea ice thickness composition was calculated to determine the percentage of sea ice of any thickness. The sea ice thickness composition was also derived from ULS observations at 1-second intervals. The sea ice thickness calculated from the heat budget analysis is used as one of the parameters to determine the absolute value of realistic sea ice thickness. By comparing the sea ice thickness composition estimated from the heat budget analysis and the sea ice thickness composition obtained from ULS observations, an empirical equation that relates the two is developed, and the sea ice thickness for the entire Northern Hemisphere is estimated from the estimated sea ice thickness using this equation.

The estimated ice thickness commposition roughly reproduce the temporal variation of the sea ice thickness structure. By applying a simple relational equation obtained at ULS point to the entire Northern Hemisphere, we were able to derive a realistic sea ice thickness distribution (Figure 1). On the other hand, the very thick ice seen in the ULS observations is not yet well reproduced by the heat budget history. This thick ice is considered to be the result of mechanical deformation of the sea ice floe. Currently, we are improving the method with the aim of reproducing the extremely thick ice volume. We plan to improve the derivation method and publish daily sea ice thickness datasets by next spring.

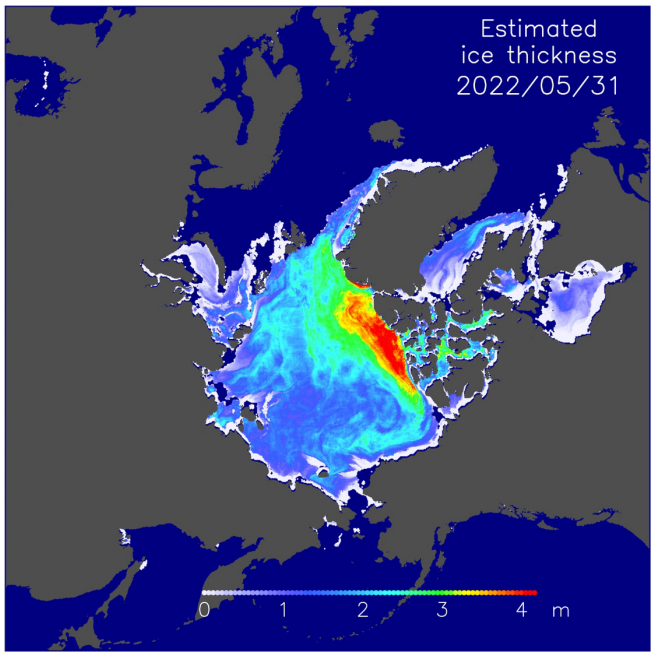

Figure 1. Estimated sea ice thickness on May 31, 2022

Interannual variability of sea ice dynamics conditions in the northern hemisphere

Takenobu Toyota[1], Noriaki Kimura[2] and Jennifer Hutchings[3]
[1]*ILTS, Hokkaido University,*[2]*AORI, The University of Tokyo, and* [3]*Oregon State University*

Recently sea ice conditions have been changing rapidly in the northern hemisphere (NH). The sea ice extent has decreased significantly especially in summer, resulting in the decrease in multi-year ice (MYI) fraction and the spread of seasonal ice zones. Associated with the loss of MYI, mean ice thickness in the Arctic Ocean also decreased significantly. Sumata et al. (2023) pointed out that a regime shift in ice thickness distribution occurred in 2007. These significant changes in ice conditions have accompanied changes in sea ice dynamical properties such as increases in ice drift speed, the significant wave height in the open water, and granular ice fraction in crystal alignments. Our motivation of this study is to examine the change in sea ice dynamics processes from the perspective of deformation processes, which has not been fully understood yet but is an important issue to predict the sea ice conditions in the future. This issue is closely related to sea ice rheology. While traditionally the Viscous-Plastic (VP) rheology (Hibler model) has been adopted in many numerical sea ice models, its validity was not necessarily confirmed from observational data. To address this problem, we examined the regional characteristics and their interannual variability of parameters related to sea ice dynamics, focusing on shape of the elliptical yield curve and deformation conditions in winter of NH. For this purpose, we used AMSR-E&2 derived gridded ice drift datasets with a grid spacing of 60 km for the period of 2002 to 2022. While we presented the results for the 12 regional seas in NH at JpGU 2024, in this study we conducted the similar analysis for the 25 areas evenly divided with the same square area (600 km x 600 km) to reduce the bias which might have been caused by the difference in area between individual seas.

In analysis we paid particular attention to the aspect ratio (e) of the elliptic yield curve for VP rheology and the ridging mode ($\alpha_r(\theta)$; Thorndike et al., 1975) as indicators to represent the dynamical state. This is because e expresses various physical processes in a simplified way and is relevant directly to the dynamical processes in the numerical sea ice model (e=2 for Hibler model). The likelihood of ridging was estimated by $|\dot{\varepsilon}|\alpha_r(\theta)$, referred to as deformation parameter (DP) here. We estimated the optimal e and DP in the individual areas for each winter (December to April) using ice drift datasets, based on Rothrock's theory, and examined the geographical properties by mapping their mean values and their interannual variations.

The results are summarized as follows: (1) VP rheology in Hibler model appears to work efficiently in most cases (mean optimal e = 1.97±0.25), but some regionality was found in optimal e values. Relatively high values are estimated in Greenland Sea (~2.6) and Beaufort Sea (~2.1) (Fig.1). (2) An increasing trend was observed for optimal e values in the Beaufort Sea as well as for shear component of strain rate. It seems consistent if we consider that energy consumption due to lateral friction is becoming more significant there. (3) DP tends to take higher values in the marginal ice zones compared with those in the interior Arctic Ocean, reflecting the higher ice drift speed. (4) Overall DP has a slightly increasing trend in NH except for several areas (e.g. Sea of Okhotsk). Temporal variations of DP show that significant ridging events tend to occur sporadically and have slightly increasing trends in their frequency in most areas except for the Sea of Okhotsk (Fig.2).

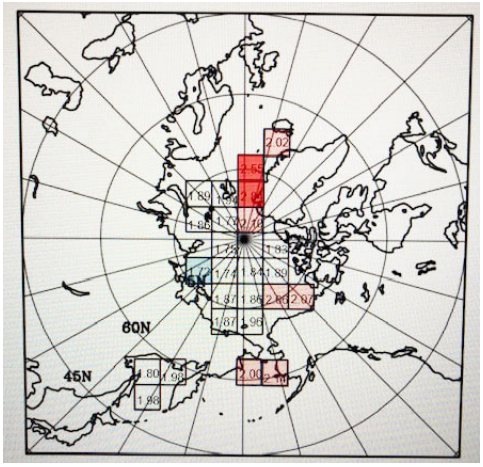

Figure 1. Geographical map of optimal e averaged for 2002 to 2022. (Red: > 2, Blue: < $\sqrt{3}$)

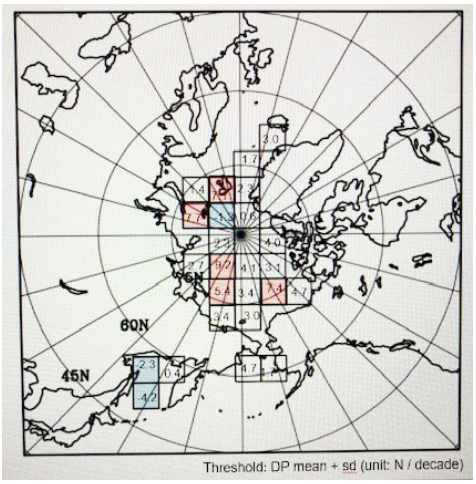

Figure 2. Geographical map of interannual trends of significant ridging events during 2002-2022. (Red: > 5 per decade, Blue: < -1 per decade)

References

Sumata, H. et al., Regime shift in Arctic Ocean sea ice thickness, *Nature*, 615, 443-449, 2023.
Thorndike, A.S. et al., The thickness distribution of sea ice. *J. Geophys. Res.*, 80(33), 4501-4513, 1975.

A new methodology to estimate freshwater content: weekly climatology and interannual anomalies in Baffin Bay and the Labrador Shelf

Vigan Mensah[1], Igor Yashayaev[2], Koji Fujita[3], Stephen E. L. Howell[4], Miho Ikeda[5], and Kay I. Ohshima[1,6]

[1]*Institute of Low Temperature Science, Hokkaido University, Japan*

[2]*Bedford Institute of Oceanography, Dartmouth, NS, Canada*

[3]*Graduate school of environmental studies, Nagoya University, Japan*

[4]*Climate Research Division, Environment and Climate Change Canada, Toronto, Canada*

[5]*Faculty of Science, Hokkaido University, Japan*

[6]*Arctic Research Center, Hokkaido University, Sapporo, Japan*

The Labrador Sea plays an important role in the Atlantic Meridional Ocean Circulation (AMOC) as it provides waters that become a part of the North Atlantic Deep Water, one of the main components of AMOC. The Labrador Sea and the adjacent Baffin Bay are connected to the Arctic Ocean via the Nares Strait. The Labrador Sea and the adjacent Baffin Bay are connected to the Arctic Ocean via the Nares Strait. The hydrography of the Labrador Sea and Baffin Bay is strongly influenced by several local factors including the production-drift-melt cycle of sea ice, precipitation, river runoff, the melting of Canadian and Greenland glaciers, and export of sea ice from the Arctic Ocean. Several of these factors have likely been affected by multi-decadal changes related to global warming and the Arctic amplification. Besides, the Baffin Bay and Labrador Sea are at the receiving end of outflow coming from the Beaufort Sea (the largest freshwater reservoir in the Arctic Ocean) via the Canadian Arctic Archipelago, including the Nares Strait. Another route for freshwater export goes through the Fram Strait and along the eastern coast of Greenland to enter the Baffin Bay and Labrador Sea from the east. These flows can be defined as remote sources of freshwater. The freshwater volume contained in the Beaufort Sea is known to vary at the decadal scale in periods of freshwater accumulation and release, and these variations affected the salinity in the Baffin Bay and the Labrador Sea (Zhang et al., 2021). Besides, the freshwater content in the Beaufort Sea has considerably increased since 2000 (Proshutinsky et al., 2019) due to a combination of increases Bering Strait throughflow, river outflow and multi-year ice melting. These recent variations make it essential to estimate the volume of local vs. remote freshwater in the Baffin Bay and Labrador Sea region, and to compare the relative importance of their variability. Such work has not been conducted before due to the difficulty in distinguishing local vs. remote freshwater input using classic freshwater estimation methods.

In this study, we developed a new methodology to estimate the weekly freshwater input in the Baffin Bay and Labrador Sea region, which can be integrated in time to obtain the full summer freshwater input. The method consists in estimating the weekly depth-average salinity in every point of a gridded domain (Fig. 1), improving the quality of the estimate via an iterative process following Yashayaev and Zveryaev (2001). In each iteration, salinity data are selected within a distance and topographic range around each grid point, outliers are detected and removed, and corrections are applied to account for the spatial and temporal (interannual anomalies) variability of the dataset. The climatology is then recalculated at each iteration as the data quality of the dataset is improved via the different corrections.

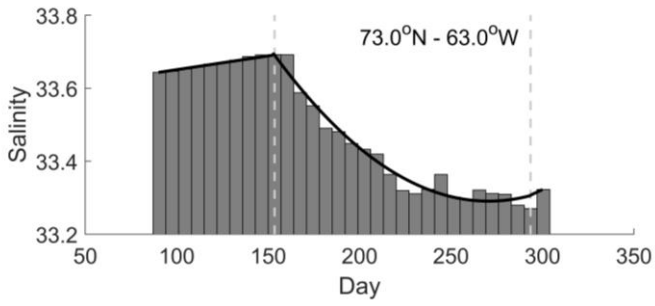

Figure 1. 0-250 m mean salinity vs. nominal day in Baffin Bay. The black line shows the idealized seasonal cycle and the dashed gray lines the start/end of the freshening season.

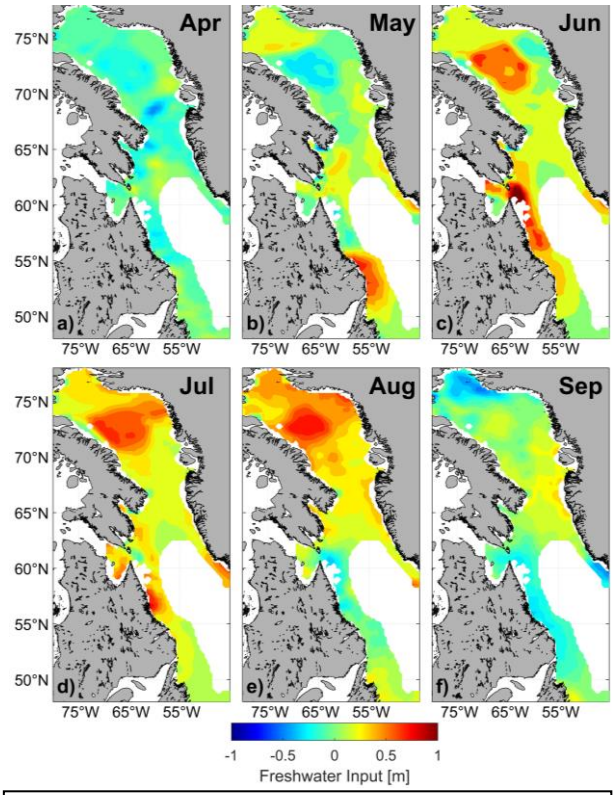

Figure 2. Monthly climatology of 0-50 m freshwater input.

We estimated climatologies in the 0-50 m and 0-250 m depth-integrated ranges, which allowed us to evaluate the weekly input of freshwater into the region. Fig. 2 displays the monthly 0-50 m freshwater inputs from April to September in our study region. The spatiotemporal variability of the freshening input allows us to suggest the following phenomena as causes for the freshwater input: in May (Fig. 2b), the outflow of the Churchill river and sea ice melt may cause the large freshwater plume between 50°N-56°N. The ice flux from the Nares Strait may be responsible for the large freshwater input north of 74°N until July (Figs. 2b-d). Sea Ice melt from the North Water Polynya may be responsible for the large freshwater inputs in the middle of Baffin Bay from June to August (Figs. 2c-e). Sea ice drifting southward from Baffin Bay and its subsequent melting could be a cause for the large freshwater input extending from 65°N to 56°N in June and July (Figs. 2c-d). Lastly, the melting of glaciers might be responsible for the increase of the freshwater input of the coast of Central and northwestern Greenland in July and August (Figs. 2d-e). Time series analysis is planned to confirm the validity of the above suggestions.

Interannual anomalies were estimated as the difference between yearly and climatological values in 2 different ways. The total freshwater input (FWI) anomaly was estimated from the yearly change of salinity at the end of summer. The local FWI anomaly was estimated from the integration of the anomaly in weekly salinity changes (i.e., the anomaly of Fig. 1). The residual contribution obtained by subtracting local anomaly from the total anomaly may be interpreted as the remote FWI anomaly in most cases. Fig. 3 displays the yearly time series of residual FWI in Baffin Bay (Fig. 3a) and off southwestern Greenland (Fig. 3b) between 1950 and 2023. As the temporal variability differs largely between the two regions, the figure illustrates how these regions are affected by different remote sources of freshwater. In Baffin Bay, the input of remote freshwater presents a slight increasing trend and strong decadal anomalies. The remote FWI has been mostly increasing since 2002. As Baffin Bay is affected by inflow of remote freshwater from the Beaufort Sea, the latter increase we observed could be related to the enhanced melting of multi-year ice and freshwater flux from the Pacific, which has been occurring starting the early to mid-2000s. The region off Southwestern Greenland exhibits strong variability at the 5-10-year scale (Fig. 3b) with a steady increase in freshwater input by more than 1 m between 2006 and 2012, that could be related to increased melting of glaciers from East Greenland or/and multiyear ice melting north of Greenland. Further analysis is needed to better understand the variability of these residual FWI time series.

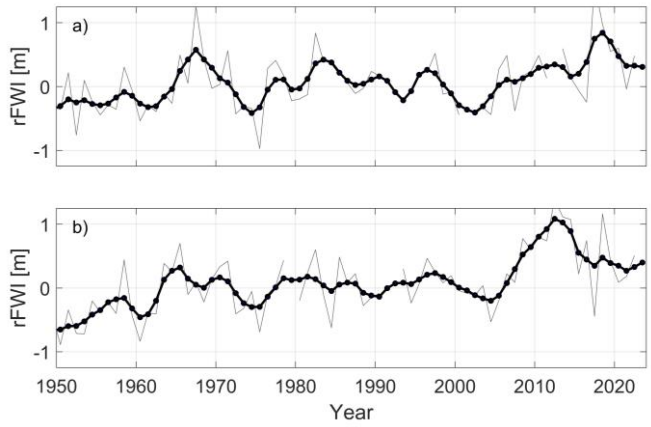

Figure 3. Yearly time series (thin gray solid lines) of residual FWI in Baffin Bay (a) and off southwestern Greenland (b). The thick black solid lines represent the 5-year moving average time series.

References

Proshutinsky, A., Krishfield, R., Toole, J. M., Timmermans, M. L., Williams, W., Zimmermann, S., Yamamoto-Kawai, M., Armitage, T. W. K., Dukhovskoy, D., Golubeva, E., Manucharyan, G. E., Platov, G., Watanabe, E., Kikuchi, T., Nishino, S., Itoh, M., Kang, S. H., Cho, K. H., Tateyama, K., and Zhao, J.: Analysis of the Beaufort Gyre Freshwater Content in 2003–2018, J Geophys Res Oceans, 124, 9658–9689, https://doi.org/10.1029/2019JC015281, 2019.

Yashayaev, I. M., & Zveryaev, I. I.: Climate of the seasonal cycle in the North Pacific and the North Atlantic oceans. International Journal of Climatology: A Journal of the Royal Meteorological Society, 21(4), 401-417, 2021

Zhang, J., Weijer, W., Steele, M., Cheng, W., Verma, T., and Veneziani, M.: Labrador Sea freshening linked to Beaufort Gyre freshwater release, Nat Commun, 12, https://doi.org/10.1038/s41467-021-21470-3, 2021.

Responsible factors for the recent regime shift in Antarctic sea ice

Kazuya Kusahara[1] and Hiroaki Tatebe[1]
[1]*Japan Agency for Marine-Earth Science and Technology (JAMSTEC)*

The Antarctic sea ice plays a crucial role in the global climate system and exhibits one of the most dynamic seasonal changes on Earth. While the Antarctic sea-ice extent showed a slow increasing trend from the late 1970s to 2015, a significant regime shift occurred in 2016, marked by a sharp decrease in sea ice extent that has persisted with record lows in recent years (Fig. 1a). This study investigates the causes of this recent regime shift using the global sea ice-ocean coupled model (COCO) with a 0.25-degree resolution, driven by surface boundary conditions based on atmospheric reanalysis. The model can reasonably reproduce the observed sea-ice extent and concentration anomalies (Fig.1). A comprehensive series of numerical experiments reveals that the thermodynamical surface boundary conditions, particularly the heat flux entering the ocean near the ice edge, are the dominant drivers of the observed sea-ice reduction. Additionally, wind stress is found to contribute to the summer sea-ice extent to some extent (particularly in the 2016/2017 reduction), but its role in the recent regime shift is minor. These findings highlight the critical impact of oceanic heat influx near the ice edge on the recent and continued negative anomalies in Antarctic sea ice.

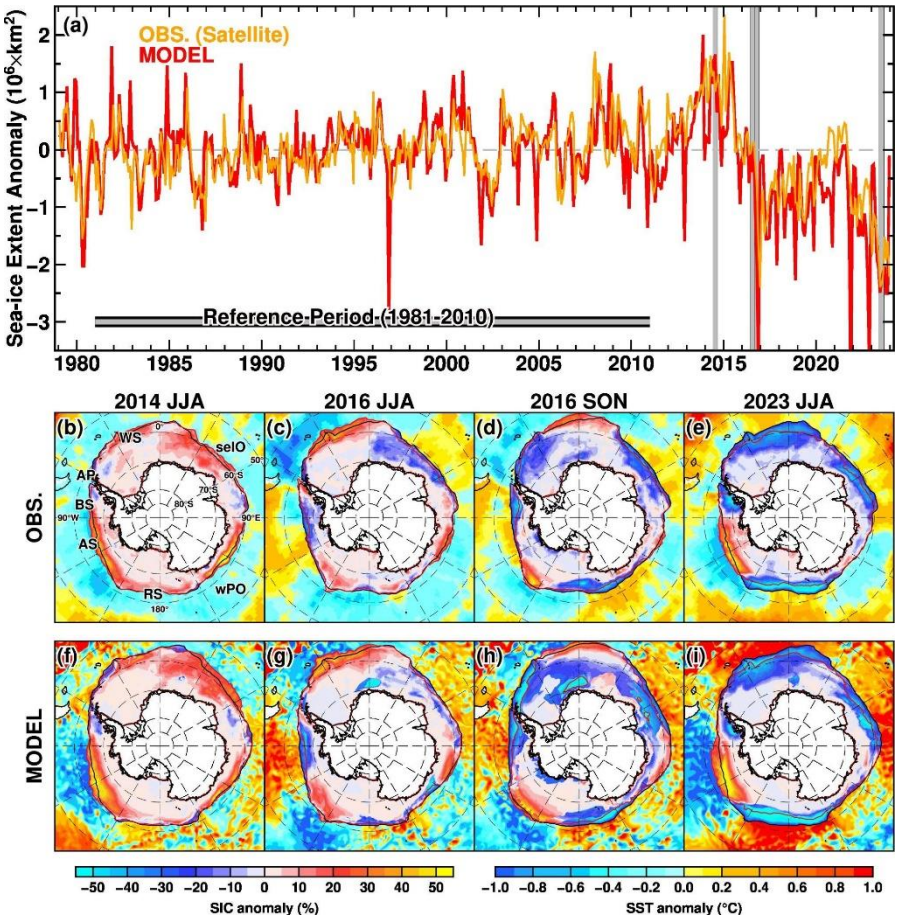

Figure 1: Sea-ice extent and concentration anomalies in Antarctic sea ice. Orange and red lines in panel (a) show satellite-based and model's sea-ice extent anomalies, respectively. Panels b–e and f–i show sea-ice concentration and sea-surface temperature anomalies in the observation and model, respectively, during selected year-seasons (2014 JJA, 2016 JJA, 2016 SON, 2023 JJA). Anomalies were calculated relative to the reference period of 1981–2010.

Estimation of sea-ice melt amount from the JARE dense XCTD observations, comparing with the climatology of the ice melt amount

Mizuki Komatsu[1], Kay I Ohshima[2,3] , Noriaki Kimura[4], Sohey Nihashi[2,5],
Masakazu Fujii [6,7], Masashi Machida[1] and Takeshi Tamura[6,7]

[1]*Graduate School of Environmental Science, Hokkaido University*
[2]*Institute of Low Temperature Science, Hokkaido University*
[3]*Arctic Research Center, Hokkaido University*
[4]*Atmosphere and Ocean Research Institute, The University of Tokyo*
[5]*Department of Engineering for Innovation, National Institute of Technology (KOSEN), Tomakomai College*
[6]*National Institute of Polar Research*
[7]*The Graduate University for Advanced Studies, SOKENDAI*

In the Earth system, meridional transport and redistribution of heat and freshwater/salt are made mainly by the atmosphere and oceans. Sea-ice also plays a similar role through its production, transport and melt (1). Especially in the Southern Ocean with the largest seasonal ice zone, sea-ice plays an essential role in freshwater/salt transport. Over the last 40–50 years, the intermediate layer of the Southern Ocean has been the most freshening area in the world (2,3). This is partly due to increased northward transport and melting of sea-ice (4). The increase in ice-melt also strengthens stratification and potentially hampers the mixing of deeper, carbon-rich water into the surface, which could enhance the net uptake of carbon dioxide. Thus the sea-ice melt and its variation potentially impact on the climate change. However, estimation of ice-melt amount is very limited, because of the complex and heterogeneous melting process. We estimate sea-ice melt utilizing spring salinity profiles from ship-based, Argo float, and elephant seals data, total of nearly 25000 data. The estimation is made by calculating the salinity deficit of the upper layer affected by sea-ice melt (Figure 1). The key point in the estimation is to find the top of winter water, which is nearly at the freezing point and not affected by warming and ice melting. We have developed an algorithm to detect the top of winter water automatically by combined use of potential temperature and salinity profiles. Our results show that large sea-ice melt (~1.5 m) occurs in the western side of the three gyres of Weddell, Ross, and east of Kerguelen plateau, where sea-ice is drifted from the coastal area to offshore. The total freshwater flux by sea-ice melt is calculated to be 17010 Gt/yr. This value is six times larger than that of the total glacial melt (~2900 Gt/yr): the basal melt plus calving/ iceberg melt (5, 6).

Following this climatological study, we have conducted the dense XCTD observations under the JARE (Japanese Antarctic Research Expedition) 64 (2022/23) and JARE65 (2023/24). The data points are indicated in Figure 2. Using these data, we estimated sea ice melt amount by the method shown in Figure 1. Based on these estimations, we discuss the characteristics and differences in the melt amount between the two seasons by comparing the sea-ice drift data, sea-ice concentration data, and heat flux calculation.

We compared the climatological values of ice melt amount (indicated by green in Fig.3) , and ice melt amount for the seasons 2022/23 (indicated by blue) and 2023-24 (indicated by red). The following two features can be found. First, the overall melt amount in 2023-24 (JARE65) is larger than that in 2022-23 (JARE64), while the melt amount in 2022-23 is larger than that in 2023-24 for the area between 65°E and 75°E. Second, the melt amount in 2023-24 is especially large in the area between 105°E and 115°E, compared to 2022-23 and climatology.

Our preliminary analysis shows some characteristics of the sea-ice drift. In the region (65°E -75°E) of Feature 1, the offshore component of the sea-ice drift anomaly in October and November 2022 was found to be dominant. On the other hand, the sea-ice drift anomaly in October and November 2023 showed a predominance of the shoreward component. The region (105°E -115°E) in Feature 2, the offshore component of the drift anomaly is dominant in 2023-24, while the shoreward component is dominant in 2022-23. We will present a time series of sea-ice concentration data, sea-ice drift data and the heat input to examine the history of sea-ice transport and melt. This study may provide a starting point for estimating future long-term interannual variability of sea-ice melt amount.

Acknowledgements
Ship-based observations were conducted in cooperation with Japanese Antarctic Research Expedition (JARE) and Japan Coast Guard. We would like to thank to Mifuka Ishikawa (JARE64) and Shun Ikawa (JARE65) from Hydrographic and Oceanographic Department of Japan Coast Guard and those who are involved with the CTD observations onboard Shirase.

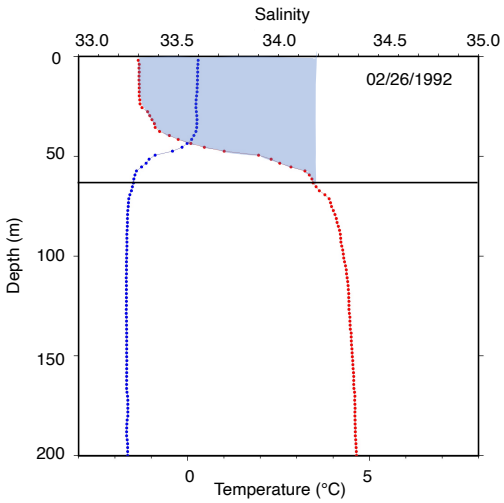

Figure 1. Vertical profiles of temperature (blue dotted line) and salinity (red dotted line) after sea-ice melting. Shading indicates the salinity deficit from which the ice-melt amount can be estimated. The lateral line indicates the deepest depth affected by sea-ice melt. The observational date is shown at the top of the figure.

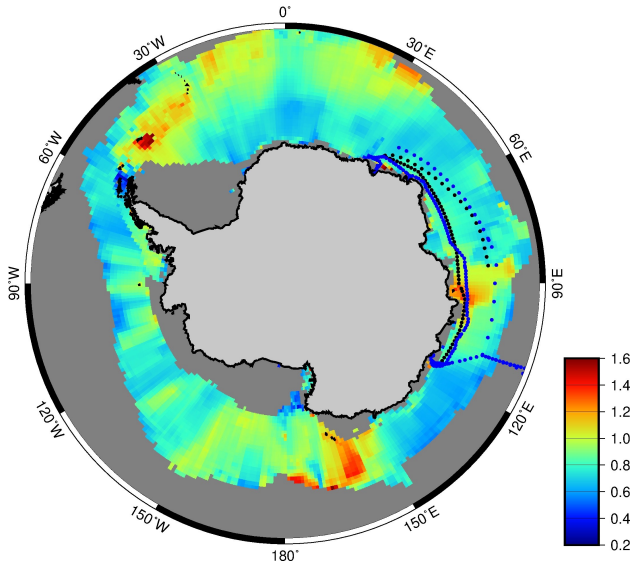

Figure 2. Climatology map of ice-melt amount and XCTDs data observed points along the JARE route. The background color represents the melt amount (m). Black and blue point indicates 2022-23 (JARE64) and 2023-24 (JARE65), respectively.

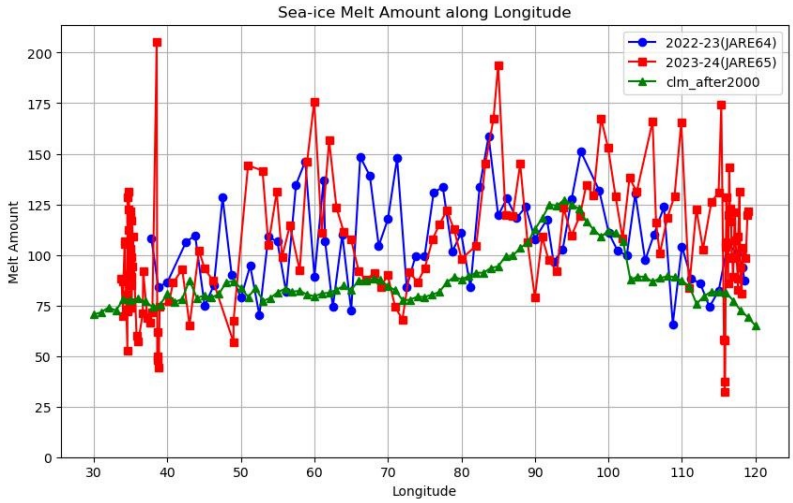

Figure 3. Sea-ice melt amount along the longitude. Green, blue, red indicates the climatology of sea-ice melt after 2000, sea-ice melt in 2022-23 and sea-ice melt in 2023-24, respectively.

References

1. Hasumi, H. and N. Suginohara, Haline circulation induced by formation and melting of sea ice, J. Geophys. Res, 100, 20613–20625, 1995.
2. Helm, K. P., N. L. Bindoff, J. A. Church, Changes in the global hydrological-cycle inferred from ocean salinity, Geophys. Res. Lett, 37, L18701, 2010.
3. Durack, P. J., S. E. Wijffels, R. J. Matear, Ocean salinities reveal strong global water cycle intensification during 1950 to 2000, Science, 336, 455–458, 2012.
4. Haumann, F. A., N. Gruber, M. Münnich, I. Frenger, S. Kern, Sea-ice transport driving Southern Ocean salinity and its recent trends, Nature, 537, 89–92, 2016.
5. Rignot, E., S. Jacobs, J. Mouginot, B. Scheuchl, Ice-shelf melting around Antarctica, Science, 341, 266–270, 2013.
6. England, M. R., T. J. Wagner, I. Eisenman, Modeling the breakup of tabular icebergs, Sci. Adv, 6, eabd1273, 2020.

OMo6

Temporal variability of warm water inflows into the Totten Ice Shelf cavity

Yoshihiko Ohashi[1], Daisuke Hirano[1,2], Kohei Mizobata[3], Kazuya Kusahara[4], Kazuki Nakata[5], Kazuya Ono[6], Masakazu Fujii[1,2], Ryosuke Makabe[1,2], Kay I. Ohshima[6], Takeshi Tamura[1,2] and Shigeru Aoki[6]

[1]*National Institute of Polar Research*

[2]*SOKENDAI*

[3]*Tokyo University of Marine Science and Technology*

[4]*Japan Agency for Marine-Earth Science and Technology*

[5]*Japan Aerospace Exploration Agency*

[6]*Institute of Low Temperature Science, Hokkaido University*

The Totten Glacier in East Antarctica holds an ice volume equivalent to a global sea-level rise of more than 3.5 m and is grounded below sea level. Therefore, the Totten Glacier is vulnerable to ocean forcing such as warm water intrusion. A recent study combining in-situ observations and numerical simulations (Hirano et al., 2023) revealed that warm modified Circumpolar Deep Water (mCDW) enters the Totten Ice Shelf (TIS) mainly along the deep troughs, connecting the Sabrina Depression to the TIS cavity, and that the deep troughs play a critical role in controlling ocean heat transport to the TIS cavity. However, the temporal variability of the mCDW inflows, which determines the TIS basal melt rate, is poorly understood due to a lack of time series data.

Two-years of mooring observations were conducted in the deep trough, from March 2022 to 2024 (Fig.1). The near-bottom mooring time series showed inflows of the warm, saline, and low dissolved oxygen mCDW throughout the observation period. The seasonal cycle of the mCDW temperature was characterized by a peak in the fall (from April to June, θ = 0.2~0.4ºC), a rapid decrease during the winter months to below 0ºC (from July to September, θ = −0.6ºC~−0.2ºC at minimum), and then a gradual increase towards summer (from October to March, θ = −0.2~0.2ºC). The seasonal cycle of the mCDW salinity showed a similar tendency to that of temperature, while dissolved oxygen showed the opposite one. In the upstream Dalton Polynya, sea-ice production increased from February to April–June and then gradually decreased to November. There was a time lag of ~4 months between the periods of increased sea ice production and decreased mCDW temperatures with increased dissolved oxygen in the deep trough. Focusing on the year-to-year variability, the temperature and dissolved oxygen of mCDW in 2023 were lower and higher than those in 2022, respectively. Sea-ice production in the upstream Dalton Polynya in 2023 was 1.5 times higher. Thus, lower temperature and higher dissolved oxygen of mCDW in 2023 were likely due to the greater heat loss associated with higher sea-ice production. This study suggests that the upstream Dalton Polynya also plays an important role in controlling seasonal and year-to-year variabilities in the ocean heat transport to the TIS.

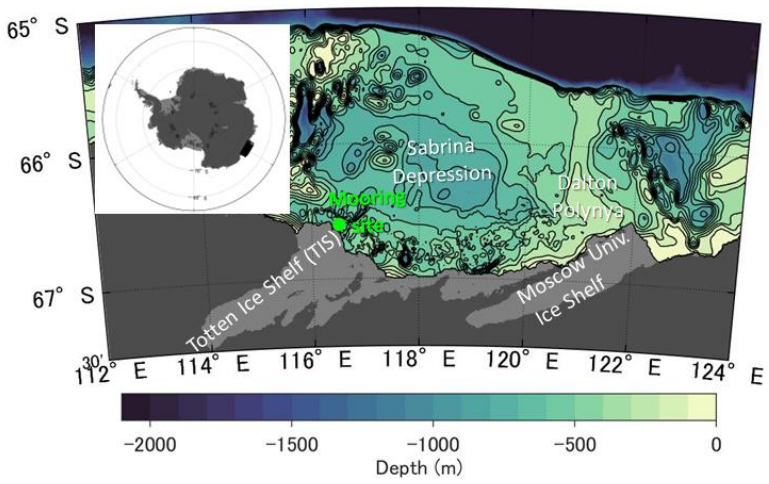

Fig. 1. Study area and location of the mooring site.

References

Hirano, D., T. Tamura, K. Kusahara *et al.* On-shelf circulation of warm water toward the Totten Ice Shelf in East Antarctica. Nature Communications, 14, 4955, 2023.

OMo7

Reproducibility of Arctic climate in CMIP6 models

Takuro Aizawa[1,2], Naga Oshima[2] , Seiji Yukimoto[2] , and Yusuke Ushijima[3]
[1]*National Institute of Polar Research*
[2]*Meteorological Research Institute, Japan Meteorological Agency*
[3]*Center for Marine Environmental Studies, Ehime University*

Observational datasets show that the Arctic has been warming nearly four times faster than the globe during last four decades. This phenomenon is known as Arctic Amplicfication (AA) of warming. With a multimodel analysis by climate models participating in Coupled Model Intercomparison Project phase 6 (CMIP6), most of the models still cannot simulate a plausible reduction of sea-ice amount and simultaneously a plausible change in global-mean surface air temperature over time. One reason for this is a lack of comprehensive representation of the Arctic climate in those climate models. This study investigates the reproducibility of Arctic climate in CMIP6 models by examining the global-mean surface air temperatures (GMSATs), Arctic-mean surface air temperatures (AMSATs), September sea ice areas (SIAs) and their trends. In addition, sea ice sensitivities to AMSATs, as well as AA over the 25-year period from 1990 to 2014 are also examined. Rreanalyses and the observational data are used for the references.

Since many CMIP6 models simulate lower AMSATs compared to the reanalyses, a simulated AMSATs in the multi-model mean is lower than the reanalyses (Fig. 1a). Additionally, there is considerable variation in the simulated AMSATs across models, with a range exceeding 6 K which is three times greater than that for GMSAT (not shown). The CMIP6 models tend to exhibit large biases in mean September SIAs with significant inter-model spread comapred to the observations (Fig. 1b). This is consistent to the cold biases in AMSATs. The sea ice sensitivities to the AMSAT change in many CMIP6 model locate within the plausible range of the observations (Fig. 1b). Climate models with larger mean SIA tend to exhibit lower sea ice sensitivity to AMSATs (Fig. 1b). The AA indices, which are estimated from the trends in AMSAT versus GMSAT (indicated by slope of the line connecting the points of each model with the origin in Fig. 1c), locate within a range of 2 to 3 for nearly all models, indicating low model dependency. In this presentation, we examine the CMIP6 model's ability to reproduce the Arctic climate from various aspects with respect to AMSATs and SIAs.

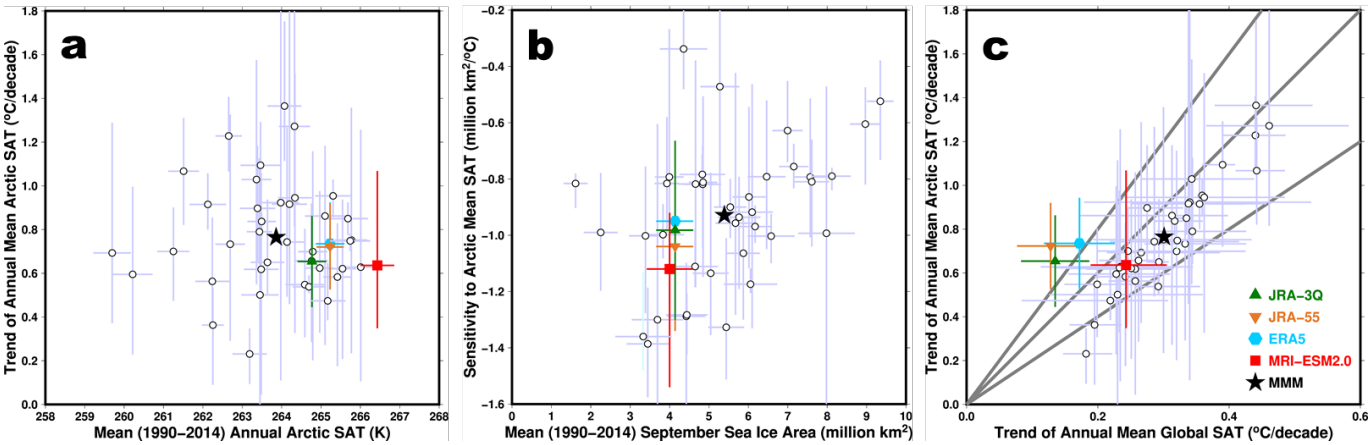

Figure 1. Reproducibility of 39 CMIP6 models for Arctic climate in the period 1990–2014. Relationships between (a) the 1990–2014 mean AMSATs, avereged over 60°N–90°N and the trends of the AMSATs, (b) the 1990–2014 mean September SIAs and sea ice sensitivity to the 1990–2014 mean AMSATs, and (c) the trends of GMSATs and the trends of AMSATs. The gray lines in (c) represent the slopes of the AA indices of 2, 3, and 4 from the bottom to top, respectively. The multi-model mean (MMM) values are indicated by the star marks.

OMo8

Understanding the Arctic-Indian Monsoon Linkages: Insights from satellite and model-based observations

Juhi Yadav[1,2], Avinash Kumar[1], Seong-Joong Kim[3], Rohit Srivastava[1], Rahul Mohan[1], M. Ravichandran[4]

[1] *National Centre for Polar and Ocean Research (NCPOR), Ministry of Earth Sciences, Goa, India*
[2] *Department of Marine Geology, Mangalore University, Mangalore 574 199, India*
[3] *Korea Polar Research Institute, Incheon 21990, Republic of Korea*
[4] *Ministry of Earth Sciences, Prithvi Bhavan, Lodhi Road, New Delhi 110003, India*

The Indian monsoon system is one of the most active branch of the Asian monsoon system, accounts for approximately ~75-80% of India's annual precipitation (Jin and Wang 2017, Bhatla *et al* 2016, Das *et al* 2014). The present study investigates the teleconnection between Arctic Sea Ice Concentration (SIC) and Indian Summer Monsoon Rainfall (ISMR), using satellite observations and simulations from the Coupled Model Intercomparison Project Phases 5 and 6 (CMIP5 and CMIP6) over the period 1979-2021. Through Rotated Empirical Orthogonal Function (REOF) analysis, the dominant mode (PC1) of ISMR was identified, explaining 31.7% of the variance, indicating significant regional variability. Further, to identify the season and strength of the relationship between SIC and ISMR, Singular Value Decomposition (SVD) analysis was conducted. We observed a maximum covariance of 41.1% during spring between Arctic SIC and ISMR (Figure 1), with significant correlations in both CMIP5 (30.6%) and CMIP6 (42.8%) simulations. The results show that ISMR PC1 and observed Arctic Spring SIC are significantly correlated ($r = -0.25$, $p<0.05$), with robust correlations in the Central Arctic ($r = 0.51$) and the Barents-Kara Sea ($r = -0.39$, $p<0.05$). Satellite observations and multi-model ensemble mean (MMEM) simulations from CMIP5 and CMIP6 show a strong connection between spring Arctic SIC and ISMR (Table 1). SVD and correlation analyses highlights similarities and differences between observed and model based SIC data. While spring shows the highest total covariance in both observations and CMIP5 simulations, CMIP6 models peak in winter, followed by spring. This difference suggests that CMIP6 models might overestimate the observed variations, indicating that external forces alone may not fully explain the trends observed during the satellite era.

This study investigated the physical mechanisms through which spring Arctic SIC influences the ISMR, focusing on interconnected atmospheric circulation patterns and jet stream positioning. During the high sea ice years (HSYs) in the Central Arctic, distinct pressure centers develop over Europe and Asia, resembling the circumglobal teleconnection (CGT) pattern (Ding and Wang 2005). These patterns promote enhanced rainfall in northwestern and peninsular India due to a strengthened easterly jet and associated Rossby wave propagation. Conversely, during low sea ice years (LSYs) the jet streams and the high-pressure systems weaken, hindering the monsoon. The study also highlights the role of upper atmospheric Rossby waves in influencing the circulation patterns. However, the LSY in Barents-Kara region corresponds to the North Atlantic-Eurasia teleconnection wave train pattern and ridge formation over northwestern Europe that affects the Indian monsoon onset. Whereas, high Barents-Kara SIC alters the atmospheric circulation pattern over northwestern Europe, leading to decreased ISMR. This comprehensive study highlights the importance of seasonal changes in the Arctic and their far-reaching impacts on the subsequent ISMR.

Statistical analysis and validation with multi-model datasets support this hypothesis. Our findings indicate that spring SIC anomalies influence pressure patterns and wind forcing, with effects persisting into summer. This combined SIC variation modulates Rossby waves, ultimately influencing subpolar westerlies. Crucially, these results highlight the long-term influence of spring Arctic SIC on ISMR patterns. Given the complex nature of ISMR prediction, identifying novel influencing factors is essential. Our study suggests that understanding the regional dynamics of Arctic SIC is vital for developing more reliable future climate models, which could significantly improve predictions of ISMR, especially in the context of ongoing global climate change.

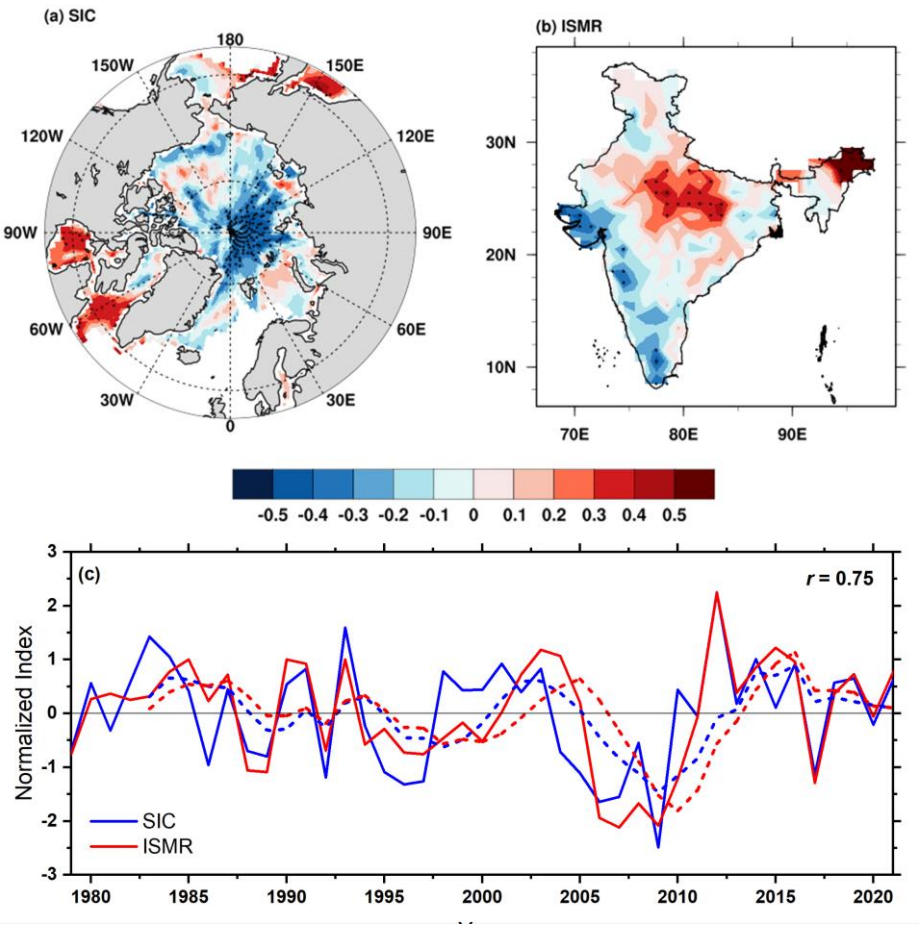

Figure 1 The leading mode of covariability between detrended Indian summer monsoon rainfall (ISMR) and spring Arctic sea ice concentration (SIC) is represented through the leading heterogeneous correlation maps for (a) spring Arctic SIC and (b) ISMR. The dots represent a statistical significance level of 95% based on a two-tailed Student's t-test. The months considered for spring are March–May and for summer, June–September. (c) The normalised time-series variations in the leading singular value decomposition (SVD) for ISMR (red) and spring Arctic SIC (blue) are presented using solid lines. The 5-year running mean is represented by dashed lines, indicating a correlation between the expansion coefficients (r) with a significance level of 99%.

Table 1. Total squared covariance fraction based on singular value decomposition analysis between normalized, detrended Indian Summer Monsoon Rainfall (ISMR) and multi-model ensemble mean Arctic sea ice concentration (SIC) from CMIP5 and CMIP6 datasets. Values are statistically distinct from other eigenvectors. Note: ISMR calculation includes data from June to September.

Season	SVD 1(%)	SVD 2(%)	SVD 3(%)	Total Variance (%)
Spring (MAM)	30.6 (42.8)	24.8 (23.2)	10.2 (8.6)	65.6 (74.6)
Summer (JJA)	31.6 (31.8)	18 (20.7)	11.2 (15.2)	60.8 (67.7)
Autumn (SON)	34.9 (40.2)	20.1 (17.6)	9.4 (13.9)	64.4 (71.7)
Winter (DJF)	31.6 (45.5)	24 (29.9)	11.1 (7.6)	66.7 (83)

References

Bhatla R, Singh A K, Mandal B, Ghosh S, Pandey S N and Sarkar A 2016 Influence of North Atlantic Oscillation on Indian Summer Monsoon Rainfall in Relation to Quasi-Binneal Oscillation *Pure Appl. Geophys.* **173** 2959–70

Das P K, Chakraborty A and Seshasai M V R 2014 Spatial analysis of temporal trend of rainfall and rainy days during the Indian Summer Monsoon season using daily gridded (0.5° × 0.5°) rainfall data for the period of 1971–2005 *Meteorol. Appl.* **21** 481–93 Online: https://onlinelibrary.wiley.com/doi/full/10.1002/met.1361

Ding Q and Wang B 2005 Circumglobal teleconnection in the Northern Hemisphere summer *J. Clim.* **18** 3483–505

Jin Q and Wang C 2017 A revival of Indian summer monsoon rainfall since 2002 *Nat. Clim. Chang.* **7** 587–94 Online: https://www.esrl.noaa.gov/psd/data/gridded/data.ncep.reanalysis.derived.pressure.html

Modulation of the Ural Blocking and its Effects on Extreme Temperature Events under Progressing Global Warming

Masatake E. Hori[1], Masakazu Yoshimori[1] and Jinro Ukita[1]
[1]*Atmosphere and Ocean Research Institute, The University of Tokyo*

Atmospheric blocking is a quasi-stationary, large-scale meandering of the jet stream in the mid to high latitude which contributes to severe weather conditions such as extremes in temperature and heavy precipitation. While atmospheric blocking contributes to large-scale horizontal transport of heat and water vapor, its modulation under the progression of global warming and its effect on extreme temperature events in the Arctic has not been fully understood. Of particular interest is how the weakened meridional temperature gradient under global warming influences the seasonality and variability of temperature extremes that accompany atmospheric blockings.

In this study, we investigate the modulation of atmospheric blocking and its impact on extreme temperature events under the progression of global warming using a large ensemble climate simulation dataset, the database for Policy Decision making for Future climate change (d4PDF; Fujita et al. 2019; Mizuta et al. 2017). The dataset consists of 100 members of non-warming experiment (HPB-NAT), 100 members of the historical experiment (HPB), 54 members 2K global warming experiment (HFB-2K), and 90 members of 4K global warming experiment (HFB-4K). Blocking events were detected using the anomaly method described in Woollings et al. (2018) against the daily mean anomaly values of the 500hPa geopotential height. We also used the ERA5 reanalysis dataset (Hersbachet al. 2020) for comparison.

The climatology of atmospheric blocking frequency shows that the HPB experiment closely resembles the spatial distribution of ERA5 with a slightly weaker signal in the climatological center of the blockings. The difference in monthly frequency of blocking occurrence under HFB-4K and HPB-NAT experiments shows that while the blocking occurrence decreases over the ocean basins of the Atlantic and Pacific, sustained increase is seen over the Ural region during the cold season starting from October through March. Taking the composite of surface air temperature during such continental blocking events reveals a positive anomaly along the northern coast of the Eurasian continent and a negative anomaly in the mid-latitudes near Lake Baikal. Comparing the probability density of temperature occurrences in the region reveals that while the frequency of blocking events increases under HFB-4K compared to the non-warming experiment HPB-NAT, the range of temperature in the higher extreme is suppressed. The role of temperature and moisture advection in maintaining the extreme temperature event associated with Ural blockings is discussed in the presentation.

References

Fujita, M., et al.: Precipitation changes in a climate with 2-K surface warming from large ensemble simulations using 60-km global and 20-km regional atmospheric models, Geophys. Res. Lett., 46, 435–442, https://doi.org/10.1029/2018gl079885, 2019.

Hersbach, H., et al.: The ERA5 global reanalysis, Q. J. R. Meteorol. Soc., 146, 1999–2049, https://doi.org/10.1002/qj.3803, 2020.

Mizuta, R., et al.: Over 5,000 Years of Ensemble Future Climate Simulations by 60-km Global and 20-km Regional Atmospheric Models, Bull. Am. Meteorol. Soc., 98, 1383–1398, https://doi.org/10.1175/BAMS-D-16-0099.1, 2017.

Woollings, T., et al.: Blocking and its Response to Climate Change, Curr. Clim. Change Rep., 4, 287–300, https://doi.org/10.1007/s40641-018-0108-z, 2018.

Impacts of the snow–hydrological processes on near-surface temperature variability over the Eurasian continent

Naresh G. Ganeshi[1,2], Yuhei Takaya[2], Kensuke K. Komatsu[3], Yu Kosaka[4], Hiroyasu Hasumi[1]

[1]*Atmosphere and Ocean Research Institute, The University of Tokyo, Kashiwa, Japan*

[2]*Department of Atmosphere, Ocean, and Earth System Modeling Research, Meteorological Research Institute, Japan Meteorological Agency, Tsukuba, Japan*

[3]*Osaka Regional Headquarters, Japan Meteorological Agency, Osaka, Japan*

[4]*Research Center for Advanced Science and Technology, The University of Tokyo, Meguro, Japan*

Abstract

The snow–hydrological processes have a major contribution to the climate variability over the northern latitudes. While previous studies have discussed the remote influence of atmospheric circulation on Eurasian climate, impacts of the snow–hydrological processes on near surface temperature over a snow-sensitive region (cold spot) has not been fully understood and requires further investigation. In this study, we examined various snow–hydrological datasets for the period 1980–2020 to assess the roles of land surface processes on near surface temperature over the Eurasian continent.

Results from Liang–Kleeman information flow analysis show that a cold spot of strong snow–soil moisture–temperature coupling is located over the West Siberian (WS) region, where fluctuations in snow and soil moisture (SM) tend to modulate the near-surface temperature significantly. A composite analysis indicated that a significant decrease (increase) in SM by ~12 % (~ 10%) in response to a decrease (increase) in snow water equivalent (SWE) by ~ 6 mm (~ 5 mm) during June tends to enhance warm (cold) temperature anomalies over the WS region by ~ 2-3 deg C (~2 deg C) through weakening of surface energy partitioning. In particular, drier land surface conditions lead to enhance the surface air temperature (T2M) when large amount of available radiational energy revert back to the atmosphere through in terms of sensible heating process. Whereas, we see colder near-surface temperature conditions during the wet phase of soil moisture due to increase of evaporative cooling.

The study also investigates the influence of atmospheric circulation on near-surface temperature over the WS region. This analysis indicates that anomalous persistent high (low) surface pressure, anticyclonic (cyclonic) circulation anomalies and clear sky conditions (cloudy conditions) associated with the so-called British-Baikal corridor pattern further favours to maintain the extreme hot (cold) temperature conditions over the WS region through land-atmosphere feedback processes. These findings contribute to our better understanding of the influence of snow– hydrological processes on the atmosphere and their associated sub-seasonal predictability.

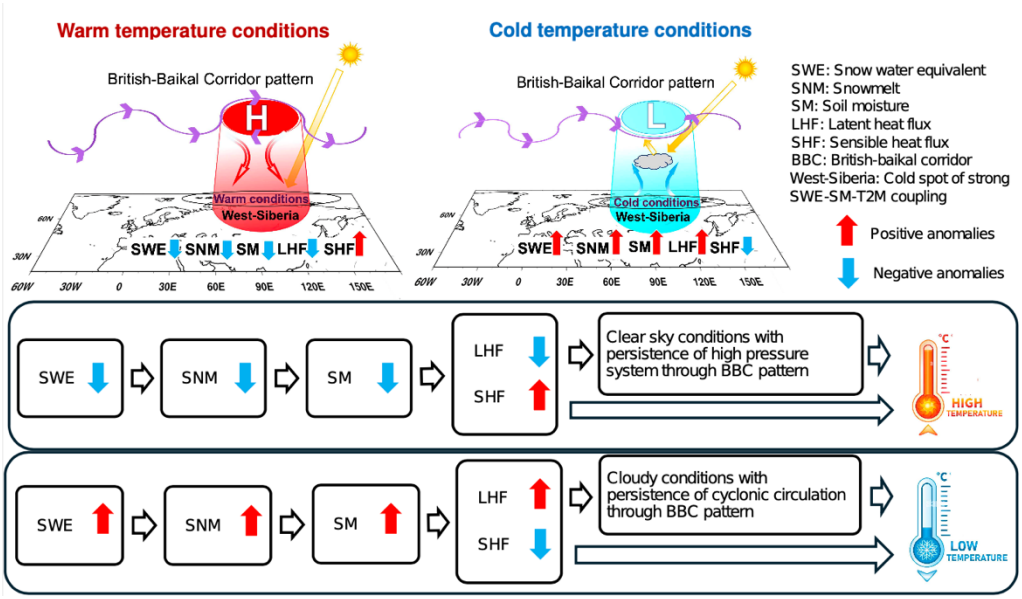

Figure 1) Schematic diagram representing the snow–hydrological processes involved in SWE–SM–T2M coupling.

OMo11

Consideration of Installation Areas for Long-Term Observation with Penetrator Observation Systems in the Antarctic Region

Kodai YAMAMOTO[1], Masa-yuki YAMAMOTO[2], Yasuhiro NISHIKAWA[2] , Satoshi TANAKA[3] , Takamasa HIRATSUKA[1],
[1] *Aerospace Engineering course, Graduated School of Engineering, Kochi University of Technology.*
[2] *School of Systems Engineering, Kochi University of Technology.*
[3] *Department of Solar System Sciences, Institute of Space and Astronautical Science (ISAS), JAXA*

1. Antarctic penetrators

Penetrators are penetration probes. There are pencil-shaped and can be equipped with various observational instruments. We have been developing technologies to enable observations from 'where we can' to 'where we want' using a penetrator, focusing on the Shirase Glacier and the surrounding area since JARE64(64th Japanese Antarctic Research Expedition). There are three elements in a penetrator: penetration, observation and communication. To confirm these elements, we have improved the penetrator observation system and acquired penetration data in JARE64 and JARE65. After these observational experiences, the Antarctic penetrator will finally be installed on the Shirase and Langhovde glaciers by JARE66. It is planned to observe the glacier for about one and a half months. However, the basis of the current penetrator observation system is designed for preventing data loss because of temporarily installing penetrators focusing the event of a disaster. Hence, its observation period may not be sufficient. For penetrators, which are mainly used for standby observations, improving power efficiency has been an important factor. In recent years, technological developments have made it possible to improve the power consumption of the observation system. Therefore, we can now discuss long-term observations of penetrators. In this presentation, we will discuss the possibility of long-term observations when using solar panels.

2.Estimating the number of observation days in the Antarctic region

We have estimated the number of avaiable observation days for our long-term observations. The power resources of the current penetrator are described. The current power consumption of the penetrator is 722 mAh/Day, and the power supply capacity is 22,000 mAh. When we assume a solar panel (with an area of 1 m^2) was attached to the Antarctic penetrator a distribution map of the amount of power generated when the solar panel was installed as a horizontal plane at each site is shown in Figure 1. We estimated how long we could observe from the date of installation (Figure 2). These figures show that the areas where penetrators can be operational for longer periods are concentrated in coastal areas. This means that the observation period is extended for many glaciers and ice shelves.

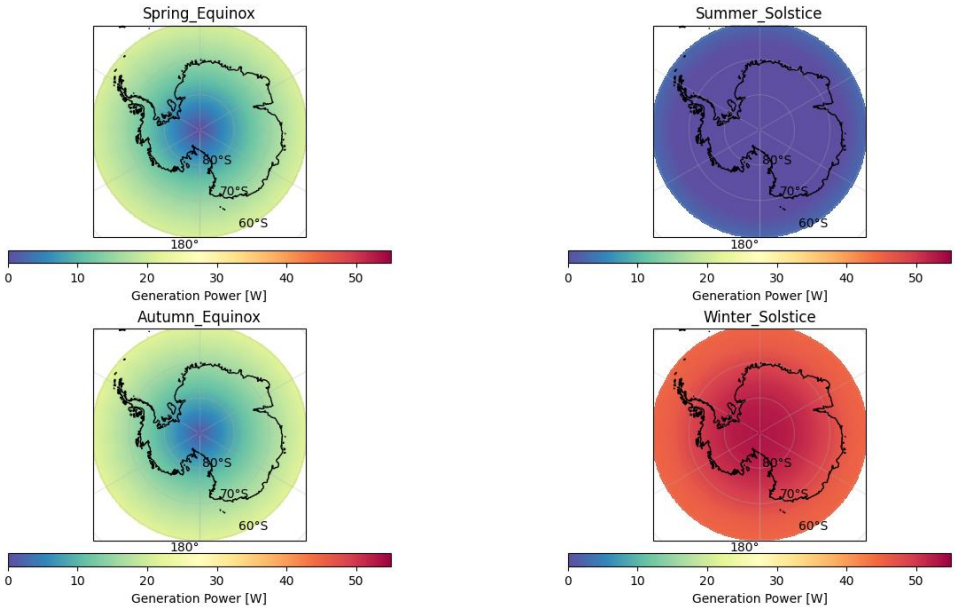

Figure 1. Map of seasonal solar radiation in the Antarctic region.

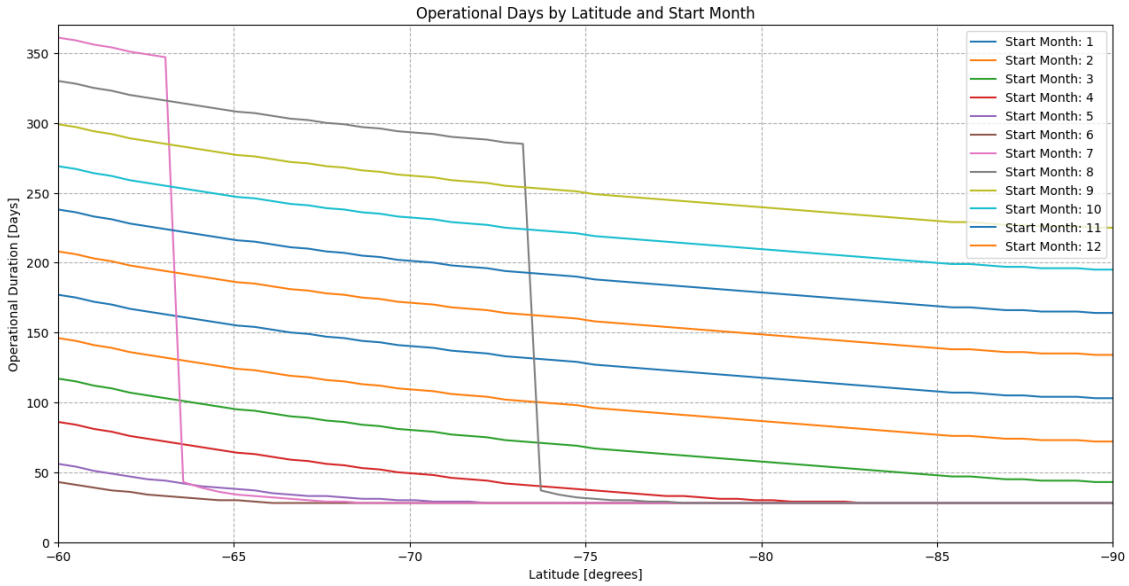

Figure 2. Observation periods in the Antarctic region.

3.Future plan

From these results, the observation period and its range could be estimated. The next step is to consider the factors that can be improved to increase the observation period, such as solar panel area and the power supply capacity. These elements depend on the airframe design. The design that can be improved with the current penetrator shape is to increase the diameter. The advantage of this improvement is that there is less load on the existing on-board equipment. However, this change increases the weight, raises concerns about penetration. To solve this problem, a structural proposal called the afterbody method has been suggested. In this structure, observation equipment such as seismometers is placed in the forebody, while batteries and communication antennas are located in the afterbody. By separating this structure before and after penetration, the reliability of observation and communication is ensured. In the future, we aim to implement the afterbody system in our penetrators. And we want to develop a penetrator that can achieve the four elements of penetration, observation, communication, and energy-generation.

Characteristics of precipitation at Syowa Station, Antarctica

Naohiko Hirasawa[1,2], Hiroyuki Konishi[3], Yasushi Fujiyoshi[4], Masanori Yabuki[5], Katsushi Iwamoto[6]

[1]*National Institute of Polar Research*
[2]*Sokendai (The Graduate University for Advanced Studies)*
[3]*Osaka-Kyoiku University,*
[4]*Emeritus Prof., Hokkaido University,*
[5]*Research Institute for Sustainable Humanosphere, Kyoto University*
[6]*Fisheries Research Division, City of Mombetsu, Hokkaido*

Major precipitation events in the Antarctic coastal region, including Syowa Station, is often accompanied by strong winds and consequent blowing snow, making it difficult not only to accurately measure the amount of precipitation on the ground, but also to even detect the presence and/or the temporal variability of precipitation. We conducted X-band Doppler radar observations at Syowa Station, Antarctica in April 2021-November 2022. The observation successfully showed the intensity of precipitation above blowing snow with strong winds all over the observation period. Moreover, Hirasawa et al. (2021)[R1] discussed that the radar was capable of weak precipitation of about 0.01 mm/hr in some cases with weak winds, when we evaluated the precipitation intensity by a disdrometer (LPM, manufactured by Thies Co.Ltd., Germany).

This presentation will discuss the characteristics of precipitation at Syowa Station with precipitation intensity evaluated from radar reflection intensity (RRI). The RRI is related to precipitation intensity through the so-called Z-S relationship, which is obtained by comparing the RRI to the measured precipitation intensity (snowfall intensity). The Z-S relationship is currently under examination as presented by Konishi et al. (2023) [R2] at this symposium last year. The first conclusions are expected by the end of September this year. Then discussions based on the evaluated precipitation intensities will be possible. Hereafter in this abstract, RRI will be referred to as precipitation intensity.

The precipitation intensity sampled every 3 hours from about the 1.5 years of observations were ordered by intensity. We focused on events that produced precipitation in the top 10% of those events as major events. Major events occurred three times in one month period at the most, and sometimes did not appear for about three months at the least. It seems difficult to find seasonality in the frequency of major events in this observation period. However, some common characteristics were found in synoptic-scale circulation fields at the time of the appearance of major events. In most cases, a deep trough existed to the west of the Syowa Station. In some cases, a blocking ridge appeared on the east side of the Syowa Station, and in these cases, there appeared to be a tendency for the precipitation period to be prolonged. Previous studies (e.g., Hirasawa et al., 2000 [R3]) have shown that blocking ridges cause major precipitation over the Antarctic ice sheet, and the present results provide a clue to understanding the mechanism that separate precipitation over coastal areas and ice sheets.

References

R1. Hirasawa et al. (2022): Okhotsk Sea and Polar Oceans Research, 6, 36-41. doi.org/10.57287/ospor.6.36

R2. Konishi et al. (2023): The 14th Symposium on Polar Science, NIPR, Tokyo.

R3. Hirasawa et al. (2000): Geophys. Res. Lett., 27, 1911-1914. https://doi.org/10.1029/1999GL011039

OMo13

The Spatial Structure of Atmospheric Rivers observed in the JARE64

Kazu Takahashi[1], Kazutoshi Sato[2,1], Jun Inoue[2,1] and Naohiko Hirasawa[2,1]
[1]*The Graduate School of Advanced Studies, SOKENDAI*
[2]*National Institute of Polar Research, NIPR*

Recently, Atmospheric River (AR) has been focused on because of its impact on the Antarctic Ice Sheet Mass Balance. ARs are generally associated with extra-tropical cyclones with the frontal system. Typical ARs are located ahead of the cold front and constructed by low-level jets and moisture-laden air mass in the warm sector of extra-tropical cyclones, transporting an amount of sensible heat and moisture to high latitudes. It is crucial that ARs-transporting moisture accounts for more than 90% of southward transported moisture (Zhu and Newell, 1998; Nash et al., 2018) and sometimes intrudes into Antarctica. Over the open water and sea ice of the Southern Ocean, moisture climatologically be concentrated in the lower troposphere near the surface, and humidity inversion layers occur only 19% of the time in austral summer (Naakka et al., 2021). Naakka et al. (2021) explained that the formation of a moisture inversion layer is substantially related to the southward advection of an oceanic humid air mass at higher altitudes. Over the Southern Ocean, the individual southward moisture transport from lower latitudes is lifted up to the higher altitudes along almost the surface of the monthly mean equivalent potential temperature, resulting in intrusion into the Antarctic inland (Bailey et al., 2019). Such a feature of southward moisture transport, which is caused by synoptic-scale phenomena such as the extratropical cyclone and forms AR, indicates the moisture passing through above the middle altitude and intruding Antarctica. On the other hand, it has been reported that the significant increase in southward moisture transport in the lower troposphere (below 800hPa) contributing to the Antarctic surface mass balance in the Antarctic coastal region is attributed to the AR (Gorodetskaya et al., 2020). To clarify the substantial contribution of ARs to the Antarctic ice sheet, it needs to be well-known how the spatial structure of moisture transport within AR contributes to the Antarctic inland. This study will focus on the features of moisture transport within AR observed during the 64th Japanese Antarctic Research Expedition (JARE64) in the Antarctic coastal region.

The JARE64 cruise was conducted from November 2022 to March 2023 over the Southern Ocean and the Antarctic coastal regions onboard Research Vessel (R/V) *Shirase*. The improved AR detection algorithm originally developed by Zhu and Newell (1998), which is based on the threshold determined by the zonal anomaly of the integrated water vapor transport, was performed for the cruise period with the European Center for Medium-Range Weather Forecasts reanalysis version 5 (ERA5) (Herbach et al., 2020). As a result, it was found that ARs passed over the R/V Shirase 6 times from December 2022 to February 2023. A shipboard microwave radiometer (MWR, Humidity And Temperature PROfilers (HATPRO): Radiometer Physics GmbH Co., Germany) showed that every AR passing occurred with a rapid increase in IWV within the troposphere. Radiosonde observations (RS-11G: Meisei Electric Co., Ltd., Japan), which were operated on the R/V Shirase and at Syowa station under the condition of occurring 5 of the ARs during the JARE64 cruise between December 2022 and March 2023, indicate that the increases in moisture in the middle troposphere. The spatial structure (the vertical structure from radiosonde observations and the horizontal structure from ERA5) of AR passing over the R/V *Shirase* will be compared.

Figure 1 shows the vertical structure of specific humidity, the contribution rate of water vapor to IWV, the zonal moisture transport, and the meridional moisture transport observed at 14UTC on 22nd February, when AR is passing over the R/V *Shirase*. The specific humidity profile has an inversion layer of about 700hPa, rapidly

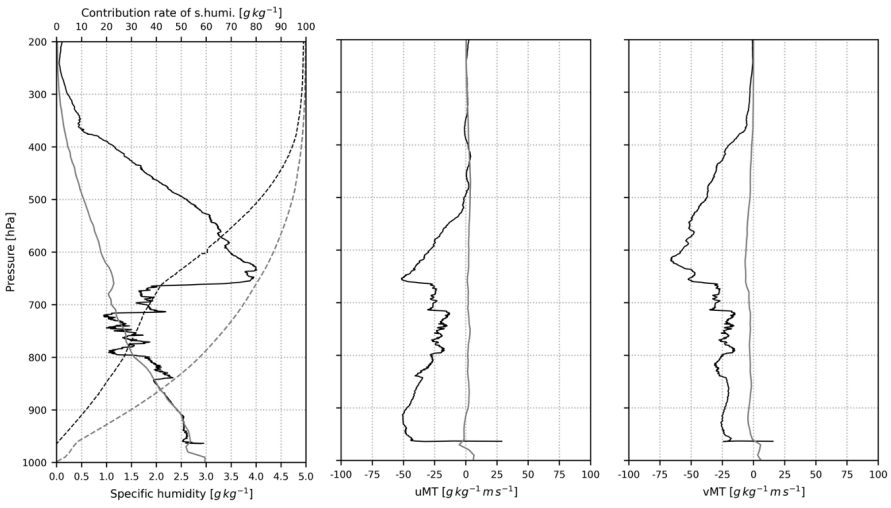

Figure 1 The vertical profiles of (a) specific humidity (solid, g/kg) and the contribution rate of water vapor to the IWV below each level (dashed, %), (b) the zonal moisture transport, and (c) the meridional moisture transport at 1300 UTC on 22 February (black) and mean of all radiosonde observations (gray) on the R/V *Shirase*.

increasing from 2.0 g/kg in the lower layer to 4.0 g/kg maximum at about 650hPa. While the zonal moisture transport is dominated near the surface due to the low-level jet, the moisture inversion contributes to the fact that the southward moisture transport is maximum at the middle altitude. Although the other radiosonde observations released in ARs also indicate the moisture inversions and/or increases in moisture in middle altitude with the southward moisture transports, the maxima of specific humidity and southward moisture transport are located from the surface to 800hPa. In this case, the contribution rate of water vapor below each altitude to IWV shows that only 40% of IWV is concentrated below 700hPa, where the moisture inversion layer exists, indicating that the air mass in the middle of the troposphere was considered a primary source of IWV. Even though other observations during the JARE64 cruise and reported by Gorodetskaya et al. (2020) have not found such a low contribution of lower tropospheric moisture to IWV, all contribution rates during AR in the lower troposphere are lower than that of mean during the JARE64. This means that the increase in moisture above the middle troposphere is more than that in the lower troposphere. It probably is an important finding that the ARs likely contribute to the increase in moisture at the middle altitude more than that in the lower troposphere. Figure 2 shows the latitude-altitude section of the ratio of the zonal and ARs mean specific humidity anomaly from the climatological mean from December to March for 45 years. The unit of the value is dimensionless because the value is divided by the climatological values. This indicates that the increase in moisture is more significant above the middle troposphere than in the lower troposphere. This likely results in the contribution rates observed by radiosondes. In the presentation, we will focus on and show the differences in the vertical and horizontal structures between ARs observed during the JARE64 each other in detail.

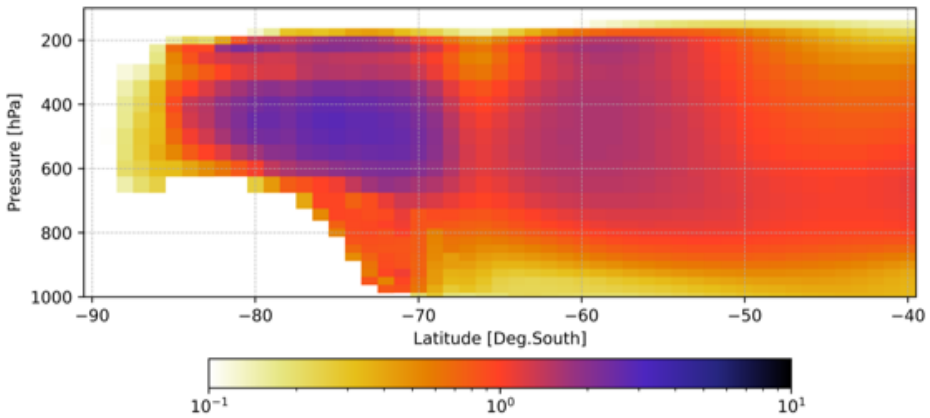

Figure 2. The latitude-altitude section of the zonal and ARs mean specific humidity anomaly within AR from climatological mean from December to March for 45 years between 1979 and 2023. The values are dimensionless because the values were divided by the climatological mean. Negative values and zeros (including the Antarctic continent) are shown in white color.

References

Bailey, A., Singh, H. K., and Nusbaumer, J. (2019). Evaluating a moist isentropic framework for poleward moisture transport: Implications for water isotopes over Antarctica. Geophysical Research Letters, 46(13), 7819-7827.

Gorodetskaya, I. V., Silva, T., Schmithüsen, H., and Hirasawa, N. (2020). Atmospheric river signatures in radiosonde profiles and reanalyses at the Dronning Maud Land coast, East Antarctica. Advances in Atmospheric Sciences, 37, 455-476.

Hersbach H, Bill, B., and 41 others (2020): The ERA5 global reanalysis. Quart. J. Roy. Meteor. Soc. 2020; 146:1999–2049.

Naakka, T., Nygård, T., and Vihma, T. (2021). Air moisture climatology and related physical processes in the Antarctic on the basis of ERA5 reanalysis. Journal of Climate, 34(11), 4463-4480.

Nash, D., Waliser, D., Guan, B., Ye, H., and Ralph, F. M. (2018). The role of atmospheric rivers in extratropical and polar hydroclimate. Journal of Geophysical Research: Atmospheres, 123(13), 6804-6821.

Zhu, Y., and Newell, R. E. (1998). A proposed algorithm for moisture fluxes from atmospheric rivers. Monthly Weather Review, 126(3), 725–735.

Acknowledgment

Dr. Shingo Shimizu (National Research Institute for Earth Science and Disaster Resilience: NIED) contributed to the observation of the microwave radiometer for the 64th JARE.

OMo14

Warming in the Dome Fuji region of East Antarctica driven by strengthening of the Indian Ocean subtropical front

Naoyuki Kurita[1], Takao Kameda[2] , Naohiko Hirasawa[3], Hideaki Motoyama[3], David Mikolajczyk[4], Linda Keller[4],George Weidner[4], Lee Welhouse[4] and Matthew Lazzara[4,5]

[1]*Nagoya University, Japan*

[2] *Kitami Institute of Technology, Japan*

[3]*National Institute of Polar Research, Japan*

[4]*University of Wisconsin-Madison, USA*

[5]*Madison Area Technical College, USA*

The East Antarctica has shown little warming in recent decades, in stark contrast to the warming trends observed in the Antarctic Peninsula and in the West Antarctica. However, the available observations are currently sparse and of short duration, and changes in surface air temperature (SAT) in the East Antarctic interior remain uncertain. Here we present a 30-year long temperature record for the three stations (Dome Fuji, Relay Station, and Mizuho) in the interior of Dronning Maud Land (DML). The observations have been corrected and the missing observations have been estimated with the help of the corrected temperature data from the ERA5 reanalysis. The record shows a statistically significant warming trend of 0.5 deg-C /decade over the period 1993 – 2022. The strong warming during the warm season (from October to the following March) is the main reason for this trend. The interannual variability of warm season temperature is consistent with negative/positive pressure anomalies over the East Antarctica, as is the positive/negative phase of SAM. However, the warming is in the opposite direction to the SAM trend, which has shifted into its positive phase. Interestingly, the variability of the warm season temperature is positively and negatively correlated with the SST in the subtropical and mid-latitude southern Indian Ocean (Fig1a). Thus, the meridional SST gradient in the subtropical oceanic frontal zone (STFZ) between the subtropical and mid-latitude of the southern Indian Ocean has a clear relationship with the warm season temperatures (Fig.1c). In addition, the SST gradient in the STFZ is increasing since the southern Indian Ocean has been warming rapidly over the last a few decades (Fig.1b). This positive trend is consistent with the warming in the interior DML. It is well known that the intensification of the subtropical oceanic front (STF) changes the atmospheric circulation through air-sea interactions. Regression to the STFZ anomaly shows a clear north-south dipole pattern of the Z300 anomalies, with an area of low pressure over the south of the STFZ, and an area of high pressure over the Enderby Land in East Antarctica. High pressure anomalies over the Enderby Land promote warm air advection to the Dome Fuji region. This pattern can be explained by the atmospheric responses to the strengthening of the STF. Thus, we can say that the strengthening STF is largely responsible for the recent warming trend in the Dome Fuji region. The fact that the recent warming of the Indian Ocean is attributed to the absorption of more excess heat from the atmosphere implies that warming in the subtropical Indian Ocean is further strengthening the STF and may lead to further warming in the Dome Fuji region.

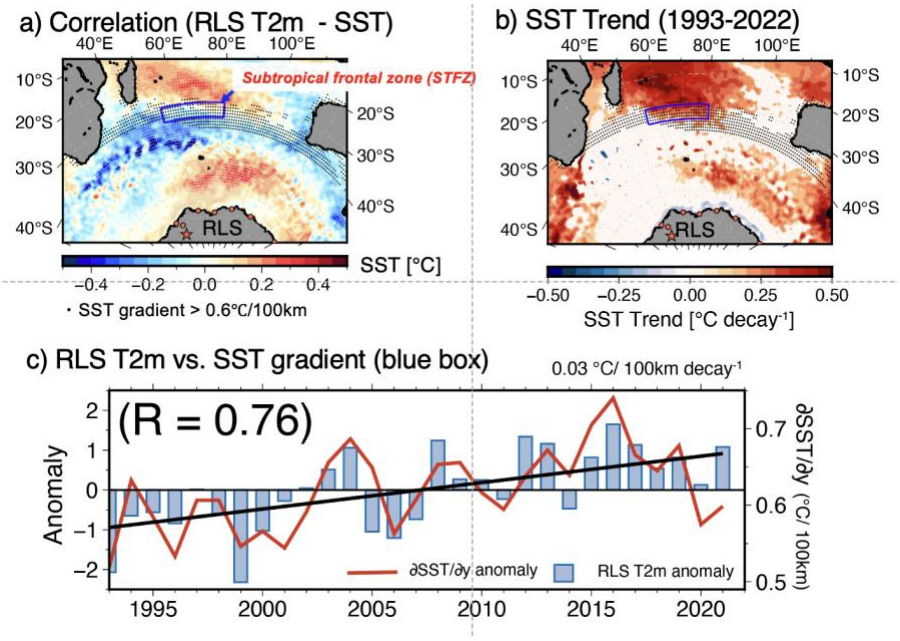

Figure 1. a) Regressions of SST onto Relay Station temperature from 1993-2022. b) Trend of the SST over the southern Indian Ocean. c) Time series of the surface air temperature anomalies at Relay Station and the mean SST gradient in the STFZ (blue box).

References

Kurita, N. *et al.* Near-Surface Air Temperature Records over the Past 30 Years in the Interior of Dronning Maud Land, East Antarctica. *J. Atmos. Ocean. Technol.* **41**, 179–188 (2024).

OMo15

A multi-phase spin-up method for the Greenland ice sheet, and its influence on future changes of the ice sheet

Ralf Greve[1,2] and Félix Grandadam[3,1]

[1]*Institute of Low Temperature Science, Hokkaido University, Sapporo, Japan*
[2]*Arctic Research Center, Hokkaido University, Sapporo, Japan*
[3]*Claude Bernard University Lyon 1 and ECL Engineering School, Lyon, France*

Ice sheets play a critical role in the Earth's climate system, and their evolution is closely linked to the global temperature and sea level. Numerical modelling has become an important tool for estimating the contribution of the Earth's ice sheets to sea-level rise over the coming centuries. Such simulations depend on reasonably accurate initial conditions of the recent 3D dynamic/thermodynamic state of the ice sheet in question. Since observational data are limited, numerical tools are required to obtain these initial conditions, which can be classified into assimilation methods and spin-up methods [1,2].

Here, we use the ice-sheet model SICOPOLIS v24 [3] to carry out a multi-phase spin-up for the Greenland ice sheet (GrIS) [4,5]. It consists of the following steps: (1) a 100-ka steady-state calibration phase that includes preliminary tuning of the basal sliding coefficient, (2) a freely evolving glacial phase from the Eemian interglacial until the Last Glacial Maximum (LGM), (3) a deglaciation phase from the LGM until the early Holocene that includes topography-nudging to produce an ice-sheet configuration close to present day, (4) a freely evolving Holocene phase from the early Holocene until today, during which further tuning of the basal sliding coefficient is carried out. This produces a present-day ice sheet (Fig. 1) that includes the thermal, sea-level, and glacial-isostatic-adjustment signals.

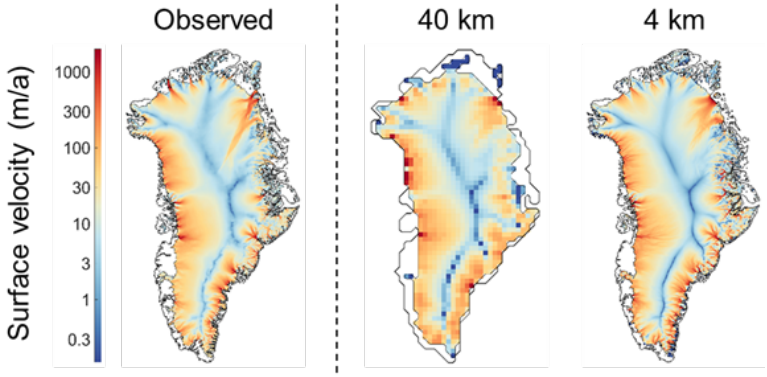

Figure 1: Observed (left) vs. simulated (right) surface velocity of the present-day GrIS. Hybrid shallow-ice–shelfy-stream dynamics, a Weertman-Budd-type sliding law with sub-melt sliding and basal hydrology, ice thermodynamics based on a polythermal enthalpy method, and two different resolutions (low/40 km, high/4 km) were employed. The agreement between the observed data and the high-resolution spin-up is good.

We will use the initialized ice sheet to carry out selected simulations into the future. We will test the influence of different ice-dynamics schemes (hybrid shallow-ice–shelfy-stream [6] vs. DIVA [depth-integrated viscosity approximation; Ref. 7] dynamics) on the simulated future change of the GrIS.

References

[1] Goelzer et al., 2018, Cryosphere 12, 1433-1460, doi: 10.5194/tc-12-1433-2018. [2] Seroussi et al., 2019, Cryosphere 13, 1441-1471, doi: 10.5194/tc-13-1441-2019. [3] SICOPOLIS Authors, 2024, GitLab @ AWI (Bremerhaven, Germany), https://git-lab.awi.de/sicopolis/sicopolis. [4] Berends et al., 2023, EGU General Assembly, EGU23-14236, doi: 10.5194/egusphere-egu23-14236. [5] Bernales et al., 2023, EGU General Assembly, EGU23-14648, doi: 10.5194/egusphere-egu23-14648. [6] Bernales et al., 2017, Cryosphere 11, 247-265, doi: 10.5194/tc-11-247-2017. [7] Lipscomb et al., 2019, Geosci. Model Dev. 12, 387-424, 2019, doi: 10.5194/gmd-12-387-2019.

How vegetation feedback for the future and the past (LIG) climate affects the Greenland ice sheet?

Ryouta O'ishi[1], Fuyuki Saito[2], Wing-Le Chan[1], Takashi Obase[2] and Ayako Abe-Ouchi[123]
[1]Atmosphere and Ocean Research Institute, the University of Tokyo
[2]JAMSTEC
[3]NIPR

Sea level rise is an important topic in future climate projections. In the past warm period known as the Last Interglacial (LIG), paleoclimate records indicate a sea level rise of several meters. The most important characteristic of the LIG is summer solar irradiance induced by the Earth's orbit different to that of the present-day. The peak of summer solar irradiance at 65N is more than 70W/m^2 in the LIG than the present-day, which affects the surface mass balance ot fhe Greenland Ice Sheet.

Within the paleoclimate modeling community, researchers have applied past GCM results to ice sheet models and attempted to reproduce past sea levels. A recent study revealed that atmosphere-ocean-sea-ice-vegetation feedback plays an important role in the Arctic climate (O'ishi et al. 2021). Vegetation changes in the northern high latitudes occur in response to stronger summer solar irradiance in the LIG, which amplifies Arctic warming through interseasonal ocean and sea-ice feedback. This result also indicates that not only the summer solar irradiance but also vegetation changes affect the response of the Greenland Ice Sheet in the LIG.

In the present study, we use the results of LIG experiments with MIROC4m (without vegetation feedback; Hasumi and emori 2004) and MIROC4m-LPJ (with vegetation feedback; O'ishi et al. 2021) as input to a 3-dimensional ice sheet model, IcIES (Saito et al. 2016), to evaluate the effect of vegetation changes upon the Greenland Ice Sheet. We also apply the result of doubled CO_2 experiments with MIROC4m and MIROC4m-LPJ to investigate the effect of vegetation feedback induced by CO2 concentration.

References

Hasumi, H. and Emori, S.: K-1 Coupled GCM (MIROC) Description, k-1 Technical Report No. 1, Center for Climate System Research (CCSR, Univ. of Tokyo), National Institute for Environmental Studies (NIES), Frontier Research Center for Global Change (FRCGC), Tokyo, Japan, 2004.

Saito, F., Abe-Ouchi, A., Takahashi, K., and Blatter, H.: SeaRISE experiments revisited: potential sources of spread in multi-model projections of the Greenland ice sheet, The Cryosphere, 10, 43–63, https://doi.org/10.5194/tc-10-43-2016, 2016.

O'ishi, R., Chan, W.-L., Abe-Ouchi, A., Sherriff-Tadano, S., Ohgaito, R., and Yoshimori, M.: PMIP4/CMIP6 last interglacial simulations using three different versions of MIROC: importance of vegetation, Clim. Past, 17, 21–36, https://doi.org/10.5194/cp-17-21-2021, 2021.

What determines the sweet spot of Dansgaard Oschger events?

Ayako Abe-Ouchi[1], Wing-Le Chan[1], Sam Sherriff-Tadano[2], Yuta Kuniyoshi[1], Takashi Obase[3], Takahito Mitsui[1]
[1]*AORI, The University of Tokyo*
[2]*Ryukyu University*
[3]*JAMSTEC*

Glacial periods were punctuated by abrupt millennial scale climate changes, such as Dansgaard Oeschger events, Boeling-Allerod and Younger Dryas. Although glacial abrupt climate changes were shown to have a strong link to the Atlantic Meridional overturning circulation (AMOC) changes and the glacial background climate, simulating the stability and millennial change of AMOC and climate with fully coupled ocean-atmosphere GCM have been challenging. Here we present many cases of millennial scale climate variability with our Atmospheric Ocean coupled GCM, MIROC4m. A series of long transient experiments (> 10, 000 years) were performed systematically with different steady glacial conditions (CO_2 level, obliquity, precession, meltwater, ice sheet size), to study the dependence of the sweet spot of millennial scale variability on the background climate and summarize the results as phase diagrams. We chose the model version which we simulate LGM AMOC weaker and shallower than the AMOC under Pre-Industrial condition. A reasonable sweet-spot of oscillation exists when the Northern Hemisphere ice sheets exist even without freshwater perturbation. In the sweet spot, self-sustained oscillation with bipolar seesaw pattern and shift between interstadial and stadial occur, with interval between abrupt events ranging from 1000 years to more than 5000 years depending on the background condition, while an abrupt shift from stadial to interstadial mode occurs in about 100 years. The sweet spot exists when the CO_2 level is between 260ppm and 185ppm, depending largely on the obliquity but marginally on the precession and ice sheet size. When the obliquity or the CO_2 amount is large (small), the AMOC is in a strong (weak) stable mode of about 18 (10) Sv (Sverdrup). Many aspects of the sweet spot, i.e., the duration of interstadial is longer systematically when the CO_2 or obliquity is larger and the relation between the duration of interglacial and Antarctica air temperature, are very much in agreement with the ice core analysis and the deep-sea sediment.

Significant changes in size distribution of black carbon particles at Dome Fuji over Termination I: Insights from Wide-Range Single-Particle Soot Photometer measurements

Kumiko Goto-Azuma[1], Kaori Fukuda[1], Jun Ogata[1], Nobuhiro Moteki[2], Tatsuhiro Mori[3], Sho Ohata[4], Yutaka Kondo[1]
Makoto Koike[5], Motohiro Hirabayashi[1], Kyotaro Kitamura[1], Ayaka Yonekura[1,6,7], Shuji Fujita[1,6], Fumio Nakazawa[1,6]
Yoshimi Ogawa-Tsukagawa[1], Ikumi Oyabu[1,6] and Kenji Kawamura[1,6]

[1] *National Institute of Polar Research, Japan*
[2]*Tokyo Metropolitan University, Japan*
[3]*Keio University, Japan*
[4]*Nagoya University, Japan*
[5] *The University of Tokyo, Japan*
[6]*SOKENDAI (The Graduate University for Advanced Studies), Japan*
[7]*Present address: Marine Works Japan Ltd., Japan*

Black carbon (BC) particles can affect Earth's radiation budget by absorbing sunlight and reducing the albedo of snow and ice surfaces (e.g., Bond et al.). BC particles can also affect cloud microphysical processes by acting as cloud condensation nuclei (CCN) or ice nucleating particles (e.g., Bond et al., 2013), thereby indirectly affecting the radiation budget. Furthermore, BC emitted from large wild fires can affect air quality and ecosystems. BC can thus affect climate and environment. Climate changes can in turn change frequencies and magnitudes of wild fires and hence BC emissions. Despite numerous studies through observations and aerosol/climate models, we have only limited knowledge on impacts of BC on radiation budget. Our knowledge on impacts of climate change on BC emissions are also limted. Ongoing global warming could impact wild fires. However, predictions are hampered by limted long-term records of natural wild fires. Ice core BC data can provide us with excellent records of the past natural wild fires.

We analyzed the second Dome Fuji deep ice core drilled in East Antarctica for a depth interval between 120 and 640 m, corresponding to the LGM to mid-Holocene period, using a Continuous Flow Analysis (CFA) system developed at the National Institute of Polar Research. The CFA system enabled us to obtain high-resolution data of BC, stable isotopes of water, microparticles and eight elements (Na, Mg, Al, Si, K, Ca, Fe and S). For BC analysis, we used a recently developed Wide-range Single Particle Soot Photometer (WR-SP2), which can detect BC particles in the diameter range between 70 and 4000 nm (Mori et al., 2016). A combination of WR-SP2 and a high-efficiency nebulizer allowed us accurate measurements of size distributions as well as concentrations of BC particles.

We calculated BC mass flux using BC concentration and accumulation rate data. The BC mass flux at Dome Fuji was high during the LGM, decreased over Termination I, and increased again in the early Holocene. This temporal trend contrasts sharply with observations from the WAIS Divide in West Antarctica. Additionally, we found that the average mass of BC particles (mBC), a measure of BC size distribution, changed significantly during Termination I, with mBC values 3-4 times greater during the LGM compared to the Holocene. The size distribution data from Dome Fuji showed a large proportion of BC particles with mass equivalent diameters exceeding 500 nm, which likely contributed to the distinct temporal trends in BC mass flux between Dome Fuji and WAIS Divide, as the upper limit of measurable BC diameters in the WAIS Divide ice core was approximately 500 nm.

References

Bond, T. C. et al., Bounding the role of black carbon in the climate system: A scientific assessment, J. Geophys. Res. Atmos., 118, 5380– 5552, doi:10.1002/jgrd.50171., 2013.

Mori, T. et al., Improved technique for measuring the size distribution of black carbon particles in liquid water, Aerosol Science & Technology, 50, 3, 242-254, DOI: 10.1080/02786826.2016.1147644, 2016.

Development and Application of Hybrid Technology Combining Dielectric Tensor Measurement and Continuous Flow Analysis

Shuji Fujita[1] and Motohiro Hirabayashi[1]
[1]*National Institute of Polar Research, Japan*

In ice core measurement, it is essential to efficiently, rapidly, and continuously analyze long ice cores, ranging from several hundred to several thousand meters, with high resolution. Traditionally, ice core studies distributed the ice core samples among different analysis groups for physical, isotopic, chemical, and gas analysis, often resulting in fragmented and discontinuous analysis. However, by utilizing hybrid technology, we can minimize sample consumption and tackle areas that were previously difficult to analyze. In this presentation, we will introduce the details of this technology.

One of the advanced techniques is the Continuous Flow Analysis (CFA). This technology has been adopted and used by international groups involved in ice core research. In this method, columnar samples (30×30×500mm) are continuously melted from one end for analysis. The target elements include major elements, water isotopes, solid particles (dust), and methane, with an effective resolution of approximately 10mm.

To complement CFA, we have been developing and improving the "Dielectric Tensor Method (DTM)" for analyzing the dielectric properties of ice cores from a crystal physics perspective. In this method, electromagnetic waves are used to reveal the compression and deformation history of each layer, as well as the molecular diffusion processes within the ice. Using a device called a millimeter-wave resonator, we can perform continuous analysis of the polycrystalline ice structure with a resolution of about 15mm.

Recently, the DTM technology has seen significant advancements. Initially, the maximum thickness of the samples that could be measured was 6mm, and the beam irradiation range was limited to a diameter of about 22mm. However, through modifications in the microwave frequency settings, resonator mirror design, and waveguide connection mechanisms, we have increased the measurable sample thickness to 90mm, with an adjustable beam irradiation range of 16 to 40mm. This improvement has greatly expanded the application scope of DTM, allowing us to apply it to columnar samples (30×30×500mm) prepared for CFA.

By using this technology, we can perform non-destructive DTM analysis, followed by CFA on the same sample. This enables comprehensive analysis, including physical, chemical, water isotopic, and gas analysis, all in a single sample preparation process. This hybrid technology is now a valuable standard technique for basic ice core analysis. Additionally, to efficiently prepare columnar samples, we developed a long-stroke microtome capable of shaping up to 10 samples simultaneously. These technological innovations are expected to accelerate ice core research, providing an environment where researchers can allocate more time to their studies. Furthermore, it enables us to extract as much information as possible from the limited and precious ice core samples.

Uptake and Transfer of Heat Within the Firn Layer of Greenland Ice Sheet's Percolation Zone

Jun Saito[1, 2], Joel Harper[1] and Neil Humphrey[3]
[1]*University of Montana, Missoula, MT, USA*
[2] *Institute of Low Temperature Science, Hokkaido University, Sapporo, Japan*
[3] *University of Wyoming, Laramie, WY, USA*

The thermal field within the firn layer on the Greenland Ice Sheet (GrIS) governs meltwater retention processes, firn densification with surface elevation change, and heat transfer from the surface boundary to deep ice. However, there are few observational data to constrain these processes with only sparse in situ temperature time series that do not extend through the full firn depth. Here, we quantify the thermal structure of Western Greenland's firn column using instrumentation installed in an elevation transect of boreholes extending to 30 and 96 m depths. During the high-melt summer of 2019, heat gain in the firn layer showed strong elevation dependency, with greater uptake and deeper penetration of heat at lower elevations. The bulk thermal conductivity increased by 15% per 100 m elevation loss due to higher density related to ice layers. Nevertheless, the conductive heat gain remained relatively constant along the transect due to stronger temperature gradients in the near surface firn at higher elevations. The primary driver of heat gain during this high melt summer was latent heat transfer, which increased up to ten-fold over the transect, growing by 34 MJ m^{-2} per 100 m elevation loss. The deep-firn temperature gradient beneath the seasonally active layer doubled over a 270-m elevation drop across the study transect, increasing heat flux from the firn layer into deep ice at lower elevations. Our in situ firn temperature time series offers observational constraints for modeling studies and insights into the future evolution of the percolation zone in a warmer climate.

Terminus dynamics of Taku Glacier, Alaska, during the recent transition

Arlec Chang[1,2], Shin Sugiyama[2], Jason Amundson[3], Lynn Kaluzienski[3] and Ian Joughin[4]
[1]*Institute of Low Temperature Science, Hokkaido University*
[2]*Graduate School of Environment Science, Hokkaido University*
[3]*University of Alaska Southeast*
[4]*University of Washington*

Ice loss from Alaskan glaciers accounted for 25 % of the total loss from global mountain glaciers between 2000 and 2019 (Hugonnet et al., 2021). Importantly, 14 % of the ice loss in Alaska is from tidewater glaciers, which may advance and retreat independent from climate conditions. While most glaciers in Alaska retreated during the period, Taku Glacier, the largest outlet glacier in the Juneau Icefield, had been advancing throughout the 20th century and first part of the 21st century. However, it started to show retreating signs around 2015. In this study, we quantified changes in terminus position, surface elevation and surface velocities in order to better understand the dynamics during the glacier's transition from advance to retreat, utilising satellite data (Landsat 4, 5, 7, 8, 9 and Sentinel-2 imageries, ArcticDEM Strips). As a result, terminus position illustrated spatial and temporal variabilities from 1984–2024 (Figure 1), with a significant retreat (~ −217 m) observed in the east section from 1984–1998 while the rest of the terminus advanced. Moreover, advancing rate in 1998–2015 was not uniform along the frontal margin, larger in the middle section, 14.7 m a^{-1}, and relatively smaller in the east and west sections, 8.7 m a^{-1} and 5.4 m a^{-1}, respectively. As regards surface elevation change, surface lowering was observed across the study area between 2014 and 2021, with a significantly large magnitude near the glacier margins, up to −30 m in the west section (Figure 2). In addition, seasonal variations in surface flow speed were noticeable in the western area, reaching a maximum of 0.73 m d^{-1} in summer and hitting a minimum of 0.28 m d^{-1} in winter. On the contrary, seasonal signal was less obvious in the eastern area, which fluctuated between 0.25 and 0.39 m d^{-1}.

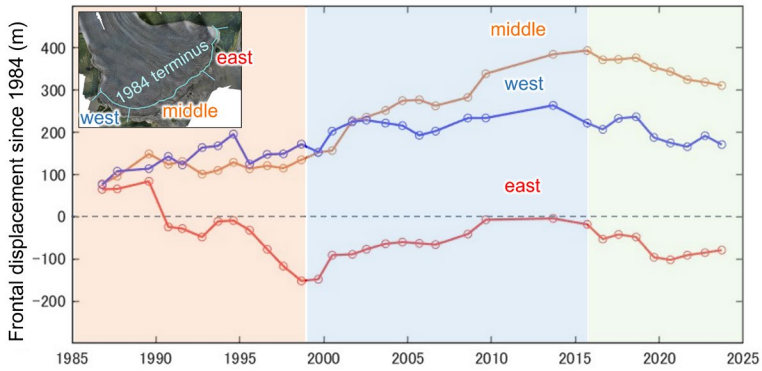

Figure 1. Frontal displacement in the west, middle, and east sections since 1984. The inset indicates the area of the three sections.

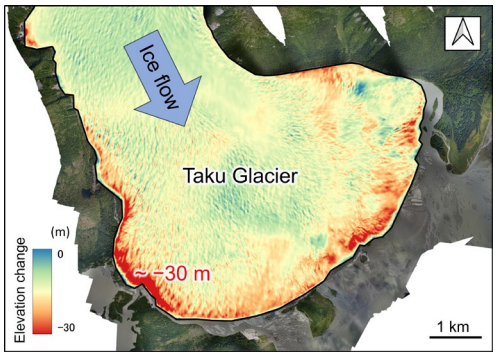

Figure 2. Change in surface elevation from June 2014 to June 2019. The background is an orthomosaic photo derived from an aerial survey in August 2015.

References

Hugonnet R., McNabb R., Berthier E., Menounos B., Nuth C., Girod L., Farinotti D., Huss M., Dussaillant I., Brun F., Kääb A., Accelerated global glacier mass loss in the early twenty-first century, Nature 592, 726–731, 2008.

McNeil C., O'Neel S., Loso M., Pelto M., Sass L., Baker E.H., Campbell S., Explaining mass balance and retreat dichotomies at Taku and Lemon Creek Glaciers, Alaska, Journal of Glaciology 66(258), 530–542, 2020.

Ritchie J.B., Lingle C.S., Motyka R.J., Truffer M., Seasonal fluctuations in the advance of a tidewater glacier and potential causes: Hubbard Glacier, Alaska, USA, Journal of Glaciology 54(186), 401–411, 2018.

Zechmann J.M., Truffer M., Motyka R.J., Amundson J.M., Larsen C.F., Sediment redistribution beneath the terminus of an advancing glacier, Taku Glacier (T'aakú Kwáan Sít'i), Alaska, Journal of Glaciology 67(262), 204–218, 2020.

OMo22

Recent advances of the development of software-defined-radio-based radio echo sounder for ice thickness measurement of glaciers

Taishi Hashimoto[1], Masahiro Minowa[2], Hiroto Sakata[2], Kazuhiko Mushiake[3], and Masahiko Mushiake[3]
[1]*National Institute of Polar Research*
[2]*Hokkaido University*
[3]*Ilohas Project Co., Ltd.*

Recently, Antarctic ice sheets are losing mass due to global warming [1]. To accurately evaluate the decrease in mass and understand its mechanisms, measuring the thickness and movement of ice sheets is necessary.
Among the numerous techniques, airborne ice radar is the most reliable and efficient means of measuring ice thickness and landforms in a wide area [2]. Several airborne surveys have been conducted in vast areas of Antarctica so far. However, the published dataset is still sparse, especially in East Antarctica. The landform under the ice is poorly measured in these areas, and the estimated variation of ice-sheet mass could be inaccurate [3].

Based on this motivation, we have been developing a compact radio echo sounder (RES) for helicopter-borne operation in the glaciers around Syowa Station. Our radar system is based on a software-defined-radio (SDR) platform called Red Pitaya [4]. We have improved the radar system this year, and are now testing it at Perito Moreno Glacier, Patagonia.

This presentation will explain the current status of the development of our SDR-based RES system and the plans for successive radar experiments.

References

[1] Smith et al., Pervasive ice sheet mass loss reflects competing ocean and atmosphere processes, Science, 2020.
[2] Schroeder et al., Five decades of radioglaciology, Annals of Glaciology, 2020.
[3] Matsuoka et al., Circling Antarctica to Unveil the Bed Below Its Icy Edge, EOS, 2022.
[4] Red Pitaya - Swiss army knife for engineers, https://redpitaya.com/.

Physical Sciences Group of SCAR

Takuji Nakamura[1,2] , Adriana M. Gulisano[3], Wojciech Miloch[4], and Juhi Yadav[5] ,
[1]*National Institute of Polar Research (NIPR), Tachikawa, Tokyo, Japan*
[2] *The Graduate University for Advanced Studies, SOKENDAI, Japan*
[3]*Instituto Antártico Argentino/Dirección Nacional del Antártico, Buenos Aires, Argentina*
[4] *University of Oslo, Oslo, Norway*
[5]*National Centre for Polar and Ocean Research, Ministry of Earth Sciences, Vasco-da-Gama, Goa, India*

The Physical Sciences Group (PSG) of SCAR (Scientific Committee on Antarctic Research) is one of the three science groups in SCAR, and is dedicated to investigating the critical processes at the interfaces between ice, ocean, land, and atmosphere, including climate change responses. The group focuses on enhancing the comprehension of ice sheet dynamics, extracting historical climate data from ice cores, exploring the sea ice and ocean circulation changes. It also aims to develop a better understanding of the atmospheric dynamics and chemistry, particularly the ozone hole's impact on Antarctic climate. Additionally, Antarctica's unique conditions—such as its dry, cold, and wind-free environment— make it an exceptional platform for astronomical and solar-terrestrial observations, providing valuable insights into space science and global climate processes.

The poster presentation introduces 15 subgroups under PSG and highlights of their activities.

OMp2

The role of Nicolaus Copernicus University Polar Station in long-term cryosphere monitoring, Svalbard

Ireneusz Sobota
Nicolaus Copernicus University in Toruń, Department of Hydrology, Cryology and Water Management, Polar Research Center, Poland

The Nicolaus Copernicus Polar Station is located in the western part of Oscar II Land north of the Kaffiøyra coastal plain, bordering on Forlandsundet in the west. The station was established in Heggodden, about 150 metres from the seashore, at the terminal moraines of the Aavatsmarkbreen. The NCU Polar Station can accommodate up to fifteen people at a time. There is a main room, a workshop, a bedroom, two mezzanine sleeping areas, a fully equipped kitchen, a lab, and a bedroom. There are also additional storage areas, another lab, a bathhouse, a lavatory, and garages.

The primary role of Nicolaus Copernicus University Polar Station is initiating and leading interdisciplinary research in polar regions and other glaciated areas, encouraging multidisciplinary research projects, cooperation with Polish and foreign polar research institutions and collaboration with non-academic partners interested in polar research and exploration.

The station has all the necessary technical equipment, such as generator sets, photovoltaic cells, automatic weather stations and motor boats. Some of the most important scientific equipment includes an automatic weather station which can run all year round and is equipped with climatological-station-grade measuring instruments; stream gauges, limnimeters and data loggers used for water stage and flow rate measurements and observations of selected physical and chemical properties of the water. Although the NCU Polar Station operates for only three to four months a year, it is designed and equipped to provide a base for continuous operation throughout the year.

Research in Svalbard has covered all components of the geographic environment, but with a particular focus on glaciology, glacial geomorphology, permafrost and periglacial processes, and climatology. The studies cover the mass balance of glaciers, glacier geometry change processes, glacier dynamics, glacier surge, glacier-climate interactions, polar hydrology, and Thermal structure of the near-surface glacier layer.

The results of glaciological, meteorological and permafrost studies /cryosphere changes/ have made it possible to obtain some of the most extended data series available for Svalbard today. Currently, monitoring contemporary changes in the cryosphere and standard meteorological observations are being conducted, including using an automatic weather station operating all year round.

Figure 1. Nicolaus Copernicus Uniwersity Polar Station on Svalbard in 2024.

Spatiotemporal high-resolution dynamics of ocean acidification in the global ocean

Y Cai[1*], BF Li[2], XL Pan[2] and YW Watanabe[2]

[1]*Graduate School of Environmental Science, Hokkaido University, Sapporo, Japan*
[2]*Faculty of Environmental Earth Science, Hokkaido University, Sapporo, Japan*

The global ocean is estimated to absorb about one quarter of the CO_2 from anthropogenic emissions, which could lead to ocean acidification manifested as a gradual decrease in seawater pH [*Le Quéré et al.*, 2015]. To understand the impact of anthropogenic CO_2 emission to the ocean, it is necessary to clarify its contribution to ocean carbon chemistry. It may not only be affected by anthropogenic influences, but also by changes with internal and external natural processes. Therefore, it is essential to distinguish between natural and anthropogenic components from the observed data in order to elucidate the current status of ocean acidification throughout the ocean from the surface to the seafloor. We here tried to distinguish between the natural and anthropogenic components from the observed ocean acidification in the global ocean. We used a 'hybrid' parameterization method which consists of Multiple Linear Regression (MLR) to find appropriate parameters and Neural Network (NN) to predict oceanic pH with high-resolution gridded data based on the ship-based observed datasets (GLODAPv2.2022), following the approach of *Watanabe et al.* [2018] and *Pan et al.* [2020, 2022, 2023]. On the day of the presentation, we will discuss quantitatively the natural and anthropogenic components of ocean acidification in the global ocean.

References

Le Quéré *et al.* Global carbon budget 2015, *Earth Syst. Sci. Data*, **7**(2), 349–396, 2015.

Watanabe, Y.W. *et al*. Long-term trends of direct and indirect anthropogenic effects on changes in ocean pH. *Geophys. Res. Lett.*, **45**, 9106–9113, 2018.

Pan, X. L. *et al*. The Southern Ocean with the largest uptake of anthropogenic nitrogen into the ocean interior. *Sci. Rep*., **10**, 8838, 2020.

Pan, X.L. *et al*. Intense ocean freshening from melting glacier around the Antarctica during early twenty-first century. *Sci Rep*, **12**, 383, 2022.

Pan, X.L. *et al.* Spatiotemporal high-resolution mapping of biological production in the Southern Ocean. *Commun Earth Environ* **4**, 488, 2023.

Hybrid parameterization of CO_2 disequilibrium over the global ocean

Li BF[1*], Cai Y[2], Watanabe YW[1]

[1] *Fac. Env. Earth Sci., Hokkaido Univ., Sapporo, Hokkaido, Japan*

[2] *Grad. Sch. Env. Sci., Hokkaido Univ., Sapporo, Hokkaido, Japan*

CO_2 has difficulty reaching equilibrium immediately at the air-sea interface, and CO_2 in the newly produced deep-water masses is always transported into the ocean interior in a disequilibrium state. The detailed global spatial distribution of the disequilibrium is yet unknown, leading to a large uncertainty for estimating oceanic anthropogenic CO_2. To overcome this issue, we obtain the detailed disequilibrium of CO_2 in the surface mixed layer by a new hybrid parameterization based on multiple linear regression (MLR) and neural network (NN) (*Pan et al*., 2023). Appling this hybrid parameterization to the ship based hydrographic data set, we found a large CO_2 disequilibrium in the polar regions. Furthermore, applying this parameterization to ocean robotic profiling floats (e.g., biogeochemical Argo) in the ocean, we drew the seasonal variation of oceanic disequilibrated and anthropogenic CO_2 spatiotemporally.

References

Pan XL, Lai, X, Makabe R, Hirano D, Watanabe YW (2023): Spatiotemporal high-resolution mapping of biological production in the Southern Ocean. *Communications Earth & Environment*, 4, 488 (2023), doi: https://doi.org/10.1038/s43247-023-01067-y.

OMp5

Variation of carbonate chemistry for brine in the Arctic sea ice by mixing with the ice/snow meltwater during melting season

Masaki Yoshimura[1], Daiki Nomura[1, 2, 3], Taichi Noshiro[1], Hiroki Ikawa[4], Akihide Kasai[1], Amane Fujiwara[5], Brent Else[6]

[1]*Faculty/Graduate School of Fisheries Sciences, Hokkaido University, Japan*
[2]*Field Science Center for Northern Biosphere, Hokkaido University, Japan*
[3]*Arctic Research Center, Hokkaido University, Japan*
[4]*Hokkaido Agricultural Research Center, NARO, Japan*
[5]*Institute of Arctic Climate and Environment Research, JAMSTEC, Japan*
[6]*Department of Geography, Arctic Institute of North America, University of Calgary, Canada*

The Arctic Ocean is an important carbon dioxide (CO_2) sink in the global carbon budget, absorbing 66−199 Tg C per year from the atmosphere (Bates & Mathis, 2009). CO_2 exchange with the atmosphere occurs not only in the open water but also in the sea ice area (Geilfus et al., 2015; Yoshimura et al., under revision). The CO_2 flux between the atmosphere and sea ice is controlled by the brine volume fraction (BVF) and the difference in the partial pressure of CO_2 (pCO_2) between the atmosphere and the brine. The pCO_2 of brine varies in a complex manner due to various factors such as temperature and carbonate system components, so detailed studies on the carbonate chemistry of brine are needed to determine the CO_2 balance in sea ice regions. Therefore, to clarify carbonate chemistry variations in the brine, we conducted observations in Cambridge Bay (CB), Canada from middle of May to beginning of June 2023 and in Utqiavik (UTQ) (Barrow), USA in middle of May 2024. Brine in sea ice was collected by the sack-hole method, and temperature, salinity, dissolved inorganic carbon (DIC), and total alkalinity (TA) of brine were measured.

During the observation period, brine temperatures increased from −3.7°C to −2.2°C, while brine salinity decreased from 61.5 to 37.7 in CB. For UTQ, brine temperatures increased from −1.3°C to −1.1°C and brine salinity decreased from 24.1 to 19.0. Brine salinity likely decreased as sea ice melted and flowed into the brine channel as sea ice temperature increased. Concurrent with the decrease in brine salinity, DIC, and TA concentrations also decreased. The pCO_2 calculated from brine temperature, salinity, DIC and TA using CO2SYS ver. 02.05 (Orr et al., 2018) in CB for early observation period (485 µatm) was higher than in the atmosphere (418 ± 3 µatm). However, over time, brine pCO_2 decreased to 335 µatm and eventually became lower relative to the atmosphere. Following Cox and Weeks (1983), BVF was calculated from the 20 cm surface layer of sea ice, resulting in a BVF of 6.8−10.8%. When the BVF is above 5−7.5%, sea ice is permeable for gas within sea ice and gas exchange could be occurred between the atmosphere and sea ice (Golden et al., 1998; Pringle et al., 2009; Zhou et al., 2013). In light of the above, sea ice during the observation period in CB was considered to have changed from a source to a sink of CO_2 to the atmosphere.

To investigate the variations in pCO_2 when meltwater (sea ice/snow) and brine were mixed, pCO_2 (pCO_2_cal) was calculated using the brine and meltwater results (temperature, salinity, DIC, and TA) from the first day of CB observations as end members (Figure 1). When brine (high salinity, high pCO_2) and meltwater (low salinity, low pCO_2) were mixed, pCO_2 decreased with decreasing salinity by the dilution effect of meltwater. This decrase was coincident with the variations in pCO_2 in CB and UTQ, suggesting the significance of the dillution effect for the variation of the brine pCO_2.

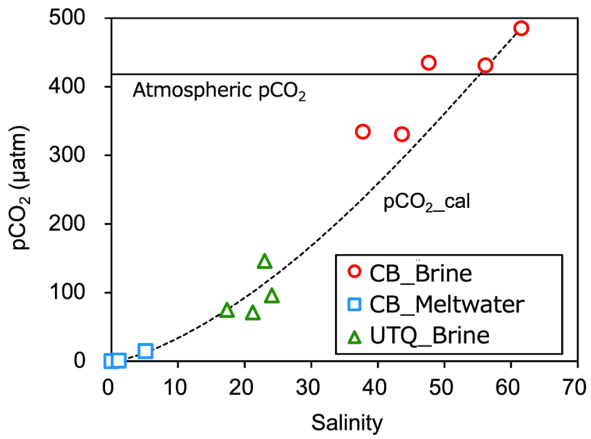

Figure 1. Relatinship between pCO_2 and salinity for brine and sea ice meltwater in Cambridge Bay (CB) and Utqiavik (UTQ). Dotted and solid lines indcate the pCO_2 when brine and meltwater were mixed (pCO_2_cal) and atmospheric pCO_2, respectively.

Short-term sea ice forecast for the whole Arctic Ocean using ice-ocean coupling model

Yoshihiro Niwa[1], Motomu Oyama[1,2], Takeshi Sugimura[1], and Hironori Yabuki[1,2]
[1] *International Polar and Earth Environmental Research Center, National Institute of Polar Research (NIPR)*
[2]*Arctic Sea Ice Information Center, NIPR*

・Introduction

With the recent rapid decline in summer sea ice in the Arctic Ocean and the opening of Arctic sea routes, the need for accurate forecasts of sea ice distribution is increasing. Sea ice forecasts are categorized by time range into long-term (a few decades), mid-term (a few months), and short-term (a few days) forecasts. In particular, short-term sea ice forecasts based on numerical simulations are crucial for ship navigation, as they help select the safest and shortest route through ice-covered areas of the Arctic Ocean.

At the NIPR's Arctic Sea Ice Information Center, we provide short-term sea ice forecasts each summer to support the Arctic research cruise of RV Mirai, operated by JAMSTEC (https://ads.nipr.ac.jp/venus.mirai/#/mirai). In addition, we offer a web service that provides optimum shipping route information across the whole Arctic Ocean (Sugimura et al., 2021) (https://ads.nipr.ac.jp/routeSearch/#/top). However, these two services are currently not interconnected because the current sea ice forecast area is limited to a part of the Arctic Ocean (white line square in Fig.1(a)), where the Mirai cruise is conducted. In the present study, as a first step toward developing a next version sea ice forecast system that integrates the optimum sea route service, we conduct short-term sea ice forecasts covering the whole Arctic Ocean and examine their performance.

・Model description

The numerical model used in this study is Ice-POM, an ice-ocean coupling model developed by De Silva et al. (2015). The model domain (Fig.1(a)) covers the whole Arctic Ocean, including the northeast and northwest shipping routes passing through the Russian coast and the Canadian archipelago, respectively. The model grid spacing is approximately 5 km horizontally with 33 vertical levels (Note that the current grid spacing is preliminary and will be refined in the future). The forecast model is initialized based on the analysis products from RIOPS (Regional Ice Ocean Prediction System) of Canada. Then, a 10-days forecast run is conducted using atmospheric forcing data from the forecast products of ECMWF.

・Results

As a test case, we conduct the 10-days forecast runs daily for one month during the summer from August 5 to September 5, 2022. Fig.1(a) shows the distribution of sea ice concentration obtained from the RIOPS analysis product on August 26, the day when the melting of sea ice off the coast of the East Siberian Sea led to the opening of the Arctic sea route. Figs.1(b) and (c) show the same distributions as Fig.1(a) but the forecast results predicted 5 days and 10 days earlier, respectively. Comparing the forecast results (Figs.1(b),(c)) with the analysis product (Fig.1(a)), we can see that while the overall sea ice distribution is well predicted, both the 5-days and 10-days forecasts fail to predict the opening of the Arctic sea route in the East Siberian Sea. In addition, the 10-days forecast (Fig.1(c)) fails to predict the opening of the sea route in the Laptev Sea and does not accurately predict the retreat of marginal sea ice in the Beaufort Sea.

Fig. 2 compares the time series of sea ice extent (the total area with sea ice concentration greater than 15%). It shows that the 10-days forecast (red line) overpredicts sea ice extent (black line) throughout the period, while the 5-days forecast (blue line) performs relatively well. However, the 5-days forecast fails to predict the rapid decrease in sea ice extent from 21 to 26, August toward the opening of the Arctic sea route. These results suggest that to accurately predict Arctic sea routes for future ship navigation, we need to further improve forecast performance by improving grid resolution, sea ice model, sub-grid scale parameterizations, etc.

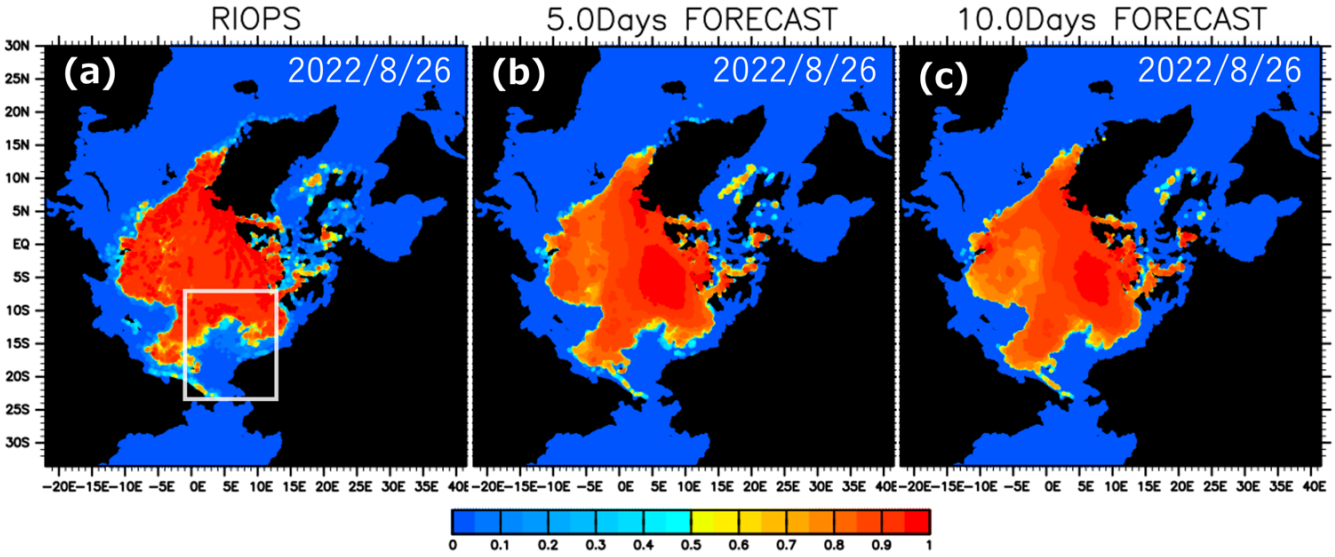

Figure 1. Sea ice concentration distribuition for the whole Arctic Ocean on August 26, 2022 obtained from (a)RIOPS analysis product, (b) 5-days forecast, and (c) 10-days forecast. White line square in (a) indicates the area of current short-term sea-ice forecasts for the RV Mirai Arctic cruise.

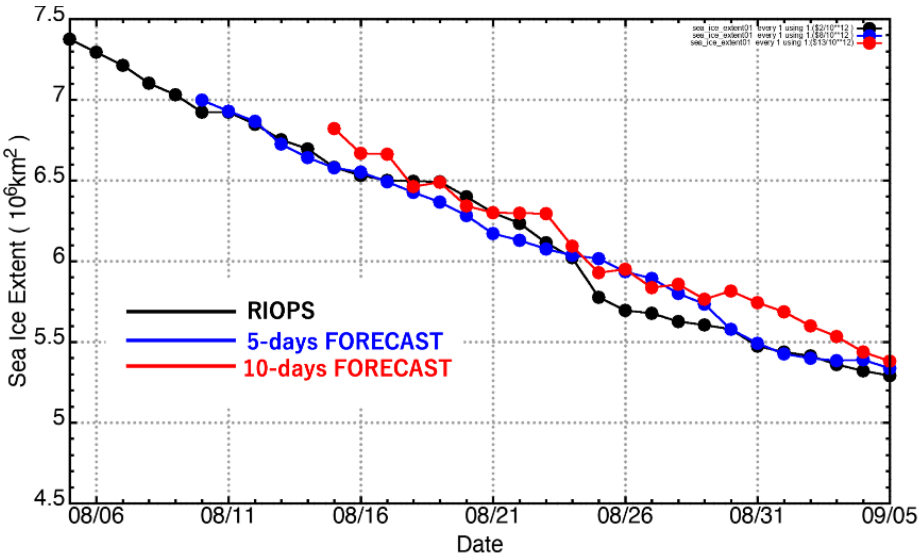

Figure 2. Time series of sea ice extent over the whole Arctic Ocean from August 5 to September 5, 2022. The data from RIOPS analysis product (black line), 5-days forecast (blue line), and 10-days forecast (red line) are shown.

Extraction of High-Resolution SAR Image Segments as Sea-Truth Data for Deformed Ice Location Analysis

Kentaro ONO[1] and Akihisa KONNO[2]
[1] *Kogakuin University Graduate School of Engineering, Tokyo, Japan*
[2]*Kogakuin University Faculty of Engineering, Tokyo, Japan*

Deformed ice refers to ice sheets that are pressed together by wind and currents, causing them to be pushed up or down under pressure. It is known that the roughness of sea ice surfaces and the thickness of the submerged ice are proportional (Worby et al, 2008). Since deformed ice with large surface roughness is also pushed downward into the water, it is considered to have significant thickness.

In this study, the sea ice thickness and drift velocity used as sea-truth data were measured by the ADCP (Acoustic Doppler Current Profiler) and ULS (Upward-Looking Sonar) deployed by the BGEP (Beaufort Gyre Exploration Project) in the Beaufort Sea. These instruments are moored in the Beaufort Sea and measure the data of the sea ice passing directly above them. This study used observation data from Site-D (74°N, 140°E), one of the multiple locations where the instruments are deployed. The ULS is a sonar installed on a buoy moored to the seabed and detects the sea surface upwards using ultrasound. The ice draft can be determined by calculating the difference between the distance from the depth where the sonar is moored to the sea surface and the distance from the sonar to the ice bottom. Sea ice moves due to wind and currents, allowing continuous measurement of the draft of sea ice flowing over the ULS. Although the ULS is fixed and limited to a specific location, the observed data has very high temporal resolution, measuring every second. The ADCP uses its bottom-tracking function to measure the movement speed of the ice bottom and records the velocity of the sea ice above the fixed device. The ADCP takes measurements every 30 minutes. In this study, linear interpolation was applied to the ADCP's measurement data to synchronize it to a per-second time scale, which was then used to track the ice sheet motion.

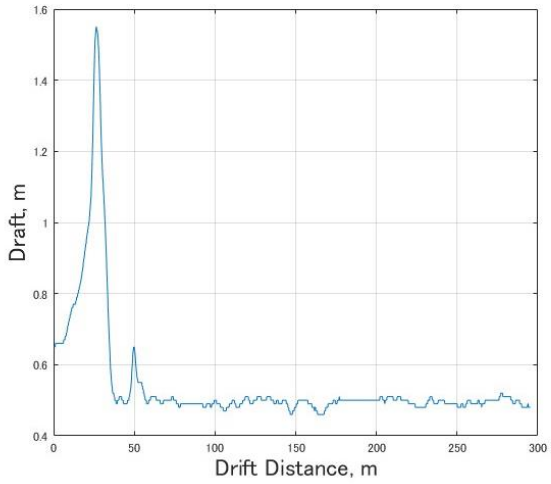

Figure 1. Drift Distance and Draft

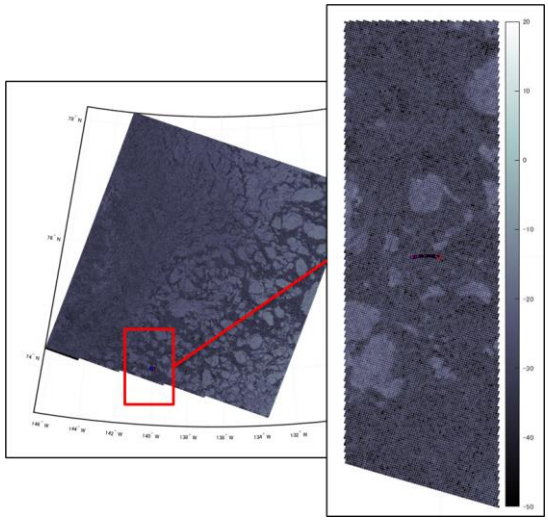

Figure 2. SAR image of the Beaufort Sea and sea ice movement trajectory

we focused on the draft data measured by Site-D's ULS during the 30 minutes before and after the SAR observation time. The trajectory was obtained by connecting these travel points, and the cumulative sum of the vectors of each movement distance was used to determine the ice's position at the end of the calculation period. The draft of the ice located above Site-D during the calculation period and the distance traveled by the ice from the time it passed directly over Site-D to the end of the calculation period are shown in Figure 1. Figure 2 shows the results of converting the movement trajectory to corresponding geographic coordinates and plotting them on the SAR image.

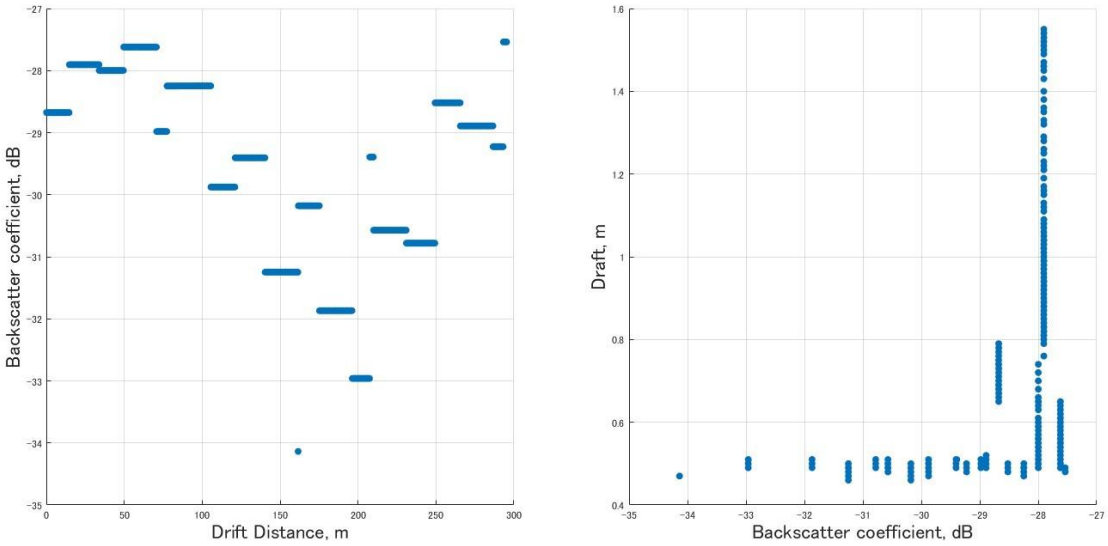

Figure 3. Relationship between Drift Distance, Backscatter Coefficient, and Draft

Figure 3 shows the backscatter coefficient and draft along the movement trajectory. The backscatter coefficient of the pixel closest to the trajectory is extracted.

In addition to plotting movement trajectories using other Sentinel-1 SAR data or different calculation periods, SAR images cropped by these methods will be incorporated into a learning model. During the implementation of the model, adjustments will be made to determine whether calibration of the Sentinel-1 data is necessary, as well as to optimize the image cropping size.

References

Worby, Anthony P., et al. "Thickness distribution of Antarctic sea ice." Journal of Geophysical Research: Oceans 113.C5 (2008).

OMp8

Coastal ocean dynamics around Greenland: Ice-sheet meltwater impacts and a circum-Greenland perspective

Kazuya Kusahara[1], Yoshiki Komuro[1], Fuyuki Saito[1] and Hiroaki Tatebe[1]
[1]*Japan Agency for Marine-Earth Science and Technology (JAMSTEC)*

Much attention has been paid to the recent increase in freshwater supply from the Greenland Ice Sheet (GrIS). This study conducts numerical experiments of a global sea ice-ocean model with a 0.25° resolution to investigate the pathways of GrIS meltwater and its impacts on the surrounding sea-ice and ocean fields. First, we investigate the pathways of the regional meltwaters in 30-year-long passive tracer experiments. The model demonstrates that the GrIS meltwaters are concentrated in coastal currents circulating around Greenland and effectively spread over Baffin Bay. Furthermore, as confirmed in previous literature, it is found that the meltwater is efficiently transported southward by the Labrador Current and then by the North Atlantic Current to the eastern North Atlantic and eventually to the Barents Sea. Next, a comparison of numerical experiments with and without the GrIS meltwater flux revealed that the GrIS meltwater contributes to regional ocean stratification and the delays sea-ice melting in the surrounding oceans. The GrIS meltwater increases the velocity of coastal surface currents by up to 10%. To further understand the ocean circulation around Greenland, we introduce for the first time a regional overturning circulation function based on semi-closed regions defined by the distance from the GrIS coastline. Our novel regional overturning circulation function illustrates that there is a wind-driven downwelling of approximately 1.5 Sv around Greenland, and the seasonal and interannual variability is well explained by on-shelf Ekman transport in the surface layer and off-shelf return flow in the lower layer, Arrested Topographic Wave dynamics (Fig. 1).

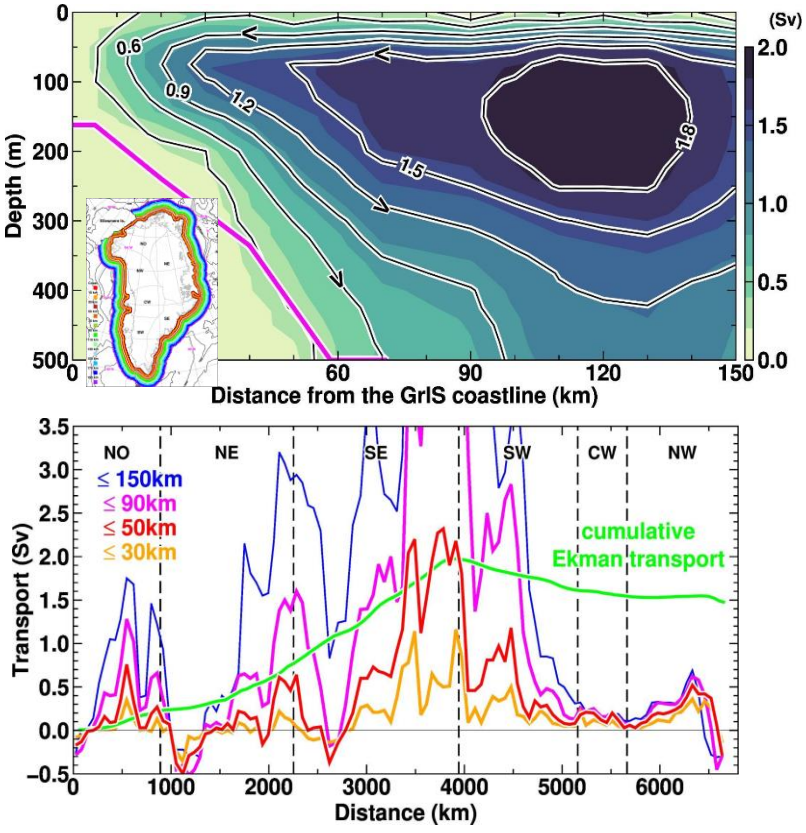

Figure 1: (Upper panel) Vertical overturning circulations in the GrIS coastal region. Contours and colors show the overturning stream function (Sv) in the distance–depth space. The stream function is calculated by lateral integration of volume transport along consistent distances from the GrIS coastline (see the small map with the color showing distance from the coastline). The horizontal axis is the distance from the GrIS coastline, and the vertical axis is the depth. The results show the annual-mean climatology averaged over the reference period (1981–2010). The magenta line shows the mean depth profile around Greenland.

(Lower panel) Alongshore ocean transport around Greenland. The horizontal axis represents the distance from the eastern coast of Ellesmere Island, moving clockwise with Greenland to the right (see the small map). The vertical axis shows the alongshore transport (Sv) in the model, calculated for the upper 200 meters. The orange, red, pink, and blue lines represent the transport integrated over distances of 30 km, 50 km, 90 km, and 150 km from the coast, respectively. The green line indicates the cumulative Ekman transport, calculated from wind stress.

OMp9

Nutrient dynamics in the Southern Ocean using the parameterizations and the data from mooring systems/shipboard observations

Sugita M[1], Mizobata K[3], Makabe R[4], Ohashi Y[4], Hirano D[4], Li BF[2], Watanabe YW[1,2]

[1] *Grad. Sch. Env.Sci., Hokkaido Univ., Sapporo, Hokkaido, Japan*
[2] *Fac. Env. Earth Sci., Hokkaido Univ., Sapporo, Hokkaido, Japan*
[3] *Dept. Ocean Sci., Tokyo Univ. Mar. Sci. Tech., Tokyo, Japan*
[4]*Natl. Inst. Polar Res., Tokyo, Japan*

The Southern Ocean (SO, south of 30°S) is considered to play an important role in the ocean biogeochemical cycling [e.g., *Sarmiento and Gruber*, 2006]. However, the interaction between biological activity and the environment in the SO is still unknown in detail due to the difficulty of observation due to severe weather and ocean conditions. To overcome this problem, we attempted to apply a hybrid parameterization based on multiple linear regression (MLR) and neural network (NN) for nutrients (phosphate, nitrate, silicate, dissolved inorganic carbon, pH) *(Pan et al.*, 2022, 2023, 2024) to the data set from several shipboard observations and the two mooring points in the SO (Sta. MM01 within the Poinsett eddy (64.0°S-114.5°E), Sta. TM01 off the Totten Ice Shelf in the East Antarctica (66.6°S-116.5°E). In the case of the mooring systems in the SO, we found the footprints of the downward export of biological productivity from the surface within the Poinsett eddy, and the glacier-derived freshening off the Totten Ice Shelf. On the day of the presentation, we will demonstrate and discuss some examples to elucidate the interaction between biological activity and the environment in the SO.

References

Sarmiento JL & Gruber N. Ocean Biogeochemical Dynamics. (Princeton University Press, 2006).

Pan XL, Li BF, Watanabe YW (2022): Intense ocean freshening from melting glacier around the Antarctica during early 21th century, Scientific Reports, 12, 383, doi: 10.1038/s41598-021-04231-6.

Pan XL, Lai, X, Makabe R, Hirano D, Watanabe YW (2023): Spatiotemporal high-resolution mapping of biological production in the Southern Ocean. Communications Earth & Environment, 4, 488 (2023), doi: https://doi.org/10.1038/s43247-023-01067-y.

Pan XL, Li BF, Hirano D, Makabe R, Shimada K, Watanabe YW (2024): Global distribution of biological decoupling between silicate and nitrate on marine productivity. submitted.

OMp10

Long-term variability of seawater stable oxygen isotope ratio in the Indian Ocean sector of the Southern Ocean

Mahiro Ohata[1], Shigeru Aoki[1] , Keishi Shimada[2] ,Kohei Mizobata[2] , Yujiro Kitade[2]
[1]*Institute of LowTemperature Science,*
[2] *Tokyo University of Marine Science and Technology,*

Introduction

Antarctic Bottom Water (AABW) is a high-density water mass that sinks along the Antarctic coast and serves as the starting point for the global deep-ocean circulation. In recent years, significant freshening and reduced density have been observed in the regions supplying AABW, and the formation of AABW has been on a declining trend since the 1990s. Furthermore, according to Shimada et al. (2020), in the East Antarctic Indian Ocean sector, the bottom water has become less dense and is sinking into the intermediate layers (γ = 28.02 to 28.19). The main cause of this decrease in density is thought to be the melting of the Antarctic ice sheet. However, the contributions of other freshwater sources, such as local precipitation and sea ice melt, are also considered, and it is not quantitatively clear which factor plays a major role. Oxygen isotopes are sensitive tracers of freshwater in seawater and are especially effective tools for detecting meltwater from the Antarctic ice sheet. Numerical simulations of freshwater discharge from the ice sheet indicate that oxygen isotope ratios reflect these effects earlier than salinity, especially in the Ross Sea (Kim and Timmermann, 2024). However, due to a lack of observational data, there has been little research on ocean water mass variations using stable oxygen isotope ratios in actual observations.

Objectives and Data

The objective of this study is to analyze the interannual variability of water mass properties, such as water temperature, salinity, and stable oxygen isotope ratio (δ^18O) in the East Antarctic Indian Ocean sector, and to identify the freshwater sources (ice sheet meltwater, sea ice meltwater, precipitation, etc.) contributing to these changes. Additionally, the study aims to evaluate the influence of warm Circumpolar Deep Water (CDW) on the East Antarctic Indian Ocean sector and its relationship with changes in bottom water. Continuous observational data along the 110°E line, along with salinity, water temperature, and stable oxygen isotope ratio (δ^18O) datasets obtained from WOCE and the Shioyakam Maru ship-based observations, are used. The salinity and water temperature data cover 12 years from 1995 to 2022, while the oxygen isotope ratio data cover 9 years from 2011 to 2019.

Results

Overall, a warming trend and a decrease in salinity were observed in the bottom water, which is consistent with previous research findings. The stable oxygen isotope ratio (δ^18O) in both the bottom and intermediate layers (γ = 28.02 ~ 28.19) showed an overall decreasing trend from 2011 to 2019. These results suggest that the increased melting of the Antarctic ice sheet may be influencing the formation of AABW. However, an increasing trend in δ^18O was also observed in some regions, particularly between 2013 and 2017, after which it decreased again. This indicates that multiple freshwater sources contributing to bottom water formation are not uniform in their variability. This variability might also be due to the increased sea ice production in the Ross Sea in 2012, which altered the properties of the bottom water, suggesting that the selection of the analysis period could influence the results. Moreover, the current measurement accuracy of δ^18O is stated to be 0.02‰ (standard deviation), but attention must be paid to the long-term stability of this accuracy. As even slight variations in δ^18O can be significant indicators, ensuring measurement consistency and accuracy is extremely important for future research.

References

Shimada, K., Y. Kitade, S. Aoki, K. Mizobata, L. Cheng, K.T. Takahashi, R. Makabe, J. Kanda, and T. Odate, Shoaling of abyssal ventilation in the Eastern Indian Sector of the Southern Ocean, Communications Earth & Environment, 3:120, 2022.

Kim, H. and A. Timmermann, Seawater oxygen isotopes as a tool for monitoring future meltwater from the Antarctic ice-sheet, Communications Earth & Environment, 5(343), 2024.

OMp11

Processes of high sea ice production and dense water formation in the Cape Darnley polynya that creates the precursor of Antarctic Bottom Water

Masashi Machida[1], Kay I. Ohshima[2,3], Alexander D. Fraser[4] ,Kazuki Nakata[5], Mizuki Kuga[2],Daisuke Simizu[6] , Takeshi Tamura[6], Yasushi Fukamachi[3]

[1]*Graduate School of Environmental Science, Hokkaido University, Sapporo, Hokkaido, Japan*

[2] *Institute of Low Temperature Science, Hokkaido University, Sapporo, Hokkaido, Japan*

[3]*Arctic Research Center, Hokkaido University, Sapporo, Japan*

[4]*Australian Antarctic Program Partnership, Institute for Marine and Antarctic Studies, University of Tasmania, Tasmania, Australia*

[5] *Earth Observation Research Center, Japan Aerospace Exploration Agency, Tsukuba, Japan*

[6] *National Institute of Polar Research, Tachikawa, Japan*

In the Antarctic coastal polynya, brine rejection during sea ice formation creates cold, saline, very dense water known as Dense Shelf Water (DSW). A part of this water sinks with being transformed into Antarctic Bottom Water (AABW) and occupies the abyssal layer of the global ocean, driving global overturning circulation. High sea ice production in the polynyas potentially contributes to high biological production in the Southern Ocean by incorporating micronutrients such as iron during the ice formation and releasing them during the ice melting.

Coastal polynyas have very efficient ice production system due to the maintenance of an open water or thin ice area by prevailing offshore-ward wind and generation of underwater frazil ice with a convection of supercooled water (Ohshima et al. 2022). The Cape Darnley polynya (CDP) has the second highest ice production around the Antarctica after the Ross Ice Shelf polynya (Tamura et al. 2008). The high ice production makes this polynya a source region of AABW (Ohshima et al. 2013). However, the details of ice production system leading to DSW formation and its interannual variation have not been well understood.

In this study, we examine the detailed processes of sea ice production and DSW formation with their yearly difference in the CDP using a comprehensive dataset: the mooring data taken for two years under the Japanese Antarctic Research Expedition, and the satellite sea ice products. The dataset includes the velocity and backscatter strength (SV) data throughout the water column derived from acoustic Doppler current profilers (ADCPs), temperature-salinity data, obtained by the moorings at three sites from February 2013 to February 2015 (partly 2014). As satellite sea ice products, we used the sea ice production and frazil ice detection data derived from the microwave radiometer AMSR by Nakata et al. (2021), and the landfast sea ice data derived from MODIS data by Fraser et al. (2020).

Figure 1 shows the time series of annual sea ice production for the Cape Darnley polynya. The sea ice production in the CDP in 2013 and 2014 was significantly different. The total annual sea ice production was the second lowest in 2013 while the third highest in 2014 since 2003. According to the time series of sea ice production in 2013 (Fig.2a), sea ice production was high in the first half of the year while suppressed in the second half. Whereas in 2014 (Fig.2b), sea ice production was low in the first half of the year while high in the second half.

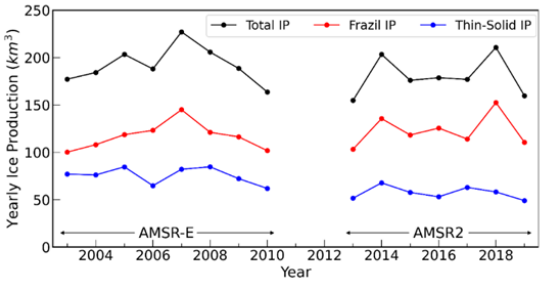

Figure. 1 Time series of annual sea ice production for the Cape Darnley polynya.
Annual ice production in active-frazil area (red), thin solid-ice area (blue), and their total (black) are shown for the periods of AMSR-E (2003–2010) and AMSR2 (2013–2019). After Ohshima et al. (2022).

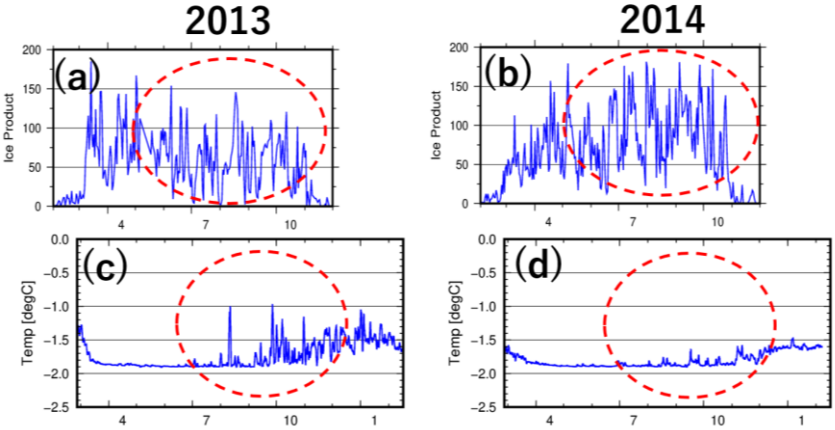

Figure. 2 Time series of daily sea ice production (km^3/day) in the CDP in (a) 2013 and (b) 2014, Water temperature at the depth of 142 m at C1 in the CDP during (c) 2013 and (d) 2014.

This contrasting difference in sea ice production between the two years can be explained by the differences in the warm water inflow and the distribution of landfast ice. The time series of water temperature in 2013 shows frequent occurrence of sporadic temperature increase after August (Fig. 2c), which can be attributed to the inflow of warm water originating from the modified Circumpolar Deep Water (mCDW). While such sporadic temperature increase was seldom in 2014 (Fig. 2d). The ADCP backscattering data indicated that the inflow of warm water in 2013 also suppressed frazil ice production, thereby reducing the efficient sea ice production of underwater frazil ice production. The analysis of satellite data also shows that the amount of frazil ice production in 2013 was much lower than that in 2014 (red lines in Fig.1). The blue shadings in Fig.3 indicate landfast sea ice around the CDP. It is found that a large part of the CDP was covered by landfast sea ice during June-August in 2013 (upper panel of Fig.3), while not in 2014 (lower panel of Fig.3). Large cover of landfast sea ice in 2013 significantly suppressed sea ice production in the CDP.

How are high sea ice production and its interannual variation related to the DSW formation? How does warm water of mCDW origin flow onto the continental shelf? These remaining questions will be further examined in the future, based on the current velocity and T-S data obtained by the moorings. The present combined study of mooring and satellite suggests that the presence or absence of the warm water inflow can be inferred from the AMSR frazil ice detection to some extent. Thus, the use of the AMSR frazil ice detection algorithm might provide information for the ocean condition in the CDP in other non-observation years or other coastal polynyas.

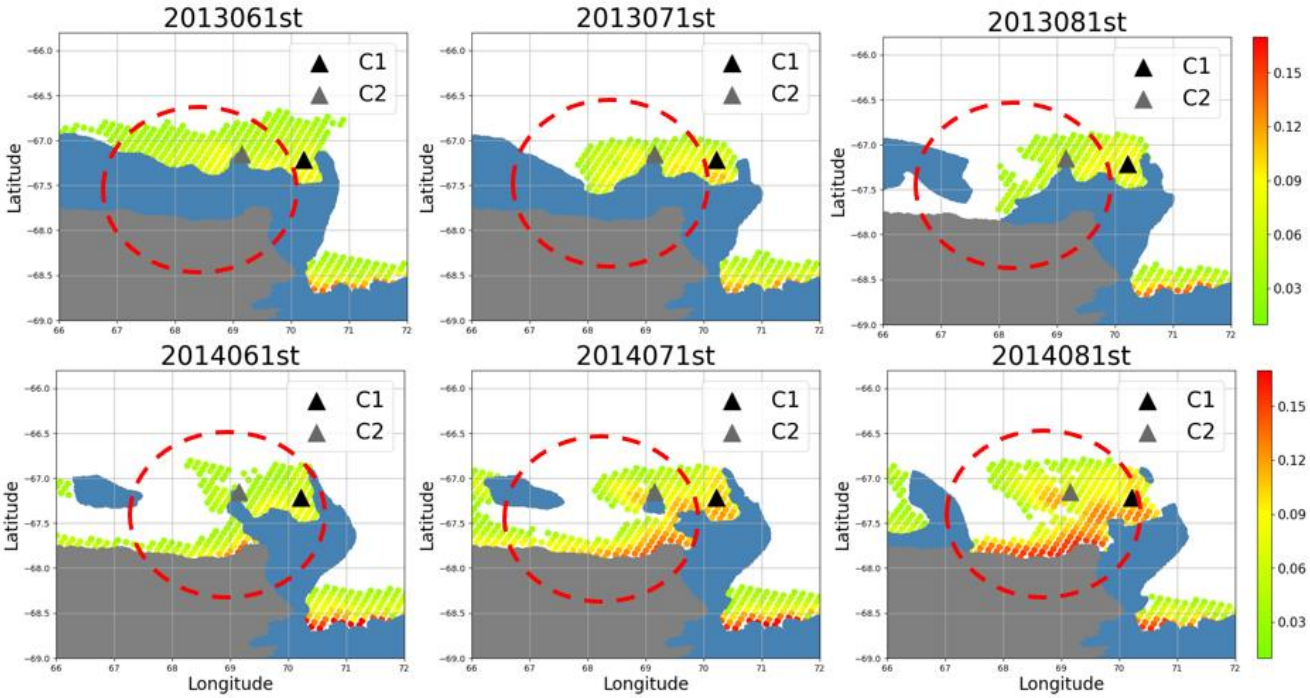

Figure. 3 Monthly mean sea ice production (color dots) and landfast sea ice distribution (blue shading) around the CDP during June-August in 2013 (upper panel) and 2014 (lower panel). The mooring locations are indicated by black triangle (C1) and grey triangle (C2).

References

Fraser, A. D., Massom, R. A., Ohshima, K. I., Willmes, S., Kappes, P. J., Cartwright, J., and Porter-Smith, R.: High-resolution mapping of circum-Antarctic landfast sea ice distribution, 2000–2018, Earth Syst. Sci. Data, 12, 2987–2999, 2020.

Nakata, K., Ohshima, K. I., & Nihashi, S., Mapping of active frazil for Antarctic coastal polynyas, with an estimation of sea-ice production. Geophysical Research Letters, 48, e2020GL091353, 2021.

Ohshima, K. I., Fukamachi, Y., Williams, G. D., Nihashi, S., Roquet, F., Kitade, Y., Tamura, T., Hirano, D., Herraiz-Borreguero, L., Field, I., Hindell, M., Aoki, S., & Wakatsuchi, M., Antarctic Bottom Water production by intense sea-ice formation in the Cape Darnley polynya, Nature Geoscience, 6(3), 2013.

Ohshima, K. I., Y. Fukamachi, M. Ito, K. Nakata, D. Simizu, K. Ono, D. Nomura, G. Hashida, T. Tamura, Dominant frazil ice production in the Cape Darnley polynya leading to Antarctic Bottom Water formation. Science Advances,8,eadc9174, 2022.

Tamura, T., K. I. Ohshima, and S. Nihashi, Mapping of sea ice production for Antarctic coastal polynyas, Geophysical Research Letters, 35 (7), 2008.

OMp12

The cause and formation mechanism of the Cosmonaut Polynya revealed by a mixed layer model

Masato Maeno and Kay I. Ohshima
Institute of Low Temperature Science, Hokkaido University, Sapporo, Japan

A polynya is an area of thin ice or open water that exists within sea-ice covered region. There are two types of polynyas: latent heat polynyas (mainly in coastal areas) that are generated when sea ice is blown offshore by wind, and sensible heat polynyas (mainly in the open ocean) that are generated by upwelling of warm water that suppresses sea ice formation and melts sea ice. Among the sensible heat polynyas, the Weddell Polynya that appeared in 1974-1976 is the largest and most prominent one, and it reappeared in 2016-2017 for the first time in 40 years (Campbell et al. 2019). For this polynya, it is suggested that the deep convection occurred with heat supplied from the intermediate/deep layers to prevent the ice formation. In turn, the deep convection has altered the intermediate/deep water properties, potentially affecting the thermohaline circulation.

The Cosmonaut Polynya is also considered as a large-scale sensible polynya, although the open water was not maintained throughout the year (Comiso and Gordon, 1996). According to 40-year SSM/I ice concentration data, although the occurrence area of the Cosmonaut Polynya is confined to the area of 41°~47°E and 64°~65.5°S, its occurrence period (season) and its duration depend on year. So far the cause and formation mechanism of this polynya have not been well understood. Further, it is also a question whether a deep convection occurred or not at the presence of the Cosmonaut Polynya. The purpose of this study is to elucidate the cause and formation mechanism of the Cosmonaut Polynya using a mixed layer model of Kraus and Turner (1967), which assumes that the mixed layer deepens due to entrainment caused by wind turbulence energy and cooling potential energy.

According to the climatological dataset of water temperature and salinity created by Mensah and Ohshima (2023), the area where the Cosmonaut Polynya has frequency occurred is characterized by thin mixed layer. To run the mixed layer model, we used the climatology of temperature and salinity in March, when cooling starts, as the initial profile, and the climatology of wind speed and heat flux (loss) from the ERA5 data as the forcings. Calculations were performed until the temperature in the mixed layer reached the freezing point. The model results show that the freezing is significantly delayed in the area where the polynya has frequently occurred, compared to other regions.

Next, we used individual temperature and salinity data observed in March as the initial profiles, and the wind speed and heat loss in the observed year. The model results suggest a tendency that the freezing is delayed around the areas where the polynya has frequently occurred, compared to the surrounding regions. Interestingly, some cases (about 20%) show that a deep convection occurs with heat supplied from the intermediate/deep layer and the freezing is prevented throughout the year. A similar result was also obtained in the area east of the polynya off Cape Ann, where the wind is particularly strong. This suggests that the westward background current advects water mass capable of forming a polynya westward, leading to its formation. These analyses of the mixed layer model show that in areas where the Cosmonaut Polynya occurs, the mixed layer is thin, allowing heat to be easily supplied from the underlying warm and saline water, which delays the freezing. A possibility of a deep convection is also suggested. This study concludes that the Cosmonaut Polynya is a sensible heat polynya and its formation is sensitive to the variations in wind and oceanographic conditions from year to year.

Reference

Campbell, E.C., E.A. Wilson, G.W.K. Moore, S.C. Riser, C.E. Brayton, M.R. Mazloff, L.D.Talley, Antarctic offshore polynyas linked to Southern Hemisphere climate anomalies. Nature, 570, 319–325, doi:10.1038/s41586-019-1294-0, 2019.

Comiso, J. C., and A. L. Gordon, Cosmonaut polynya in the Southern Ocean: Structure and variability, Journal of Geophysical Research, 101(C8), 18297-18313,1996.

Kraus, E., and J. Turner, A one-dimensional model of the seasonal thermocline II. The general theory and its consequences, Tellus, 19(1), 98–106, 1967.

Mensah V. and K. I. Ohshima, A Mapping Methodology Adapted to all Polar and Subpolar Oceans with a Stretching/Shrinking Constraint, JOURNAL OF ATMOSPHERIC AND OCEANIC TECHNOLOGY, 40, 1241-1261, 2023.

Structure of the Weddell Gyre's eastern boundary derived from surface floats

T. Imo[1], K. Mizobata[2], D. Hirano[3], K. Ono[4], S. Aoki[4]
[1]*Graduate School of Environmental Science, Hokkaido University*
[2]*Department of Ocean Sciences, Tokyo University of Marine Science and Technology*
[3]*National Institute of Polar Research*
[4]*Institute of Low Temperature Science, Hokkaido University*

Introduction

The Weddel Gyre is a clockwise circulation sandwiched between a coastal current flowing along the Antarctic continental shelf margin and the offshore Antarctic Circumpolar Current. At its western end, it forms the Weddel Sea Deep Water, a type of Antarctic Bottom Water. The formed Antarctic Bottom Water is responsible for the global-scale overturning circulation. Therefore, the Weddel Gyre has a significant impact on the global climate. While the depiction of the western structure of Weddel Gyre is known to some extent, partly because it is restricted to the Antarctic Peninsula, the eastern structure, where water flows in from the northern Antarctic Circumpolar Current, has not been established. Reeve et al. (2019) have used previous Argo float data to create a stream function for the entire Weddel Gyre and derived flow fields. However, the number of Argo float data for the eastern boundary and continental coastal areas was not sufficient, and the uncertainty in the flow fields shown is large. In addition, the eastern boundary of Weddel Gyre is located beyond 60°E in flows derived from sea surface dynamic height based on satellite observations in the past (Park and Gamberoni., 1995), and stream function derived from numerical models show that the position of the eastern boundary of the Weddel Gyre varies significantly from year to year (Ryan et al. 2015). Therefore, the purpose of this study is to clarify the eastern structure of Weddel Gyre by using accumulated surface float observation data and the latest satellite observations and numerical experiments.

Data

The author participated in the 65th Japanese Antarctic Research Expedition (JARE65) from November 2023 to March 2024. On that occasion, five surface floats were deployed. Including previous surface floats, a total of 17 float data will be used. The information on the float data is shown in the Table 1. The latest sea-surface height obtained from the satellite altimeter (Mizobata et al., 2020), and ERA-5 wind data are also used in addition.

Table 1. Information on previous surface floats.

S/N	JARE	Start Day	Start Point	End Day	End Point	Drogue
22001	65	2023/12/12	63.125S, 49.592E			○
22002	65	2023/12/13	63.449S, 46.003E	2024/1/27	64.369S, 44.077E	○
22003	65	2023/12/13	64.149S, 42.017E	2023/12/26	64.400S, 41.536E	○
22022	65	2024/2/19	66.229S, 46.600E	2024/6/20	64.883S, 23.733E	×
22023	65	2024/2/22	66.000S, 49.489E	2024/3/25	68.038S, 35.300E	×
6070	64	2022/12/14	65.015S, 45.000E	2023/2/27	66.502S, 42.185E	○
7100	64	2023/2/19	65.275S, 47.010E	2023/5/22	69.426S, 22.321E	○
5080	63	2021/12/10	68.455S, 38.225E	2022/1/20	68.391S, 33.143E	○
2090	63	2022/2/12	66.492S, 37.495E	2022/3/30	66.487S, 34.338E	○
9690	63	2022/2/12	66.366S, 40.367E	2022/8/30	64.089S, 1.282E	○
88219	50	2009/1/14	61.999S, 38.015E	2009/6/8	61.637S, 43.967E	×
88220	50	2009/1/15	64.011S, 37.951E	2009/6/8	63.976S, 43.683E	×
88221	50	2009/1/16	66.024S, 37.880E	2009/6/8	68.503S, 23.639E	×
78257	49	2007/12/20	68.381S, 37.578E	2008/2/12	68.529S, 37.218E	×
78258	49	2007/12/20	63.319S, 45.123E	2008/6/21	67.913S, 25.206E	×
78259	49	2007/12/20	67.201S, 36.254E	2008/7/1	65.643S, 12.790E	×
78256	49	2007/12/31	66.676S, 39.083E	2008/5/11	72.018S, 19.238W	×

Method

The time series data of float positions show the trajectory of each float and provide an overview of the flow field at the eastern end of Weddel Gyre. The flow velocity of each float is calculated and its variation is compared with the ERA-5 10-m wind variation to investigate the effect of wind. After evaluating the effect of wind on the float flow velocities, the accuracy of the

satellite-derived geostrophic velocity from sea level altitude using the altimeters of CryoSat-2/SIRAL and other instruments and the GOCO05c geoid model were evaluated by comparing the float drift speed.

Result

The trajectories of the five surface floats at JARE 65 are shown in Figure 1. The red and green trajectories are split into east and west, suggesting that the eastern boundary of Weddel Gyre is around 50°E. In addition, some of the float trajectories appear to follow the topography, indicating that it is a barotropic structure. These characteristics can also be seen from the historical surface floats, suggesting that the eastern boundary of Weddel Gyre is located around 50°E. An eddy-like structure is also observed just west of the boundary at about 45°E, which is thought to be a factor complicating the eastern boundary. The eastward coastal current velocity averaged about 20 cm/s but was faster in the fall than in the summer, although there could be differences depending on the location. A statistically significant correlation was also obtained between the variation of zonal winds and the zonal flow velocity of floats.

Overlaying the float trajectories with the flow field obtained from satellite altimeter showed that the altimeter-derived flow field was clearly reverse flow and inaccurate along the continental coast.

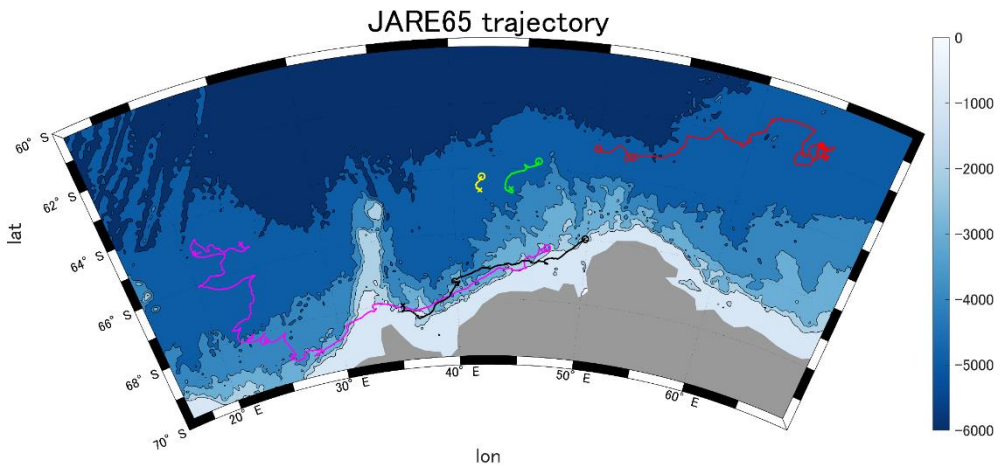

Figure 1. Trajectories of five surface floats deployed at JARE 65. The shade in the background is bathymetry.

Conclusion

We have attempted to determine the eastern structure of Weddel Gyre using previous surface float data. The float trajectory provides an overview of the eastern structure, and its eastern boundary is thought to be located around 50°E. An eddy-like structure is seen immediately to the west, which is considered to be a factor complicating the eastern structure of Weddel Gyre. The flow field from satellite altimeter has been characterized by a possible geoid defect in this vicinity (Kwok and Morison., 2016), indicating that float trajectories may improve the accuracy of the result. Further analysis, removing wind effects from the float data and combining it with numerical model and reanalysis data (OFES (OGCM for the Earth Simulator) and SOSE (Southern Ocean State Estimate)), etc., is expected to improve quantitative estimates of the eastern structure of Weddel Gyre and improve estimates of the amount of ice shelf melting due to heat through the Weddel Gyre and Antarctic bottom water formation.

References

Mizobata. K., Shimada. K., Aoki. S., Kitade. Y., 2020. The Cyclonic Eddy Train in the Indian Ocean Sector of the Southern Ocean as Revealed by Satellite Rader Altimeters and In Situ Measurements. JGR Oceans. 125, 6.

Park, Y. H., & Gamberoni, L. 1995. Large-scale circulation and its variability in the south Indian Ocean from TOPEX/POSEIDON altimetry. Journal of Geophysical Research, 100(C12), 24911.

Reeve, K. A., Boebel, O., Strass, V., Kanzow, T., and Gerdes, R. 2019. Horizontal Circulation and volume transports in the Weddell Gyre derived from Argo float data, Prog. Oceanogr., 175, 263–283.

Ryan, S., Schroder, M., Huhn, O., Timmermann, R., 2016. On the warm inflow at the eastern boundary of the Weddell Gyre. Deep-Sea Res. Part I: Oceanogr. Res. Papers 107, 70-81.

Kwok, R., J. Morison, 2006, Sea surface height and dynamic topography of the ice-covered oceans from CroSat-2:2011-2014. J. Geophys. Res. Oceans, 121, 674-692.

OMp14

Japanese observation programs of atmospheric greenhouse gases at Syowa Station, Antarctica and Ny-Ålesund, Svalbard

Daisuke Goto[1], Shinji Morimoto[2], Shigeyuki Ishidoya[3], Shohei Murayama[3], Sakae Toyoda[4] and Satoshi Sugawara[5]
[1]*National Institute of Polar Research*
[2]*Graduate School of Science, Tohoku University*
[3]*National Institute of Advanced Industrial Science and Technology*
[4]*Tokyo Institute of Technology*
[5]*Miyagi University of Education*

To elucidate the temporal variations in atmospheric greenhouse gases and other related species in polar regions, and to obtain information about their sources and sinks, we have maintained systematic observation programs at Syowa Station (69.00°S, 39.58°E), Antarctica, and Ny-Ålesund (78.92°N, 11.93°E), Svalbard, since 1984 and 1991, respectively. At Syowa Station, continuous measurements of atmospheric CO_2 were initiated in 1984 (e.g., Morimoto et al., 2003), and we later expanded these in-situ continuous measurements to include CH_4, CO, O_2, and N_2O as part of the Japanese Antarctic Research Expedition (JARE). In addition to the in-situ measurements, systematic air sampling with subsequent laboratory analysis has been conducted for SF_6, Ar (Ishidoya et al., 2021), and isotopic ratios of CO_2, CH_4, and N_2O. We have also collaborated with the air sampling program of the National Oceanic and Atmospheric Administration (NOAA) at the station since 1986. In the Arctic, weekly air sampling was initiated at Ny-Ålesund in 1991 to measure CO_2, CH_4, and the isotope ratios of CO_2. Since then, the measurements have expanded to include atmospheric CO, N_2O, SF_6, O_2 (e.g. Ishidoya et al., 2012), and the isotopic ratios of CH_4 (Morimoto et al., 2017). In-situ continuous measurements of atmospheric O_2 (Goto et al., 2017), CO_2, and CH_4 have also been maintained since 2012–2013, under the framework of Japanese Arctic Research Programs such as GRENE (2011–2015), ArCS (2015–2020), and ArCS II (2020–2025). Most of these datasets are available through the Science database (https://scidbase.nipr.ac.jp/?ml_lang=en) and the Arctic and Antarctic Data Archive System (ADS, https://ads.nipr.ac.jp/), both operated by the National Institute of Polar Research. In this presentation, we report our observational activities at Syowa Station and Ny-Ålesund and introduce plans in the future.

References

Goto, D., S. Morimoto, S. Aoki, P. K. Patra, T. Nakazawa, Seasonal and short-term variations in atmospheric potential oxygen at Ny-Ålesund, Svalbard, Tellus B: Chemical and Physical Meteorology, 69:1, 1311767, 2017.

Ishidoya, S., S. Morimoto, S. Aoki, S. Taguchi, D. Goto, S. Murayama, T. Nakazawa, S. Taguchi, P. K. Patra, Oceanic and terrestrial biospheric CO_2 uptake estimated from atmospheric potential oxygen observed at Ny-Ålesund, Svalbard, and Syowa, Antarctica, Tellus B: Chemical and Physical Meteorology, 64(18924), 2012.

Ishidoya, S., S. Sugawara, Y. Tohjima, D. Goto, K. Ishijima, Y. Niwa, N. Aoki, S. Murayama, Secular change in atmospheric Ar/N_2 and its implications for ocean heat uptake and Brewer-Dobson circulation, Atmospheric Chemistry and Physics 21(2) 1357-1373, 2021.

Morimoto, S, T. Nakazawa, S. Aoki, G. Hashida and T. Yamanouchi, Concentration variations of atmospheric CO_2 observed at Syowa Station, Antarctica from 1984 to 2000, Tellus, **55**(B), 170–177, 2003.

Morimoto, S., R. Fujita, S. Aoki, D. Goto, T. Nakazawa, Long-term variations of the mole fraction and carbon isotope ratio of atmospheric methane observed at Ny-Ålesund, Svalbard from 1996 to 2013, Tellus B: Chemical and Physical Meteorology, 69:1, 1380497, DOI: 10.1080/16000889.2017.1380497, 2017.

OMp15

Impact of anthropogenic aerosols on Arctic amplification in a long-term future climate

Jun Ono[1], Manabu Abe[2], Hiroaki Tatebe[2] and Yoshiki Komuro[2]
[1]*National Institute of Polar Research*
[2]*Japan Agency for Marine-Earth Science and Technology*

The Arctic has warmed approximately four times as fast as the globe (Rarpechko et al., 2022), called Arctic warming amplification (AA). So far, various processes (ice-albedo feedback, lapse rate and cloud feedbacks, and meridional heat transport) have been proposed to explain AA in previous studies (e.g., Goosse et al., 2018). However, the relative contributions are still under debate. Moreover, no study examined the dependence of future AA on greenhouse gas emission scenarios by the end of this century. In the previous study (Ono et al., 2022), we revealed, using a large ensemble of historical and scenario simulations by a single climate model MIROC6, that AA is intensified in a low-emission scenario (SSP1-2.6) compared with a high-emission scenario (SSP5-8.5) after the middle of 21st century. However, the difference in AA between the two scenarios may not be caused by the difference in CO2 forcing alone but affected by changes in other forcing agents such as aerosols, methane, and CFCs/HFCs (Previdi et al., 2021). For instance, emissions trajectories (IPCC, 2021) show that CO2 forcing reduces under SSP1-2.6 since the early twenty-first century but continues to increase until the late twenty-first century under SSP5-8.5. On the other hand, the anthropogenic aerosol emissions decrease in both scenarios, likely acting to warm the globe. Although the CO2 forcing is dominant for global warming in all SSP scenarios (Figure SPM.4 in IPCC (2021)), an assessment of the degree to which other radiative forcings' impact on AA has remained for future works. To assess the impact of anthropogenic aerosols on the AA, we conducted two climate simulations with 10-member ensembles for SSP1-2.6 and SSP5-8.5. In this study, emissions of anthropogenic sulfur dioxide, a key precursor to anthropogenic aerosols, were fixed at 2015 levels for both scenarios. Even with fixed aerosol emissions, AA could be still enhanced in a low-emission scenario and energy budget analysis suggests that ice-albedo feedback is the primary factor, which aligns with the findings of Ono et al. (2022). Further details will be discussed in the poster presentation.

Acknowledgement
The present study was supported by the Japan Ministry of Education, Culture, Sports, Science and Technology (MEXT) through the Arctic Challenge for Sustainability II (ArCS II: Grant Number JPMXD1420318865) Program and the advanced studies of climate change projection (SENTAN: Grant Number JPMXD0722680395) Program. Jun Ono was supported by the Japan Society for the Promotion of Science (JSPS) through a Grant-in-Aid for Scientific Research (KAKENHI-C Grant Number JP23K11416). The model simulations were performed using Earth Simulator at the Japan Agency for Marine-Earth Science and Technology (JAMSTEC), Japan.

References
Goosse, H., Kay, J. E., Armour, K. C. et al. (2018). Quantifying climate feedbacks in polar regions. Nature Communications, 9, 1919, https://doi.org/10.1038/s41467-018-04173-0
IPCC. Summary for Policymakers. In: Climate Change 2021: The Physical Science Basis. Contribution of Working Group I to the Sixth Assessment Report of the Intergovernmental Panel on Climate Change (eds. Masson-Delmotte, V. et al.) (Cambridge University Press. 2021) In Press.
Ono, J., Watanabe, M., Komuro, Y., Tatebe, H., & Abe, M. (2022). Enhanced Arctic warming amplification revealed in a low-emission scenario. Communications Earth & Environment, 3, 27, https://doi.org/10.1038/s43247-022-00354-4
Previdi, M., Smith, K. L. & Polvani, L. M. (2021). Arctic amplification of climate change: a review of underlying mechanisms. Environ. Res. Lett. 16, 093003
Rantanen, M., Karpechko, A.Y., Lipponen, A. et al. (2022). The Arctic has warmed nearly four times faster than the globe since 1979. Communications Earth & Environment, 3, 168, https://doi.org/10.1038/s43247-022-00498-3

OMp16

Characteristics of Scattering Ratio of Ultraviolet Radiation observed at Syowa Station

OHTAKE Jun[1]

[1] *Aerological Observatory, Japan Meteorological Agency*

Solar ultraviolet radiation (UV) down to the surface is divided into the direct component and the diffuse (i.e. scattered by the atmosphere) component. Observations of the diffuse component of UV have been carried out mainly in the mid-latitudes and have yielded a great deal of knowledge, but few studies have been reported with regards to the polar regions. At Syowa station (Syowa), Antarctica, observations of the global radiation of UV have been carried out as a part of basic observations of meteorology since 1993 [1] using the Brewer spectrophotometer (Brewer) [2]. In addition, UV observations of the diffuse component were carried out from 2013 to 2019. In this study, the characteristics of the scattering ratios (SR: ratio of diffuse component to global component) at the Syowa obtained from these observations are examined.

The Brewers used at the Syowa were calibrated in the same way as the UV observations conducted by the Japan Meteorological Agency (JMA) [3,4]. Brewer scans back and forth every 0.5 nm from 290 to 325 nm wavelength for one observation, and the wavelength-integrated value is called “total UV (TUV)”. Hourly UV observations are available on the JMA website [5] and the World Ozone and Ultraviolet Radiation Data Centre website [6]. In this study, an Automated Shadow Unit [7] was mounted to the Brewer’s azimuth tracker to make a shadow on the UVB dome at preset time to block direct component. To measure diffuse component and global component at the same time, two Brewers were operated; the diffuse component was measured with one and the global component was measured with the other.

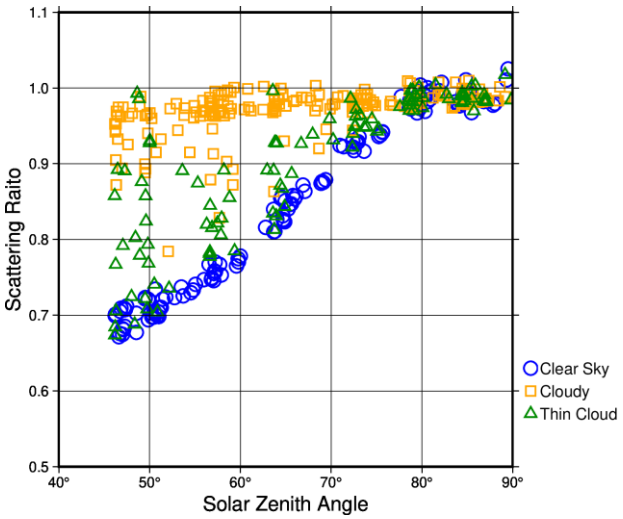

Figure 1. Scatter plot of TUV scattering ratio versus solar zenith angle at Syowa. The plot is categorized by weather, with blue circles for clear sky, orange squares for cloudy, and green triangles for thin cloud.

Figure 1 shows relation between TUV SR and SZA at Syowa, categorized by weather. For clear sky cases, SR were nearly constant between 0.96 and 1.01 when SZA were 76° to 85°; SR became smaller as SZA decreased when SZA were less than 76°; SR ranged from 0.67 to 0.71 when SZA were around 47°. In cloudy cases, SR were between 0.95 and 1.01 in many cases, and in some cases less than 0.95 when SZA were less than 76°. SR for thin cloud cases spread between those for clear sky and cloudy cases, and they overlapped in some cases. Figure 2 shows relation between SR and SZA at Syowa for three wavelengths (305, 315, and 325 nm). SR of longer wavelengths were comparatively lower at the same SZA for clear sky cases, but no regularity was found for cloudy cases.

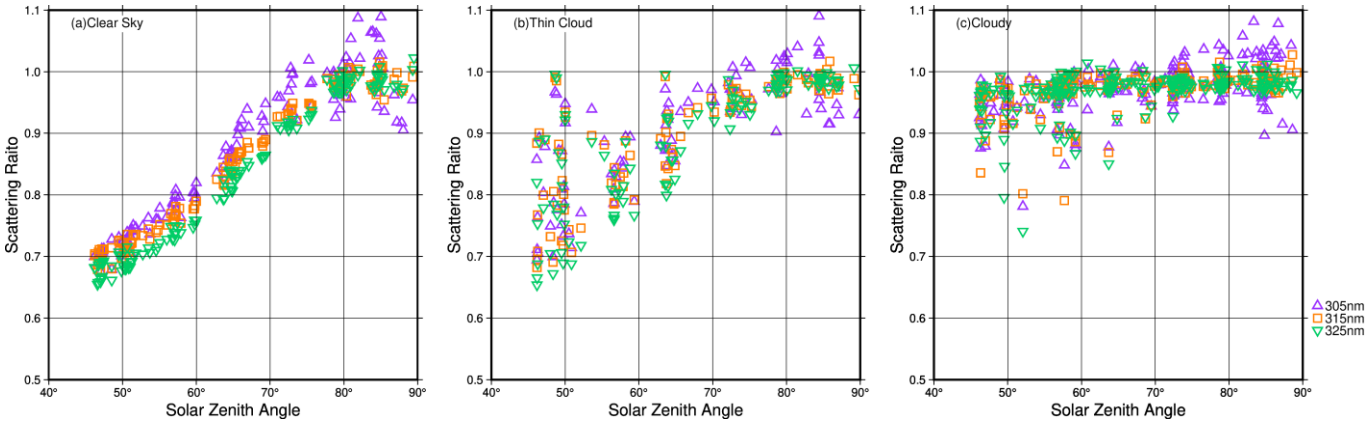

Figure 2. Scatter plots of scattering ratio of three wavelengths (305nm: purple triangles, 315nm: dark-orange square, 325nm: light-green downward-triangle) to the solar zenith angle at Syowa in clear sky(a), thin cloud(b) and cloudy(c) cases.

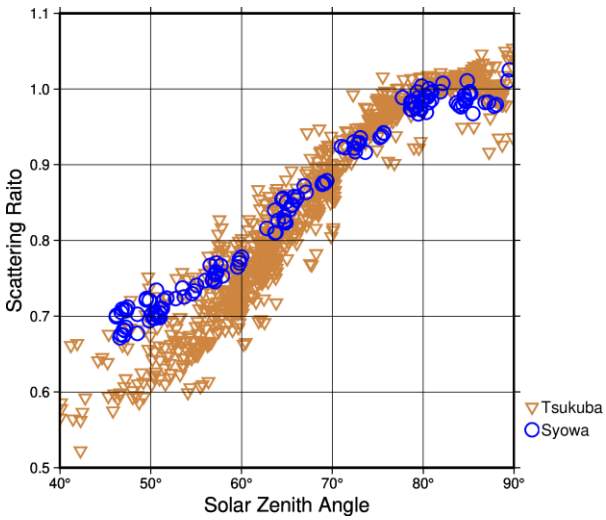

Figure 3. Scatter plot of the TUV scattering ratio against the solar zenith angle under clear sky cases. Syowa is shown as a blue circle and Tsukuba is shown as a dark-yellow downward-triangle.

To investigate features in the polar region, SR at Syowa was compared with those at Tsukuba, Ibaraki prefecture, Japan. Figure 3 shows relation between TUV SR and SZA under clear sky cases at Syowa and Tsukuba. When SZA was smaller than 70°, the minimum SR value was smaller at Tsukuba than that at Syowa. Since the surface albedo at Syowa is larger than that at Tsukuba, more UV is probably reflected at Syowa, and then this reflected UV is scattered by the atmosphere and also observed as the downward diffuse component.

In addition, the effect of SR on total ozone and aerosols will be reported on the day of the symposium.

References

[1] Takao, T., Koike, J., Kawata, Y., Sugita, O., Sakurai, K., 1996: Meteorological observations at Syowa Station in 1993 by the 34th Japanese Antarctic Research Expedition, Antarctic Record, Vol. 40, No. 2, 202-246. [in Japanese]
[2] Brewer MkIII Spectrophotometer, https://www.kippzonen.com/Product/50/Brewer-MkIII-Spectrophotometer
[3] Ito, T., Ueno, T., Kajihara R., Shitamichi, M., Uekubo T., Ito, M., Kobayashi, M., 1991: Development of Monitoring technique of Ultraviolet Irradiance on the Ground -An Assessment of UV-B Increase due to Ozone Depletion Based on Spectral Observations-, Journal of Metrological Research, Vol.43, No.5, 213-273. [in Japanese]
[4] Ito, M., Noto, Y., Miyagawa, K., Ueno, T., 2000: The Calibration Method and the Trend of Instrument Responsivity for Brewer Spectrophotometer in JAPAN, Journal of the Aerological Observatory, Vol.60, 45-56. [in Japanese]
[5] Annual Report on Atmospheric and Marine Environment Monitoring Data, https://www.data.jma.go.jp/env/data/report/data/index_e.html
[6] World Ozone and Ultraviolet Radiation Data Centre, https://woudc.org/https://woudc.org/
[7] Ito, M.,2006: Diffuse Spectral UVB Observation using Brewer Spectrophotometer and New Automated Shadow Unit, Journal of the Aerological Observatory, Vol.66, 47-56. [in Japanese]

Acknowledgment

I would like to thank Mr. ITO Mahito for proposing and preparing the observation of diffused UV component at Syowa Station and the members of JARE54 to JARE59 who carried it out.

Characteristics of cloud fraction from whole-sky camera observation onboard R/V *Shirase* from JARE 55 to JARE 61

* Makoto Kuji[1], Amiri Yokotani[2], Ayako Endo[3], Masahiro Hori[4] and Naohiko Hirasawa[5,6]
[1]*Division of Natural Sciences, Faculty, Nara Women's University*
[2]*Graduate School of Humanities and Sciences, Nara Women's University*
[3]*Faculty of Science, Nara Women's University*
[4]*School of Sustainable Design, University of Toyama*
[5]*National Institute of Polar Research, Research Organization of Information and Systems*
[6]*Department of Polar Science, School of Multidisciplinary Sciences, SOKENDAI (The Graduate University for Advanced Studies)*

Cloud has opposite effects on the earth climate system: warming and cooling. Their magnitudes depend on cloud fraction, height, and so on. They influence the radiation balance on the earth and cloud is one of the greatest error sources for the climate prediction [IPCC, 2021]. Nevertheless, it is not easy to make a detailed observation due to their spatial and temporal variability. Furthermore, we do not have enough observation sites, especially over the ocean. It is, therefore, important to elucidate their behavior in detail. The analysis of clouds over the Southern Ocean is important in terms of climate model improvement and cloud feedback studies, because many climate models do not adequately represent clouds over there [Trenberth and Fasullo, 2010]. Thus, we made a periodical shipboard observation to investigate maritime cloud using whole-sky camera, ceilometer and visual observations onboard R/V *Shirase* between Japan and Antarctica. In this study, we reanalyzed the observation data with new classification curves and investigated cloud fraction for a total of seven years from JARE 55 to JARE 61, i.e., from 2013 to 2020.

Shipboard observations were carried out onboard R/V *Shirase* (AGB-5003) [Kuji et al., 2016]. The whole-sky camera system mainly consists of a digital camera (NIKON D7000, NIKON Corporation) and a circular fisheye lens (4.5 mm F2.8 EX DC Circular Fisheye HSM, SIGMA Corporation) to take a photo of a whole sky. The observation interval was 5 min. We estimated cloud fraction from whole-sky camera images based on a cloud detection method [Yoshimura and Yamashita, 2013]. Furthermore, we analyzed the whole-sky images over sea ice region as a function of solar height because sea surface albedo over sea ice regions is very different from that over open ocean [Kuji et al., 2018].

As a result, the daily-averaged cloud fraction was generally more than 55 % in all seven cruises over the Southern Ocean. Furthermore, we examined the cloud fraction in three areas: sea ice, outward and return open water areas. It is found that the average cloud fraction was more than 70 % only in the open water areas. These results suggest that cloud fraction tends to be particularly large in the open waters over the Southern Ocean from December to March of each observation year.

Acknowledgments
The shipborne whole-sky camera observations were conducted in cooperation with Japan Aerospace Exploration Agency (JAXA) and National Institute of Polar Research. The authors are grateful to those who related to observations onboard R/V *Shirase* during JARE 55-61.

References

Hirose, S., M. Takada, M. Kuji, and M. Hori, Characteristics of cloud fractions from whole-sky camera observations onboard R/V *Shirase* from 2013 to 2020, The 12th Symposium on Polar Science, OMp17, 2021.

Intergovernmental Panel on Climate Change (IPCC2021), Climate Change 2021.

Kuji, M., R. Fujimoto, M. Miyagawa, R. Funada, M. Hori, H. Kobayashi, S. Koga, J. Matsushita, and M. Shiobara, Cloud fractions estimated from shipboard whole-sky camera and ceilometer observations, *Transactions of the Japan Society for Aeronautical and Space Sciences*, **14**, 7-13, 2016.

Kuji, M., A. Murasaki, M. Hori, and M. Shiobara, Cloud Fractions Estimated from Shipboard Whole-sky Camera and Ceilometer Observations between East Asia and Antarctica. *J. Meteor. Soc. Japan*, **96**, 201-214, 2018.

Trenberth, K. E., and J. T. Fasullo, Simulation of present-day and twenty-first-century energy budgets of the southern oceans. *J. Climate*, **23**, 440-454, 2010.

Yoshimura, M. and M. Yamashita, Contribution of Ground-Based Cloud Observation to Satellite-Based Cloud Discrimination, *J. Environ. Sci. Eng*. A, **2**, 379-382, 2013.

Characteristics of cloud fraction from whole-sky camera observation onboard R/V *Shirase* during JARE 57

*Amiri Yokotani[1], Ayako Endo[2], Makoto Kuji[3], Masahiro Hori[4] and Naohiko Hirasawa[5,6]
[1]*Graduate School of Humanities and Sciences, Nara Women's University*
[2]*Faculty of Science, Nara Women's University*
[3]*Division of Natural Sciences, Faculty, Nara Women's University*
[4]*School of Sustainable Design, University of Toyama*
[5]*National Institute of Polar Research, Research Organization of Information and Systems*
[6]*Department of Polar Science, School of Multidisciplinary Sciences, SOKENDAI (The Graduate University for Advanced Studies)*

Cloud has opposite effects on the earth climate system: warming and cooling. Their magnitudes depend on cloud fraction, height, and so on. They influence the radiation balance on the earth and cloud is one of the greatest error sources for the climate prediction [IPCC, 2021]. Nevertheless, it is not easy to make a detailed observation due to their spatial and temporal variability. Furthermore, we do not have enough observation sites, especially over the ocean. It is, therefore, important to elucidate their behavior in detail. Thus, we made a periodical shipboard observation to investigate maritime cloud using whole-sky camera, ceilometer and visual observations onboard R/V *Shirase* between Japan and Antarctica. In this study, we reanalyzed the observation data with new classification curves.

Shipboard observations were carried out onboard R/V *Shirase* (AGB-5003) [Kuji et al., 2016]. The whole-sky camera system mainly consists of a digital camera (NIKON D7000, NIKON Corporation) and a circular fisheye lens (4.5 mm F2.8 EX DC Circular Fisheye HSM, SIGMA Corporation) to take a photo of a whole sky. The observation interval was 5 min. We analyzed 29,861 images from 16 November 2015 to 11 April 2016 (JARE 57). We estimated cloud fraction from whole-sky camera images based on a cloud detection method [Yoshimura and Yamashita, 2013]. Furthermore, we analyzed the whole-sky images over sea ice region as a function of solar height because sea surface albedo over sea ice regions is very different from that over open ocean [Kuji et al., 2018]. The ceilometer was an instrument to determine cloud base heights by measuring the return time of laser beam (Vaisala CL51). The observation interval was 36 s. We have 221,675 profiles from 16 November 2015 to 11 April 2016 (JARE 57). We can obtain up to three cloud base heights with the software built in the system. The cloud fraction with the ceilometer was defined as a frequency of cloud appearance, that is, the ratio of cloudy to total effective profiles. In addition, we can use the cloud fraction by visual observation as one of the meteorological datasets. The observation interval 1 h. We have 2,475 cloud fractions from 16 November 2015 to 11 April 2016 (JARE 57).

As a result, it is found that the variation of cloud fractions is generally consistent: the correlation coefficients between the whole-sky camera versus the ceilometer and the visual observations are very high with 0.92 and 0.85, respectively.

We are going to examine the characteristics of the cloud fraction estimated from the whole-sky camera on the ship tracks. Furthermore, we will make a validation study comparing the cloud fractions from R/V *Shirase* as well as satellite observations.

Acknowledgments

The shipborne whole-sky camera observations were conducted in cooperation with Japan Aerospace Exploration Agency (JAXA) and National Institute of Polar Research. The authors are grateful to those who related to observations onboard R/V *Shirase* during JARE 55-61.

References

Intergovernmental Panel on Climate Change (IPCC2021), Climate Change 2021.

Kuji, M., R. Fujimoto, M. Miyagawa, R. Funada, M. Hori, H. Kobayashi, S. Koga, J. Matsushita, and M. Shiobara, Cloud fractions estimated from shipboard whole-sky camera and ceilometer observations, *Transactions of the Japan Society for Aeronautical and Space Sciences*, **14**, 7-13, 2016.

Kuji, M., A. Murasaki, M. Hori, and M. Shiobara, Cloud Fractions Estimated from Shipboard Whole-sky Camera and Ceilometer Observations between East Asia and Antarctica. *J. Meteor. Soc. Japan*, **96**, 201-214, 2018.

Kuji, M., A. Murasaki, M. Hori, M. Takeda, J. Matsushita, and M. Shiobara, Characteristics of cloud fractions from whole-sky camera observations onboard R/V *Shirase*, The Seventh Symposium on Polar Science, OMp14, 2016.

Yoshimura, M. and M. Yamashita, Contribution of Ground-Based Cloud Observation to Satellite-Based Cloud Discrimination, *J. Environ. Sci. Eng*. A, **2**, 379-382, 2013.

OMp19

The long-term changes in the glaciers of Kaffiøyra region, Svalbard, Arctic

Ireneusz Sobota, Kamil Czarnecki, Marcin Nowak
Nicolaus Copernicus University in Toruń, Department of Hydrology, Cryology and Water Management, Polar Research Center, Poland

The primary objective of this research is to present the essential conditions and characteristics of changes in the dynamics and spatial extent of the glaciers in the Kaffiøyra region. Most of the research consisted of direct field measurements carried out in 1996–2024, and the investigated changes were mainly related to the mass balance on glaciers, and remote sensing methods and field observations documented the changes in glaciers.

Kaffiøyra is a coastal plain in northwestern Spitsbergen (Oscar II Land) – the largest island of the Svalbard archipelago. There are nine glaciers located in the Kaffiøyra region that terminate on the land. These include valley glaciers which terminate on the plain (Waldemarbreen, Irenebreen, Elisebreen, Agnorbreen, Eivindbreen, Andreasbreen and Oliverbreen), as well as glaciers that define the boundaries of plains and which end in the sea (Aavatsmarkbreen in the north and Dahlbreen in the south).

An analysis of the extent of valley glaciers in this area showed that since 1909, glaciers have been in a greater or lesser recession phase. The recession of the glaciers in the Kaffiøyra area during the analysis period results from a negative trend in the mass balance and dynamics of the Svalbard glaciers. The rapid and substantial changes in the mass balance of glaciers occurring in recent years are also reflected in a growing rate of surface area shrinkage. From the maximum advance to 2023, the glaciers in this area decreased by about 50% on average. The slightest change was recorded for Elisebreen and Eivindbreen Waldemarbreen, while the largest was for Oliverbreen and Andreasbreen.

The changes in the position of the fronts of Kaffiøyra region glaciers, which coincide with the north-western coast of Spitsbergen, are similar to changes observed for other Svalbard glaciers of this type. The recession of these glaciers results from large changes in the mass balance and dynamics of Svalbard glaciers that began at the turn of the 20th century and notably increased in intensity during the last 15–20 years.

OMp20

Can the spatio-temporal distribution of recent snow cover in the Northern Hemisphere be explained by variations in the Arctic Oscillation Index?

Masahiro Hori[1], Masashi Niwano[2,4], Rigen Shimada[3], Teruo Aoki[4,2]

[1]*University of Toyama*
[2]*Meteorological Research Institute*
[3]*Japan Aerospace Exploration Agency*
[4]*National Institute of Polar Research*

Snow cover is an essential variable to be monitored from space for assessing the effect of the global warming on the Arctic region. We have evaluated the long-term trends of snow cover duration in the Northern Hemisphere and revealed that the significant negative trends of annual snow cover duration (SCD) occurred in Europe region and positive trends in parts of the United States of America and Canada during the past two decades (2001-2020) (Hori et al., 2021). The significant negative SCD trends in Europe were found to be mainly caused by the earlier snow melt in spring, while the positive SCD trends in the US are due to earlier snow fall in autumn (Hori et al, 2023). In this study we analyzed the regression and correlation between the Arctic Oscillation index (AOI) and SCD, and found that the spring negative SCD trends in Europe are negatively correlated with AOI whereas the autumn positive SCD trends in the US are not well correlated with AOI. The spring negative trends in SCD are considered to result from the recent increase (positive trend) of AOI in spring. On the other hand, the mechanism by which SCD has been becoming positive in the autumn in the U.S. might be due to climatic changes in atmospheric circulation patterns (e.g., meandering pattern of westerly winds) prevailing during the season.

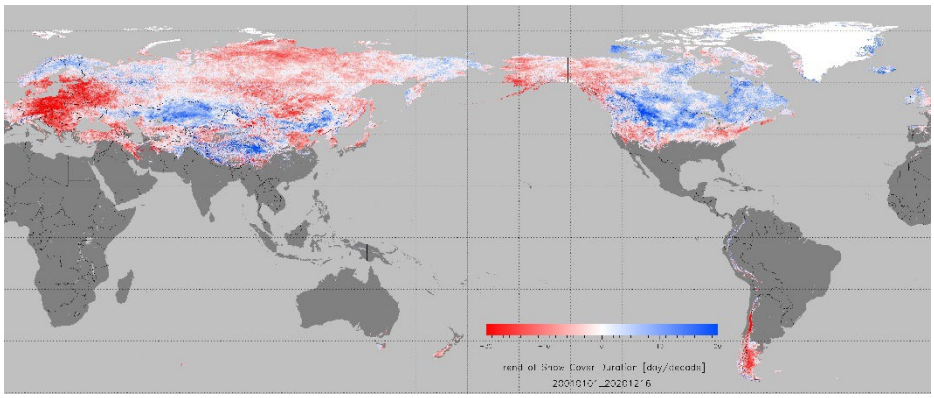

Figure 1. Spatial distributions of long-term trends of snow cover duration (SCD, day/decade) in the Northern Hemisphere for the period of 2001-2020 (20 years).

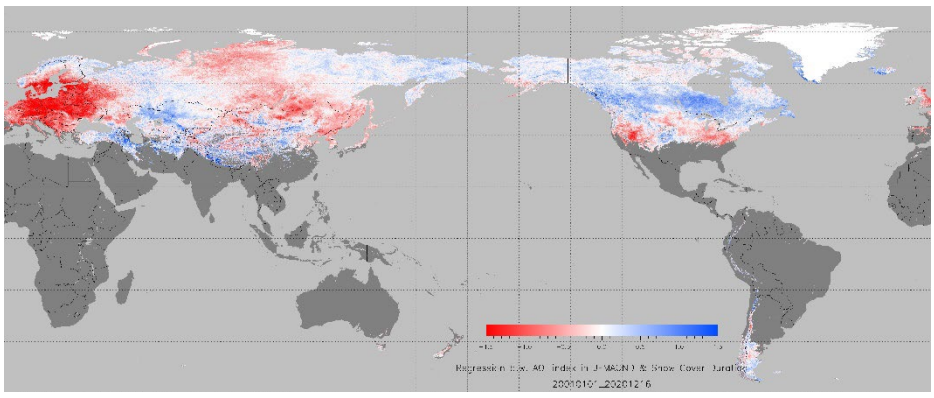

Figure 2. Regression coefficient maps between the Arctic Oscillation index in snowy months (Jan.- Apr., Oct.- Dec.) and the SCD during the period of 2001-2020 (20 years).

References

Hori, M., M. Niwano, R. Shimada, T. Aoki, Heterogeneous response of snow cover in the Northern Hemisphere to the recent Arctic warming, The 12th Symposium on Polar Science, Online, 2021.

Hori, M., M. Niwano, R. Shimada, T. Aoki, Time series analysis of snow cover duration in the Northern Hemisphere during the recent 20 years, The 14th Symposium on Polar Science, Tachikawa, 2023.

OMp21

Formation and abrupt drainage of Setevatnet, a glacial lake of Kongsvegen in Svalbard

Takuro Imazu[1,2], Shin Sugiyama[1] and Shuntaro Hata[1]
[1] *Institute of Low Temperature Science, Hokkaido University*
[2] *Graduate School of Environment Science, Hokkaido University*

Abrupt glacial lake drainage elevates basal water pressure and enhances glacier sliding. Studying such an event is important for understanding the relationship between the glacier hydrology and ice dynamics (Chuldley et al., 2019). Setevatnet is a glacial lake formed in a valley between Kongsvegen and Uvêrsbreen in Svalbard (78°49' N, 12°37' E) (Fig. 1). The lake was discovered in 1906 and its abrupt drainage was first reported in 1975 (LiestøL, 1976). While the drainage of lake water into the base of Kongsvegen has occurred annually in recent years, the impact of the drainage on the hydrology and dynamics of the glacier is not well understood. To better understand the impact of the lake drainage on the glacier, field observations using a geophone, an acoustic sensor, and a time-lapse camera were carried out on/near the glacier in the spring of 2024 (Fig. 1b). This presentation reports the most recent formation and abrupt drainage of Setevatnet in July 2024 based on remote sensing. We also report seismic data obtained from April to August 2024.

The surface area and water volume of Setevatnet were measured from 3 May to 12 August 2024, using 38 satellite images acquired by the Sentinel-2 multispectral imager. The spatial resolution of the images was 10 m. To quantify the lake area, we utilized normalized differential water index (NDWI) calculated within the study area (red box in Fig. 1) (McFeeters, 2013). We used a threshold (0.32–0.40) of NDWI to distinguish the pixels of the lake surface. To obtain the bathymetry of Setevatnet, we used three strips of ArcticDEM (version 4.1) acquired after the drainage. The lake-surface elevation was estimated from the lake shoreline of each image, which was used to compute the water volume from the bathymetry. In the field, we installed a geophone (SM-6/H-B Style 4.5 Hz) 1 m below the ice surface, and the device was connected to DATA-CUBE^3 to record data with a sampling frequency of 200 Hz. We identified icequake activities by comparing the short- (0.4 seconds) and the long-term (60 seconds) average of the vertical component above 25 Hz (Beyreuther et al., 2010). We counted the number of events based on the STA/LTA ratio, by taking the ratio of 20 and 10 as the event initiation and termination.

The lake gradually expanded from 27 May to 2 July with maximum lake area and water volume of $1.80\times10^5 \pm 0.15\times10^5$ m^2 and $3.5\times10^6 \pm 0.6\times10^6$ m^3, respectively. The lake drainage began between 2 and 4 July and the lake was almost empty on 16 July (Fig. 2). According to the water volume change, the mean rate of discharge from 2 to 16 July was 2.9 ± 0.5 m^3 s^{-1}. The number of seismic events increased rapidly when the lake began to form at the end of May and gradually decreased during the drainage (Fig. 2). The increase in the number of events during the lake expansion implies that the lake was connected to subglacial or englacial conduits.

In the presentation, we will discuss the drainage mechanism and the impact of drainage on the ice dynamics with additional field data obtained with an acoustic sensor and a time-lapse camera.

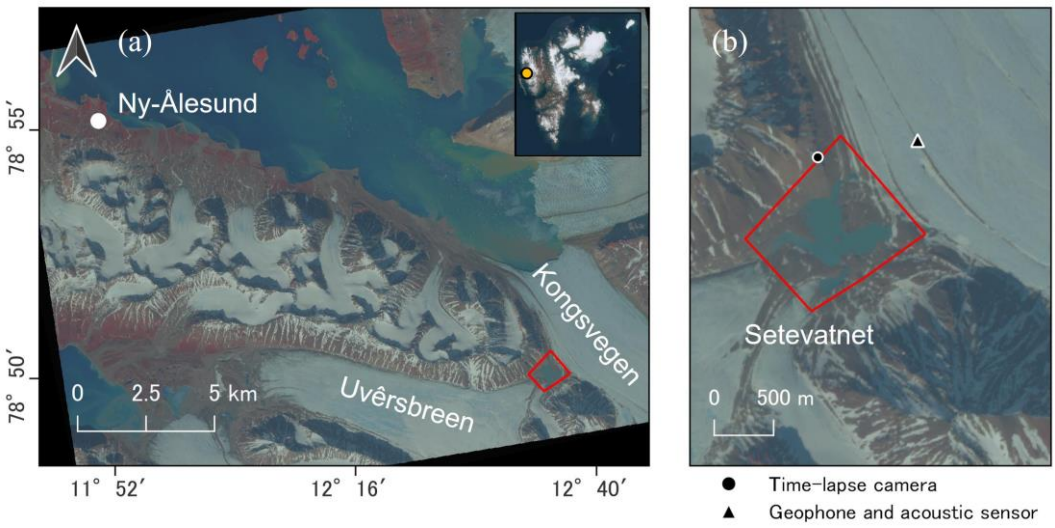

Figure 1. (a) The false-color stellate image on 4 July 2023 acquired by Sentinel-2. The inset shows the location of the study site in Svalbard. The red box shows the location of Setevatnet. (b) The enlarged map of (a) for Setevatnet. The location of the geophone and the acoustic sensor (▲), and the time-lapse camera (●) installed in the spring of 2024.

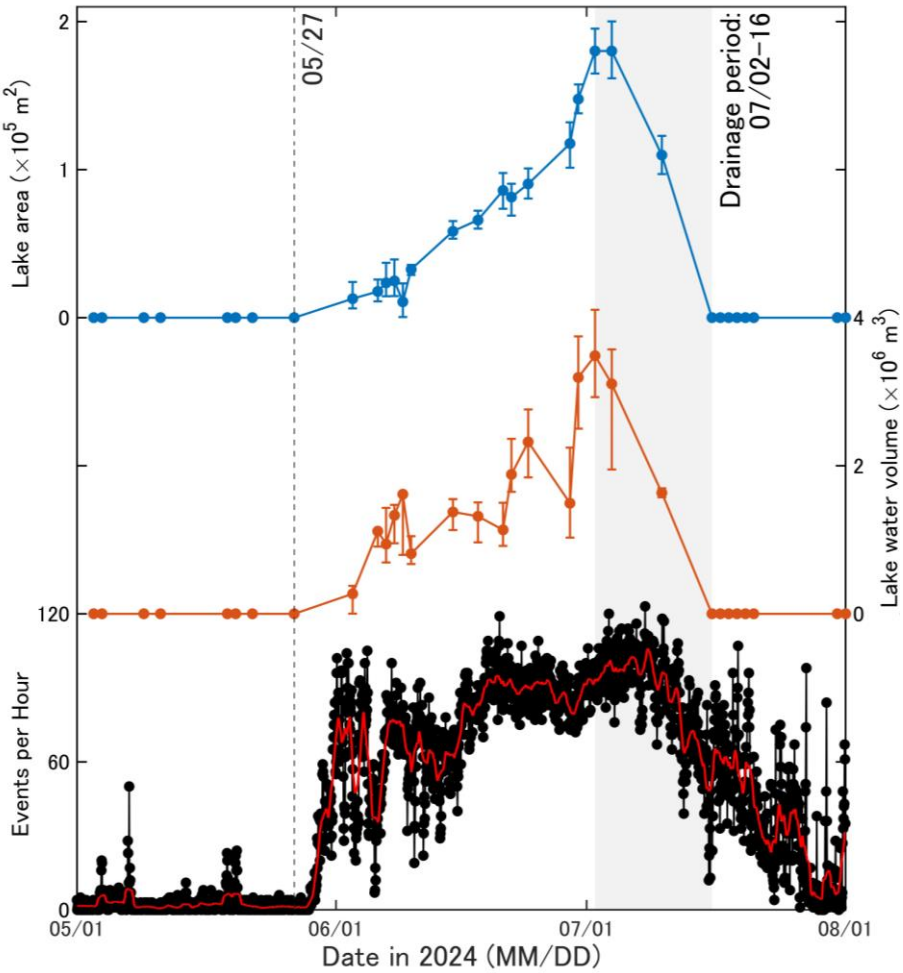

Figure 2. The area (blue) and water volume (red) of Setevatnet, and seismic events on Kongsvegen (black) from 1 May to 1 August 2024. Uncertainties in the measurements area indicated by the error bars. A red curve associated with the seismic events is 24-h-window running mean. The vertical dashed line indicates the date of lake formation (27 May 2024). The grey shaded area shows the period of the drainage event from 2 to 16 July 2024.

References

Beyreuther, M. and 5 others, Obspy: A python toolbox for seismology, Seismological Research Letters, 81(3), 530–533, 2010.

Chudley, T.R. and 6 others, Supraglacial lake drainage at a fast-flowing Greenlandic outlet glacier, Proc. Natl. Acad. Sci, 116, 25468–25477, 2019.

LiestøL, O., Setevatnet, a glacier dammed lake in Spitsbergen, Norsk Polarinstitutt Arbok, 1975, 31–35, 1976.

McFeeters, S. K., Using the normalized difference water Index (NDWI) within a geographic information system to detect swimming pools for mosquito abatement: a practical approach, Remote Sensing, 5, 3544–3561, 2013.

OMp22

Mineral dust variations over the past 1000 years at EGRIP, northeastern Greenland

Yuki Komuro[1,2], Fumio Nakazawa[1,3], Kumiko Goto-Azuma[1,3], Naoko Nagatsuka[4], Motohiro Hirabayashi[1], Jun Ogata[1], Kaori Fukuda[1], Naoyuki Kurita[5], Koji Fujita[5], Ayaka Yonekura[6], Kyotaro Kitamura[1], Giulia Sinnl[7], Sune Olander Rasmussen[7], Trevor James Popp[7], Dorthe Dahl-Jensen[7]

[1]*National Institute of Polar Research*

[2]*Laboratory for Environmental Research at Mount Fuji*

[3]*The Graduate University for Advanced Studies, SOKENDAI*

[4]*Japan Agency for Marine-Earth Science and Technology*

[5]*Nagoya University*

[6]*Marine Works Japan*

[7]*University of Copenhagen*

Temporal variations in mineral dust concentrations on the Greenland ice sheet are associated with temporal variations in ground surface conditions on their source regions and their transportation processes. For example, the decrease of snow-covered area in the Greenland coast due to global warming can increase exposed soil area, thus increase mineral dust supplied from the coasts. Aridification of Asian arid regions, which are likely major distant sources of mineral dust, and enhanced westerly winds can increase the mineral dust supply from those regions. The mineral dust from distant sources is dominated by fine mineral particles, while that from the coast contains coarse mineral particles. Therefore, the analysis of coarse mineral dust concentration can allow us to evaluate the mineral dust supply from the coast. In addition, Ca concentrations can be used to evaluate the contribution of mineral dust from arid regions, as soils in arid regions are rich in calcium salts such as calcite. To understand the relationship between variations in mineral dust and climate, we analyzed a shallow ice core drilled at the East Greenland Ice Core Project (EGRIP) site. In this study, we report the analysis results of particle size distribution and elemental concentrations in mineral dust.

The ice core was analyzed using a continuous-flow analysis (CFA) system at NIPR. Elemental concentrations (Na, Mg, Al, Si, S, K, Ca, and Fe) were measured by an ICP-MS (Agilent technologies, 7700). Assuming that S was derived completely from SO_4, SO_4 concentrations were calculated from the S concentrations. For mineral dust analyses, a portion of meltwater was collected using a fraction collector at a depth interval of 0.12 m. Concentrations and size distributions (0.7–18 μm) of mineral dust in the collected samples were measured by a Coulter counter (Beckman Coulter, Multisizer 4e). Additionally, for tritium measurements, ice core samples at depths of 13–15 m were cut and melted. Tritium measurements of the samples were conducted using a scintillation counter (ParkinElmer, Quantulus 1220).

For dating of the ice core, we conducted annual layer counting primarily based on the seasonal variation in Na. As fixed date layers, we used a tritium peak, volcanic layers, and ice layers. Based on these analyses, the ice core was estimated to cover the past approximately 1000 years. The average size distribution of mineral dust mass concentrations showed a unimodal shape with a mode diameter of around 2 μm. Thus, the mineral dust deposited at EGRIP likely came mainly from distant source regions. The concentration of coarse mineral dust (> 5 μm) increased after 1615, suggesting that the mineral dust supply from the Greenland coast increased after that year. The variation of coarse dust concentration after 1900 significantly correlated with the Greenland Blocking Index. Thus, the variation of mineral dust from the coast after 1900 was likely related to the variation of atmospheric pressure over Greenland. To estimate the concentration of distant-source mineral dust, we subtracted the concentration of coastal-source mineral dust from the total concentration of mineral dust (0.7–10 μm). The concentration of mineral dust calculated by this method showed a variation similar to that of non-sea-salt Ca, which is considered to originate mainly from arid regions. Therefore, it is suggested that the calculated concentration corresponds to the concentration of mineral dust from distant arid regions. The calculated concentration after 1900 significantly correlated with the Arctic Oscillation Index, suggesting that the variation of mineral dust supply from the distant arid regions after that year was related to the variation of the Arctic Oscillation. In the presentation, we will report the results of more detailed comparisons between the mineral dust concentrations obtained from this study and paleoclimate data from previous studies.

Reconstruction of atmospheric CH_4 concentration history since the Industrial Revolution from the SE-Dome II ice core, southeastern Greenland

Mai Suzuki[1], Ikumi Oyabu[2, 1], Kenji Kawamura[2, 1, 3], Yoshinori Iizuka[4]
[1]*Graduate Institute for Advanced Studies, SOKENDAI*
[2]*National Institute of Polar Research, Research Organization of Information and Systems*
[3]*Japan Agency for Marine Science and Technology*
[4]*Institute of Low Temperature Science, Hokkaido University*

1. Introduction

Methane (CH_4) is one of the most important greenhouse gases and is emitted from both natural and anthropogenic sources. Direct observations of atmospheric CH_4 started only in the 1980s; thus, we need to reconstruct the past concentrations from ice cores to gain the knowledge on the histories of anthropogenic source strengths and natural source changes associated with climatic changes since the Industrial Revolution. Also, inter-polar difference (IPD) of CH_4 concentration may provide a clue for the latitudinal distribution of CH_4 emissions, which may be reconstructed if accurate ice core data are available from both Antarctica and Greenland. Accurate concentration histories are also important as input data for climate models. However, high-resolution and high-precision CH_4 data for the industrial period is only available from the Law Dome ice core from Antarctica, which was drilled at a high-accumulation site (about 1 m w.e.year^{-1}). There have been no high-quality data from Greenland, because of in-situ production of CH_4 in high-impurity layers in the ice sheet and the lack of ice cores from Greenland with very high accumulation rate like the Law Dome core. In this study, we have overcome these problems and reconstructed the CH_4 concentration between 1841 A.D. and 2004 A.D. by analyzing the SE-Dome II ice core (67°19'17" N, 36°47'03" W, 3,161m a.s.l , accumulation rate:1.04 ± 0.20 m w.e.year^{-1}), southeastern Greenland (Iizuka et al., 2021; Kawakami et al., 2023).

2. Method

The SE-Dome II ice core was drilled at the southeastern dome summit in 2021 to the depth of ~250 m (Iizuka et al., 2021) with a primary objective of reconstructing ultrahigh-resolution aerosol histories at seasonal scales. Various physical and chemical analyses have been conducted on the SE-Dome II core. For this study, a cross section of ~6 cm^2 was allocated from 66-m depth to the bottom of the core. The core samples were cut at the Institute of Low Temperature Science, Hokkaido University, and transported to the National Institute of Polar Research (NIPR) in March 2024.

At NIPR, an ice sample of 110 ~ 160 g was cut out from a bulk ice-core sample with a band saw. The length of each sample was determined to contain approximately 1 year of accumulation, according to the published ice age scale based on annual layer counting of H_2O_2 profile (Kawakami et al., 2023). We chose the 1-year length for each sample to minimize the possible age reversal or age discontinuity of trapped gases due to inhomogeneous gas trapping in the bubble close-off region at the bottom of firn.

Then, all faces of the sample were trimmed by ~1 mm with the band saw, and further shaved off by a ceramic knife for decontamination. The shaving of the surfaces is also helpful for finding any cracks that should be removed. The sample mass after the preparations is 100 - 150g. The air in the ice sample was extracted with an established wet-extraction technique (Fig. 1, Oyabu et al., 2020). The extracted air was split into two aliquots for mass spectrometric (Thermo Delta V) and gas chromatographic (Agilent 7890A) measurements. The concentrations of CH_4, CO_2 and N_2O were measured with the gas chromatograph, and isotopic and elemental ratios ($\delta^{15}N/^{14}N$ of N_2, $\delta^{18}O/^{16}O$ of O_2, $\delta O_2/N_2$ and $\delta Ar/N_2$) were measured with the mass spectrometer (Oyabu et al., 2020).

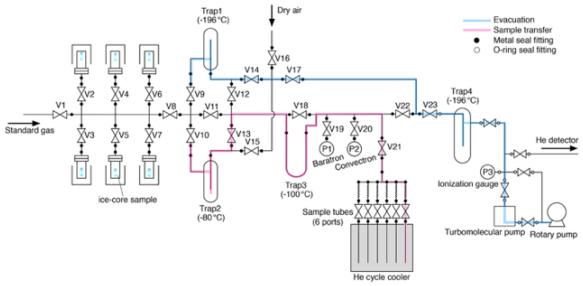

Fig. 1 Schematic diagram of the wet-extraction system. (Oyabu et al., 2020)

3. Results and discussion

We analyzed 170 samples from the depths of 251 - 78m, and the age of extracted air was estimated to be between 1841 C.E. and 2004 C.E., as follows. The air bubbles are closed off at the bottom of firn, so the age of ice and gas are different at the same depth, i.e., we cannot reconstruct the CH_4 history by using the ice age. In this study, we compared the CH_4 data of SE-Dome II core to that of Law Dome core and estimated the gas age, by matching the timings of major changes in the CH_4 increase rate. We here assumed that the difference between the ice age and gas age (known as Δage) is constant through time and that the age scale of the Law Dome core is correct. The Δage for the SE-Dome II core thus temporarily estimated is 41 years.

The CH_4 concentrations from the SE-Dome II core increased gradually from ~830 ppb in the 1840's to ~1000ppb in the early 1950's, and then rapidly from the late 1950's to the end of the 20th century (>1800ppb). The overall CH_4 increase in Greenland was ~1000ppb over the ~160 years, which is four times as large as the largest abrupt increase at the end of the last glacial-interglacial transition.

Compared to the widely known, high-resolution CH_4 dataset from the NEEM ice core, northwestern Greenland, showing artifactual spikes of up to ~150 ppb above a 10-year moving average due to in-situ CH_4 production (Rhodes et al., 2013), we do not find anomalous values in the SE-Dome II data, suggesting a successful CH_4 reconstruction for the most of industrial period up to the early 2000's. We speculate that the apparent lack of CH_4 contamination in our data is primarily the low concentration of impurities in the SE-Dome II core due to extremely high accumulation rate. Also, anomalous CH_4 values, even if produced locally within a layer of high impurity content, might be diluted because of the long sample (~1m).

The CH_4 growth rate from the SE-Dome II core was 3.1 ppb/year for 1841 - 1948 C.E., 14.7 ppb/year for 1949 - 1991 C.E., and 3.9 ppb/year for 1992 - 2004 C.E. A main finding from our data is the very rapid CH_4 concentration increase from the middle of 20th century to the early 1990's. The growth rate then significantly slowed down and presented the similar trend to the direct observations. The average growth rate in the 1980's was >40 ppb/year, which is twice as large as the growth rate at Point Barrow (Alaska) in the late 1980's. The growth rate from the SE-Dome II data is in agreement with that of the direct arctic observation for the overlapping period. We thus suggest that the rapid CH_4 increase in the 1980's is a true atmospheric signal of the Arctic, and that the most rapid CH_4 increase occurred just before the beginning of the direct atmospheric CH_4 observations.

References

Iizuka et al., Ice core drilling and related observations at SE-Dome site, southeastern GrIS Ice Sheet, *Bulletin of Glaciological Research*, **39**, 1-12, 2021.

Kawakami et al., SE-Dome II Ice Core Dating With Half-Year Precision:Increasing Melting Events From 1799 to 2020 in Southeastern Greenland, *J. Geophys. Res.*, **128**, e2023JD038874, 2023.

Oyabu et al., New technique for high-precision, simultaneous measurements of CH_4, N_2O and CO_2 concentrations; isotopic and elemental ratios of N_2, O_2 and Ar; and total air content in ice cores by wet extraction, *Atmos. Meas. Tech*., **13**, 6703–6731, 2020.

Rhodes et al., Continuous methane measurements from a late Holocene Greenland ice core: Atmospheric and in-situ signals, *Earth and Planetary Science Letters*, **368**, 9-19, 2013.

Rubino et al., Revised records of atmospheric trace gases CO_2, CH_4, N_2O, and $\delta^{13}C$-CO_2 over the last 2000 years from Law Dome, Antarctica, *Earth Syst. Sci. Data*, **11**, 473–492, 2019.

Umezawa et al., Towards reconstructing the Arctic atmospheric methane history over the 20th century: measurement and modelling results for the North Greenland Ice Core Project firnm, *Atmos. Chem. Phys.*, **22**, 6899–6917, 2022.

OMp24

Associations between cyanobacteria and mineral particles in cryoconite on Greenland glaciers

Naoko Nagatsuka[1], Jun Uetake[2], Rigen Shimada[3] and Nozomu Takeuchi[4]
[1]*JAMSTEC*
[2]*Hokkaido University, The Field Science Center for Northern Biosphere*
[3]*JAXA*
[4]*Chiba University*

Cryoconite is a biogenic surface dust mainly composed of mineral particles transported by wind from local or distant terrestrial surfaces (e.g., Bøggild et al., 2010 ; Nagatsuka et al., 2016) and organic matter produced by microbial activity on glaciers (e.g. Takeuchi et al., 2014). Due to its dark coloration, cryoconite can reduce the surface albedo of glaciers, thereby accelerating their melting, particularly in Arctic regions. Cyanobacteria, the primary agents in cryoconite formation, are thought to promote cryoconite development by encasing mineral particles and organic matter in a sticky biofilm. Additionally, minerals on glaciers may serve as nutrient sources for these microbes, potentially influencing cryoconite formation and albedo reduction. To investigate the impact of mineral dust on microbial production and cryoconite abundance, we analyzed the morphology and composition of minerals in cryoconites on glaciers in northeastern (Qaanaaq Glacier) and southwestern (Isunguata Sermia Glacier) Greenland using scanning electron microscopy (SEM) and energy-dispersive X-ray spectroscopy (EDS).

Our results revealed differences in the dominant cyanobacterial species between the two glaciers. In Qaanaaq Glacier, *Phormidesmis* sp. was the predominant species, while in Isunguata Sermia Glacier, the larger cell type, *Calothrix* sp. was more abundant. The minerals attached to the surface of cyanobacteria in both glaciers were predominantly smaller than 2 μm and mainly consisted of silicate minerals. However, there were significant differences in mineral compositions between the glaciers. In Qaanaaq Glacier, mica and chlorite, containing K, Mg, and Fe, constituted 90% of the minerals in cryoconite. In contrast, Isunguata Sermia Glacier exhibited a higher proportion of amphibole, containing Mg, Ca, and Fe. These variations in mineral composition are likely influenced by the surrounding geological context of each glacier, indicating a link between mineral composition and local geology. The mineral composition also differed between the two cyanobacterial species. The minerals attached to *Phormidesmis* had a lower proportion of amphibole and a higher proportion of mica and chlorite compared to those attached to *Calothrix* in both glaciers. This suggests that the mineral composition of cryoconite affect the dominant cyanobacterial species in each glacier

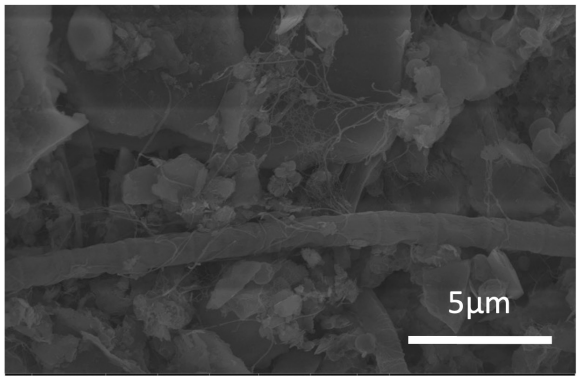

Figure 1. SEM image of cyanobacteria and mineral particles in cryoconite

References

Bøggild, C. E., Brandt, R., Brown, K., and Warren, S. G., The ablation zone in northeast Greenland: ice types, albedos and impurities. J. Glaciol. 56, 101–113, 2010.

Nagatsuka, N., Takeuchi, N., Uetake, J., Shimada, R., Onuma, Y., Tanaka, S., and Nakano, T., Variations in Sr and Nd Isotopic Ratios of Mineral Particles in Cryoconite in Western Greenland. *Front. Earth Sci.* 4:93., 2016.

Takeuchi, N., Nagatsuka, N., Uetake, J., and Shimada, R., Spatial variations in impurities (cryoconite) on glaciers in northwest Greenland. Bull. Glaciol. Res. 32, 85–94, 2014.

Determination of ammonium ion concentrations by continuous flow analysis

Motohiro Hirabayashi[1] and Jun Ogata[1]
[1]*National Institute of Polar Research*

1. Introduction

Snow and ice in the polar regions reflect the atmospheric environment at the time of snow accumulation. Analysis of snow and ice cores can provide information on the past atmospheric environment. Ice cores collected from the Antarctic ice sheet and other regions provide a continuous record of the environment at the time of accumulation over hundreds of thousands of years. We have developed continuous flow analysis (CFA) system to analyze ice cores while melting them in order to save labor, reduce sample volume, increase processing speed, and improve the time resolution of ice core analysis.

Nitrogen-containing inorganic compounds in the Antarctic region are deeply related to the Southern Ocean ecosystem and the formation of the ozone hole, and it is extremely important to understand their behavior. Analysis of nitrogen-containing inorganic compounds in Antarctic snow and ice can be a helpful tool for understanding the nitrogen cycle.

Among nitrogen-containing inorganic compounds, ammonium ion (NH_4^+), nitrate ion (NO_3^-), and nitrite ion (NO_2^-) had been analyzed by ion chromatograph with samples fractionated by CFA-fraction collector (FC). High time-resolution analysis of ammonium ions on the order of μg/L was sometimes difficult due to contamination from the environment in which CFA-FC was installed. Therefore, we developed an ammonium ion detection system that can be connected to CFA system and investigated the possibility of continuous quantitative analysis.

2. CFA system

The CFA system consists of melting section and analysis section. The melting section consists of a melting head that simultaneously melts and decontaminates the ice core sample and a distance meter that precisely measures the melting length. In the analysis section, gas and liquid are separated in a gas-liquid separator, and then the samples are flowed to each analyzer. The composition of the analyzers varies depending on the ice core to be analyzed and its purpose, but the liquid analysis section mainly consists of a water stable isotope analyzer, a particle analyzer, an ICP mass spectrometer, and fraction collector.

Ammonium ions were analyzed by a fluorescence detector (FLD) using derivatization method with o-phthalaldehyde (OPA). 50 μl/min was used as the flow rate of meltwater from CFA. The lower detection limit was 0.5 μg/L.

Development of a numerical library for higher-order coupling between ice-sheet and climate models

SAITO Fuyuki[1], Ryouta O'ISHI[2], Takashi OBASE[2] and Ayako ABE-OUCHI[2]
[1]*Japan Agency for Marine-Earth Science and Technology(JAMSTEC)*
[2] *Atmosphere and Ocean Research Institute, Univ. of Tokyo*

Ice sheet evolution is often described as responses to variation of other climate systems such as atmosphere and ocean, however, it is well known that there is interaction between the systems and the changes in ice-sheet do feedback on the other systems. Therefore development of coupling models, which simulate the climate components simultaneously, is an important subject in order to compute the evolution of ice-sheet with high accuracy.

The model domain of global climate models is typically defined on longitude-latitude grid system on a (true) sphere, while that of ice-sheet component is typically defined on regional cartesian grid on polar stereographic projection of a ellipsoid.

Exchanges of information between climate and ice-sheet models such as the surface mass balance require a function to absorb the difference of the model structures and, in particular, not to break the conservation. In addition, as already discussed by Fischer et al. (2014), the different structure of the models may cause the projection errors and geometric errors.

In this study, the module adopted in the climate model MIROC to exchange the information between the atmosphere and ocean components (Suzuki et al. 2009) is extended, such that the regional model component of polar stereographic projection can be available. A design to compute polygon areas of overlapped cells follows SPRING (Takeshima et al., 2020) with extending on the polar-stereographic projection. The second-order conservative remapping is implemented using an algorithm presented in Saito (2024).

In the present study, the peformance of the library will be presented in terms of numerical efficiency and also influence of the projection errors and geometric errors on ice-sheet simulation. Demostration of climate field remapping on the ice-sheet domain will be presented.

References

Suzuki et al., Coupling procedures of heat and freshwater fluxes in the MIROC (Model for Interdisciplinary Research on Climate) version 4, JAMSTEC Report of Research and Development,9(1),1-9, 2009.

Takeshima, A., Kim, H., Shiogama, H., et al., 2020: Global aridity changes due to differences in surface energy and water balance between 1.5 °c and 2 °c warming. Environmental Research Letters, 15(9):0940a7, doi: 10.1088/1748-9326/ab9db3.

Saito, F., 2024: Centroids in second-order conservative remapping schemes on spherical coordinates. EGUsphere, 2024:1–31, doi: 10.5194/egusphere-2024-1101.

OMp27

Large abrupt increases in Antarctic snowfall during Heinrich Stadials of the last ice age

Ikumi Oyabu[1,2], Kenji Kawamura[1,2,3], Shuji Fujita[1,2], Christo Buizert[4], Sam Sherriff-Tadano[5], Kumiko Goto-Azuma[1], Motohiro Hirabayashi[1], Hideaki Motoyama[1], Ayako Abe-Ouchi[6]

[1] *National Institute of Polar Research, Research Organization of Information and System, Japan*

[2] *Polar Science Program, Graduate Institute for Advanced Studies, SOKENDAI, Japan*

[3] *Japan Agency for Marine Science and Technology, Japan*

[4] *College of Earth Ocean and Atmospheric Sciences, Oregon State University, USA*

[5] *University of the Ryukyus, Okinawa 903-0213, Japan*

[6] *Atmosphere and Ocean Research Institute, The University of Tokyo, Japan*

During the last glacial period, the North Atlantic region experienced cold intervals characterized by significant iceberg discharge events. These intervals, known as Heinrich stadials, coincided with abrupt climate shifts observed globally. In Antarctica, the accelerated warming was identified from ice-core isotopic records, but changes in precipitation have remained unknown. Here, we present accumulation-rate reconstructions for the last glacial period at centennial resolutions for four ice-core sites in East Antarctica. Surprisingly, large and rapid accumulation increases on a millennial timescale occurred during the Heinrich stadials beyond what is expected from the site warming amplitudes. The sensitivity of accumulation rate to surface temperature for these events could be up to 27% K^{-1}, which is more than double the Antarctic modern sensitivity. The increased snowfall may be attributed to enhanced atmospheric moisture content or meridional transport, which in turn may be driven by a cascade of southward shift of the Intertropical Convergence Zone (ITCZ), southward shift and strengthening of Southern Hemisphere westerly winds, and enhanced wind-driven upwelling of Southern Ocean deep water. Increased frequency or intensity of direct moisture transport may also play a crucial role. Our results provide a consistent picture of southern high-latitude hydrological changes linked to global climate perturbation, with potential implications for current anthropogenic warming.

Unveiling the influence of impurities on recrystallization and crystal orientation in the deepest layers of Antarctic ice cores

*Shuji Fujita[1,2], Tomotaka Saruya[1], Motohiro Hirabayashi[1], Kumiko Goto-Azuma[1,2], Jun Ogata[1], kaori Fukuda[1], kyotaro Kitamura[1], Hiroshi Ohno[4], Iizuka Yoshinori[3]

[1] *1. National Institute of Polar Research, Research Organization of Information and Systems(ROIS), [2.] Graduate Institute for Advanced Studies, SOKENDAI, Department of Advanced Studies,, [3.] ILTS, Hokkaido University Japan, [4.] Kitami Insititute of Technology, Japan*

In the dynamics of polar ice sheets, the deepest few hundred meters are the least understood in terms of structure and properties. This is due to the challenges of accessing and collecting ice core samples from the interior and deep parts of the Antarctic continent. However, in the context of polar ice sheet flow, the deformation of ice at these depths is crucial to the overall movement of ice. Moreover, recent research (Saruya et al., 2024) has shown that the presence of impurities closely relates to the frequency of recrystallization and the formation of crystal c-axis orientation clusters.

To investigate the impact of these impurities on c-axis clustering and dynamic recrystallization, we utilized a 3035m-long ice core drilled at Dome Fuji, a summit in East Antarctica. Specifically, we selected eight depths within the deepest 20% of the total depth (approximately 2,400m to 3,000m). These 7-meter sections of the ice core were shaped into prismatic samples with cross-sections of 32mm x 32mm, and the strength of crystal c-axis clusters was continuously examined with a high resolution of about 15mm.

Additionally, using the same prismatic samples, we conducted continuous flow analysis (CFA) to analyze impurity concentrations (particularly Si, Ca, Al, Fe, Na, Mg, and SO_4) with a high resolution of about 10mm. We then examined the relationship between the strength of crystal c-axis clusters and these impurity concentrations.

The main results are as follows: Continuous analysis revealed that recrystallization appears as numerous intermittent spikes when viewed in the depth direction. Furthermore, the occurrence of these "recrystallization spikes" is primarily in ice with concentrations of dusty impurities below a certain threshold, with virtually no occurrence in ice with concentrations above this threshold. Specifically, the threshold relationships with the number concentration of dust and elements such as Si, Ca, Al, and Fe were clearly identified. In contrast, the relationships with Na, Mg, and SO_4 were inconsistent and unclear. Moreover, in the depth zone corresponding to the deepest 10% of the ice sheet, ice with impurity concentrations that would not normally lead to recrystallization at shallower depths showed a weakening of c-axis cluster strength and the occurrence of recrystallization.

This study provides data for unraveling the effects of depth, ice age, impurity concentration, and temperature on the frequency of recrystallization within ice sheet ice.

References: Saruya, T., Miyamoto, A., Fujita, S., Goto-Azuma, K., Hirabayashi, M., Hori, A., Igarashi, M., Iizuka, Y., Kameda, T., Ohno, H., Shigeyama, W., and Tsutaki, S.: Development of deformational regimes and microstructures in the deep sections and overall layered structures of the Dome Fuji ice core, Antarctica, EGUsphere [preprint], https://doi.org/10.5194/egusphere-2023-3146, 2024.

ice sheet, ice core, recrystallization, impurities

OMp29

Automated snow depth measurements at multiple points along the Antarctic inland route and its device development

Fumio Nakazawa[1, 2], Naohiko Hirasawa[1, 2], Shun Tsutaki[1] and Kenji Kawamura[1, 2, 3]
[1]*National Institute of Polar Research, Japan*
[2]*The Graduate University for Advanced Studies, SOKENDAI, Japan*
[3]*Japan Agency for Marine-Earth Science and Technology*

Observations of snow accumulation (surface mass balance) in inland areas conducted by the Japanese Antarctic Research Expedition began in 1991 as part of the Dome Fuji Project I and have continued to the present. Along the route of approximately 1,000 km from S16, which is located in a coastal region and serves as a base for inland travel, to Dome Fuji Station in the inland region, snow stakes have been installed at around 2 km intervals, and observations are conducted at 505 locations. Since these snow stake observations require on-site measurements by personnel, they are conducted only once or twice a year at most. Three sites along the route (H128, MD78, and the Relay Point) are equipped with Automatic Weather Stations (AWS), which collect snow depth data every 10 minutes. However, along the route from S16 to Dome Fuji Station, there are areas where terrain and wind-driven redistribution of surface snow significantly impact snow accumulation. Therefore, to better understand the regional snow distribution, it is necessary to increase the number of unmanned observation points capable of detailed monitoring of snow accumulation variations.However, the AWS used in the inland region, where temperatures reach extreme lows, are equipped with ultrasonic snow depth sensors, which are expensive commercial products, making it challenging to deploy observations at many locations. To address this issue, we developed a low-cost snow depth measurement system that can operate stably even in extreme cold, based on the method proposed by Iijima et al. (2015).

We used a non-contact ultrasonic level sensor (Fieldpro, Inc., Tokyo, Japan), capable of measuring snow depth and water level. The distance to the target from the sensor is temperature-corrected by an internal temperature sensor and output as a voltage signal. The signals are recorded using a voltage recorder (Ondotori TR-55i-V, T&D Corporation, Tokyo, Japan). The resolution is 5 mm, and the measurable distance ranges from 50 cm to 2.5 m. The power supply is DC12V, and the current consumption is about 7 mA. By turning the sensor power on and off during each measurement, battery power consumption can be reduced. Even with year-round measurements taken every hour, the system can operate on eight AA batteries.

The device was installed in an ultra-low temperature freezer (internal dimensions: W110 cm × D53 cm × H55 cm), and the internal temperature was gradually lowered from -30°C to -80°C to confirm data acquisition. The device itself operated at -80°C; however, when the temperature dropped below -40°C, the voltage readings became unstable, resulting in inaccurate measurements. It is possible that the built-in temperature sensor became unstable, leading to incorrect temperature correction. Currently, we are considering a method of directly acquiring the data before temperature correction and applying the correction using separately obtained temperature data.

References

Iijima, Y., M. Nemoto, K. Shimoyama and T. Nakaji, Quantifying snow depth measurement system using inexpensive ultrasonic depth sensor, JSSI & JSSE Joint Conference on Snow and Ice Research – 2015 in Matsumoto, https://doi.org/10.14851/jcsir.2015.0_268

OMp30

Temperature distribution in the crevasse-drainage systems of the Antarctic glaciers: A case study of the Perunika Glacier

Tsvetan Parov
Bulgarian Academy of Sciences, Space Research and Technology Institute

Livingston Island is part of the archipelago of the South Shetland Islands in Antarctica - a 540 km chain of four main island groups, some are volcanic, including eleven major islands (Elephant and Clarence Islands; King George and Nelson Islands; Robert, Greenwich, Livingston, Snow, and Deception Islands; Smith and Low Islands) and several minor ones with many islets and rocks. Located about 100 km north of the Antarctic Peninsula in the Southern Ocean.

The Perunika glacier is part of the permanent ice cover of Livingston Island. With a length of about 8 km and a width of 3 km, is located approximately 2 km north from the Bulgarian Antarctic Base “St. Kliment Ohridski”. In its lower and middle parts, where the ablation zone is most pronounced, the glacier is heavily crevassed, providing access to subglacial drainage systems formed in the sliding zone between the ice and the ground surface.

This study aimed to determine the depth of heat penetration from the surface of the glacier into the crevasses in the ablation zone and establish the zone of constant temperatures in the glacier. It explored the relationship between the air temperature at the glacier surface and the temperature distribution in the crevasses, including the temperature gradient at different levels and the direction of the airflow.

We used autonomous data loggers for measuring and recording temperature and relative humidity.

The measured depth reached 18 m in the central part of the glacier. Due to the shallower depth of the crevasses in the periphery, temperature sensors were placed at a depth of 9 m there. An ultrasonic anemometer was installed in the deepest crevasse in to the center of the glacier to determine the size and direction of air flows. Meteorological parameters such as air temperature, humidity, atmospheric pressure, and solar radiation were measured on-site using autonomous sensors and recording devices mounted on installations on the glacier surface and at depth using alpine techniques. The results clearly show a temperature gradient through 3-meter layers, a relatively clear boundary of the constant temperature zone, and a significant infiltration of cold air through the crevices driven by turbulent wind processes. Additionally, a weak negative correlation was found between solar activity and temperatures in the crevasses.

It appears that as solar activity increases, the temperature decreases.

There are also weak but consistently positive correlations with air movement both upward and downward. In other words, during higher solar activity, air moves more - both upward and downward.

Although glaciers in Antarctica and around the world are relatively well-studied, the question of heat exchange between the external surface atmosphere and the internal glacier air volumes remains unresolved. The findings from the experiment, such as the constant temperature, its value, and the correlation between solar activity and temperatures in the glacier, provide a basis for long-term monitoring of these parameters, which could provide forecasts for glacier melting. The applied basic methodology for the study is directly linked to the development of sensors, equipment, and software that we install in the glaciers. The methods for securing the measuring instruments in conditions of intense solar radiation and winds reaching up to 140 km/h are the same as those used by high-altitude climbers during ascents in the Himalayas but were found inadequate for our needs in Antarctica. In the future, sensors that do not require frequent servicing may be deployed, as well as the use of a greater number of anemometers for more precise determination of air currents. The relationship between changes in solar radiation intensity and temperatures in glaciers is an important aspect of studying climate change. Studies indicate that variations in solar activity can influence Earth's climate, including glaciers. While solar activity is an important factor, consensus in the scientific community is that human activities, particularly emissions of greenhouse gases like CO2, have a significant impact on the climate. Therefore, to clarify the relationship between changes in solar radiation intensity and the reduction of temperatures in glaciers, it is necessary to consider multiple factors and conduct multifactorial analyses, including studies on solar activity, atmospheric conditions, and anthropogenic influences.

References

de Pablo MA, Ramos M, Vieira G, Molina A, Ramos R, Maior CN, Prieto M, Ruiz-Fernandez J (2024) Interannual variability of ground surface thermal regimes in Livingston and Deception islands, Antarctica (2007–2021). Land Degradation and Development 35(1): 378-393. https://doi.org/10.1002/ldr.4922

F.J. Navarro, U.Y. Jonsell, M.I. Corcuera, A. Martín-Español Decelerated mass loss of Hurd and Johnsons Glaciers, Livingston Island, Antarctic Peninsula J. Glaciol., 59 (213) (2013), pp. 115-128. https://doi.org/10.3189/2013JoG12J144

Georgieva G, Dimitrova L, Gourev V (2019) Ice generated events in Perunika Glacier, recorded by LIVV station, European Association of Geoscientists & Engineers, 10th Congress of the Balkan Geophysical Society, Sep 2019, Volume 2019, p. 1-5. https://doi.org/10.3997/2214-4609.201902661

Gachev E, Meshini E, Matev S, Iliev M, Gachev G, Gacheva M (2024) First records of a new Europe's southernmost glacier found in Southern Albania. Journal of the Bulgarian Geographical Society 50: 75-94. https://doi.org/10.3897/jbgs.e120301

Gachev E (2021) Periglacial landforms and the geological controlling factors: examples from the highest mountains of the Balkan Peninsula. Journal of the Bulgarian Geographical Society 44: 39-47. https://doi.org/10.3897/jbgs.e68982

Kopeckova L, Abalakov in history and in ice. https://www.summitpo.org/abalakov-in-history-and-in-ice/841717 [Accessed 16 April 2024]

Letamendia U, Navarro F, Benjumea B (2023) Ground-penetrating radar as a tool for determining the interface between temperate and cold ice, and snow depth: a case study for Hurd-Johnsons glaciers, Livingston Island, Antarctica. Annals of Glaciology :1-9. https://doi.org/10.1017/aog.2023.73

Martín C, Navarro F, Otero J, Cuadrado ML, Corcuera MI (2004) Three-dimensional modelling of the dynamics of Johnsons Glacier, Livingston Island, Antarctica. Annals of Glaciology 39: 1-8. https://doi.org/10.3189/172756404781814537

Parov T (2023) Influence of atmospheric conditions and solar activity on the underground karst system of the Ponor Mountain. Journal of the Bulgarian Geographical Society 49: 101-112. https://doi.org/10.3897/jbgs.e114034

Purdie H, Zawar-Reza P, Katurji M, Schumacher B, Kerr T, Bealing P (2022). Variability in the vertical temperature profile within crevasses at an alpine glacier. Journal of Glaciology 69(274): 410-424. https://doi.org/10.1017/jog.2022.7

Schaap T, Roach MJ, Peters LE, Cook S, Kulessa B, Schoof C (2020) Englacial drainage structures in an East Antarctic outlet glacier. Journal of Glaciology 66(255): 166-174. https://doi.org/10.1017/jog.2019.92

SILSO, World Data Center - Sunspot Number and Long-term Solar Observations, Royal Observatory of Belgium, on-line Sunspot Number catalogue: https://www.sidc.be/SILSO/home [Accessed 17 April 2024]

Silva, A. B., Arigony-Neto, J., Braun, M. H., Espinoza, J. M. A., Costi, J., & Jaña, R. (2019). Spatial and temporal analysis of changes in the glaciers of the Antarctic Peninsula. Global and Planetary Change, 184, 103079. https://doi.org/10.1016/j.gloplacha.2019.103079

Stoev, P. Stoeva P (2021) Terrestrial temperature variations over karst territories as a response to an 11-year solar cycle. SocioBrains 78: 169-177.

Tapping KF, Charrois DP (1994) Limits to the accuracy of the 10.7 cm flux. Solar Physics 150: 305–315. https://doi.org/10.1007/BF00712892

Williamson SN, Copland L, Thomson L, Burgess D (2020) Comparing simple albedo scaling methods for estimating Arctic glacier mass balance. Remote Sensing of Environment 2461: 111858. https://doi.org/10.1016/j.rse.2020.111858

Willis IC, Pope EL, Leysinger Vieli GJ-MC, Arnold NS, Long S (2016) Drainage networks, lakes and water fluxes beneath the Antarctic ice sheet. Annals of Glaciology 57(72): 96-108. https://doi.org/10.1017/aog.2016.15

OMp31

Relationship between depth and physical properties of snow particles observed at H128 in Antarctica

Takumi Okada[1], Konosuke Sugiura[2] and Naoyuki Kurita[3]
[1]*Graduate School of Science and Engineering, University of Toyama*
[2]*Faculty of Sustainable Design, University of Toyama*
[3]*Nagoya University*

The size and shape of snow particles in the snow layer vary depending on the weather and climate of the place where the snow formed. In particular, such records in polar regions are important for assessing the effects of global warming. In addition, the data obtained is valuable because the polar region are an environment that is frequently inaccessible to humans.
This study reports on snow pit observations conducted out by the 64th Japanese Antarctic Research Expedition (JARE64), which analyzed the size and shape of particles in the snow layer, as well as notable layers (Figure 1). The observations were conducted from December 2022 to January 2023. The observation locations were H15 (latitude 69°4.9'S, longitude 40°46.4'E, altitude 1,021 m), about 50 km inland from Showa Station in Antarctica, and H128 (latitude 69°23.5'S, longitude 41°33.7'E, altitude 1,377 m), about 100 km inland. This analysis mainly reports on observations at site H128 down to a depth of approximately 3.0 m. Regarding particle size and shape, a public domain Java image processing program, ImageJ, was used to analyze the area and circularity of snow particles. Figure 2 (a) shows the relationship between depth and cross-sectional area, with the cross-sectional area increasing as the depth. On the other hand, Figure 2 (b) shows no significant change in circularity with depth, with values ranging from approximately 0.6 to 0.7.

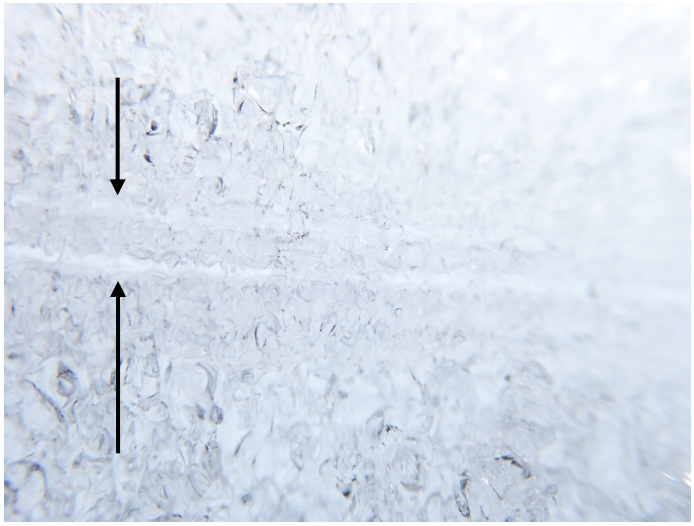

Figure 1. Cross - sectional photograph of the snow layer.
An ice layer-like parts indicated by the arrows can be seen.

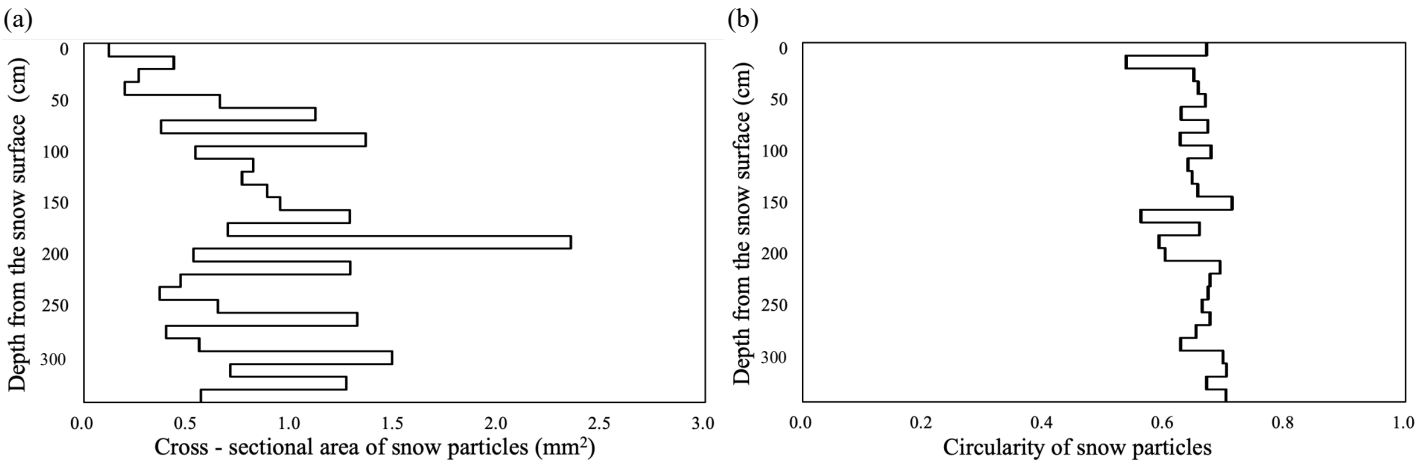

Figure 2. Vertical profile along the depth. (a) Cross – sectional area of snow particles and depth, (b) Circularity of snow particles and depth.

Trend analysis of blowing snow occurrence in Antarctica using the ICESat-2 dataset from November 2018 to October 2023

Konosuke Sugiura[1], and Naohiko Hirasawa[2]
[1]*University of Toyama*
[2]*NIPR*

When winds become strong, snow particles that have once accumulated are blown into the air and blowing snow occurs. This blowing snow is known to have a significant impact on the surface mass balance of the Antarctic ice sheet. Sublimation from the snow particles in blowing snow also results in a loss of surface mass of the Antarctic ice sheet. Furthermore, since blowing snow provides water vapor, the largest contributor of greenhouse gases, to the atmosphere, the occurrence of blowing snow is key to discussing the effects of global climate change as polar warming becomes more pronounced. In order to clarify this effect, it is necessary to understand the actual conditions of blowing snow. In recent years, attempts have been made to detect the occurrence of blowing snow in the polar regions from satellite observations.

The aim of this study is to clarify the occurrence trend of blowing snow in Antarctica using the satellite-based blowing snow products currently available. NASA's ICESat-2 is one of the Earth observation satellites that can detect blowing snow, and has been providing blowing snow occurrence products for the polar regions since October 2018. The Antarctic product was used in this study. The period covered is five years, from November 2018 to October 2023. The trend (slope of the regression analysis) obtained from the regression analysis is shown in Figure 1. The results show an increasing trend for Antarctica as a whole, no clear increase or decrease in the ice sheet top region, a slight decrease along the western coast of East Antarctica and on the Antarctic Peninsula, and an increase in Mizuho Station area, but a significance test is required. As this analysis was conducted over a short period of five years, further analysis using a longer-term dataset is required. Seasonal trend analysis will be carried out in the future in order to gain a better understanding of the occurrence trends.

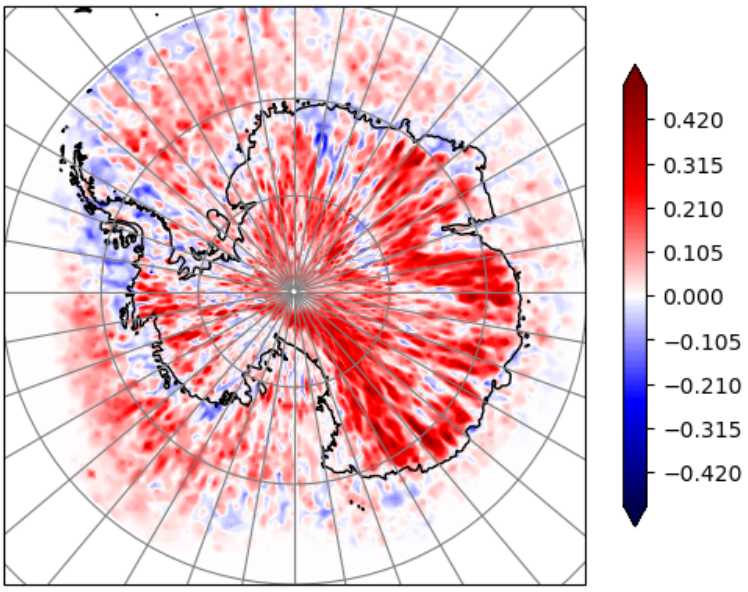

Figure 1. Trends in blowing snow occurrence in Antarctica.